1-1-2019

2d Suspended Fet Technology: Overcoming Scattering Effect For Ultrasensitive Reliable Biosensor

Nirul Masurkar
Wayne State University

Recommended Citation
Masurkar, Nirul, "2d Suspended Fet Technology: Overcoming Scattering Effect For Ultrasensitive Reliable Biosensor" (2019). *Wayne State University Dissertations*. 2329.
https://digitalcommons.wayne.edu/oa_dissertations/2329

2D SUSPENDED FET TECHNOLOGY: OVERCOMING SCATTERING EFFECT FOR ULTRASENSITIVE RELIABLE BIOSENSOR

by

NIRUL MASURKAR

DISSERTATION

Submitted to the Graduate School

of Wayne State University,

Detroit, Michigan

in partial fulfillment of the requirements

for the degree of

DOCTOR OF PHILOSOPHY

2019

MAJOR: Mechanical Engineering

Approved By:

Advisor Date:

DEDICATION

Dedicated to my parents Nihar and Kalpana Masurkar,

my brother Mr. Rukshal and Pranshal Masurkar and My wife Pranali Masurkar and

son Siyan Masurkar, who has always supported me through unconditional love.

ACKNOWLEDGMENTS

It has been an enjoyable experience being a Ph.D. student at Wayne State University, which laid the very foundation of my research career and growth as a person. During which I had the immense opportunity to work with some remarkable people who have guided me along the path for completion of my work. This acknowledgment is to express my personal appreciation to everyone who made my journey possible.

I would like to express my deepest gratitude to my research supervisor Dr. Leela Mohana Reddy Arava, for his assistance, inspiration, and helpful feedback of this research work. He has been the backbone for all my successes and always made sure that I keep moving in the direction for completing my projects on time. I thank my secondary advisor Dr. Gregory William Auner, forgiving his assistance and support in completing my work on schedule. I would like to thank Dr. Golam Newaz, Dr. Guru Dinda, Dr. Mahendra Kavdia for being on my committee and providing with useful critiques for my work. I thank my department chair Nabil Chalhoub and department secretary Lisa Rapicano for their help in getting approvals done quickly. I thank Dr. Zhixian Zhou for lending his equipment during device characterizations as well as Dr. Mark Cheng and Dr. Pai yen Chen for supporting me at the initial period of my Ph.D.

I had the privilege to work with some of the best scientists and researchers from all over the world. I appreciate the help of Dr. Antony George and Dr. Hemtej Gullapalli for their insights and suggestions for this work. I thank Professor Pulickel Ajayan from Rice University for his valuable advice toward my research.

I am greatly indebted to my former advisors Dr. Ingemar Lundstorm, Dr. P.F Turner and Dr. Edwin Jager from Linkoping University, Sweden as well as Dr. Brian Lawrenson, Dr. T.J Dines and Dr. Kazeem Dastoori from University of Edinburgh and University of Dundee, Scotland *for coaching and guiding me the fundamentals of Microelectromechanical systems (MEMS) technology and solid-state electronics. This knowledge laid the very foundation of my research work and has helped me publish my first research article.*

I am thankful to my colleagues at the Functional Nanomaterials and energy devices laboratory for providing their support in my research work: Dr. Hesham Al Salem, Dr. Bhuvaneshwari Dharmarajan, Dr. Khalid Ababtain, Deepesh Gopalakrishnan, Abdualrazzag Sawas, Uday Praveen, Kiran Mahankali, Sathish Rajendran and Sanjeev Porchelvan.

I am grateful to work with Dr. Babu Ganguli and Dr. Naresh Thangavel, who helped me a lot and cleared my scientific doubts throughout a Ph.D. journey. I want to thank Mr. Sundeep Varma for supporting me throughout my Ph.D program without him, this journey would be tedious.

I would like to thank my research friend's Dr. Ali Shahini, Dr. Eric Gui Rui Kim, Dr. Aby K George, and Mohammed Ashraf Ali for supporting and guiding when I needed the most. I am grateful to Sally Yurgelevic, Chris and other team members of Smart Sensors and Integrated Microsystems for helping me with sample characterization. I thank Dr. Zhi ("Mike") Mei, Wayne State University, and Dr. Allen Hunter and Dr. Haiing Sun, University of Michigan for helping me with SEM and TEM samples.

I had immense pleasure in guiding and nurturing research study of undergraduate and graduate students Gregory Hunter, Ann Amarachi Mark, Bassam Samir Bitar, and Kawsar Jamil. I learned a lot while teaching them different properties of fabrication and characterizations of electronic devices. Apart from my research work I had a wonderful opportunity in training high school's students Petro, Mary, Aida, Mikita, and Darina. This was one of the few unique moments where I have enjoyed sharing my research with future engineers.

I am grateful to my professors from St. Vincent Palloti College of Engineering and Technology, India for educating me the fundamental aspects of science during my undergraduate program. I would like to thank Prof. K. S Narayan and Prof. C.N.R Rao from JNCASR (IISc), Bangalore, India, for edifying my knowledge towards molecular electronics devices. I'd like to thank my backbenchers' friend from engineering Sagar, Sumant, Gajanan, Avishkar, and Aamir whom I enjoyed my logical journey.

My journey wouldn't have been possible without the endless encouragement and support of my parents Mr. Nihar and Mrs. Kalpana Masurkar, my brothers Rukshal and Pranshal Masurkar and My wife Pranali Masurkar and son Siyan.

TABLE OF CONTENT

DEDICATION ……………………………………………………………………..............ii

ACKNOWLEDGMENT……………………………………………..…………....iii

LIST OF TABLES ……………………………………………………..……….....xi

LIST OF FIGURES ……………………………………………..…….…......xii

CHAPTER 1 INTRODUCTION…………………………..……………….……..1

CHAPTER 2 BACKGROUND AND LITERATURE REVIEW……………..…..…......5

2.0 FET-based biosensor……………………………………………………….…..…6

2.1 Nanomaterials…………………………………………………….………..……….7

2.2 2D Materials………………………………………………………………….…..8

2.2.1 Graphene………………………………………......................................…….9

2.2.2 TMDs …………………………………………………………..……….…....12

2.3 Challenges in 2D material: Transport and Scattering mechanism in 2D materials……..…………………………………………………...……………...14

2.4 Solutions for Scattering ………………………………..………………..……16

2.5 Fabrication of Suspended 2D FET process flow ……………..………………….………....17

2.5.1 Suspended MoS_2 FET device…………………………………………..……...18

2.6 Hypothesis……………………………………………………………...…………..19

2.7 Dissertation Objectives……………………………………………...…………..22

2.7.1 Synthesis of 2D materials via CVD and FET characterization……………………..…….22

2.7.2 Fabrication of nanogaps and characterization of suspended FET……………………..….23

2.7.3 Testing pH and E-coli bacteria concentration via suspended FET biosensor……………………………………………………….……………………....24

CHAPTER 3 SYNTHESIS OF 2D MATERIALS VIA CVD METHOD AND FET CHARACTERIZATION………………………………………..….............................25

3.1 Synthesis of 2D materials……………………………………………………………….25

3.2 Chemical Vapor Deposition…………………………………………...………...25

3.2.1 Temperature and precursors optimization……………………………….............26

3.2.2 Pressure Optimization………………………………………….……………...30

3.2.3 Growth Surface Optimization………………………………….………………...32

3.3 Characterization of monolayer TMDs…………………………..…………….........34

3.3.1 Scanning Electron Microscopy and energy dispersive X-ray spectroscopy….…………………………………………...……………….………..34

3.3.2 Transmission Electron microscopy………………………………….……..….36

3.3.3 RAMAN Spectroscopy…………………………………………….…………38

3.3.4 X-ray diffraction (XRD) ……………………….…………………………….….40

3.3.5 Atomic Force Microscopy (AFM) ………………..…………………………..41

3.4 Electrical characterization of CVD grown TMDs…………………………………….41

3.4.1 Fabrication of 2D FET……………………………………………………..….41

3.4.2 FET characterization of MoS_2 and WSe_2………….……………………………...44

3.5 Summary and conclusion……...……………………………………………..….47

CHAPTER 4 SUSPENDED 2D MATERIALS FET……………….………………….…50

4.1 Introduction……….……………………………………………………………50

4.2 Challenges involve in 2D FETs………………………………….………....51

4.3 Suspended 2D FET via nanogaps……………………………..…….…….…52

4.4 Fabrication of the nanogaps……………………………………………….….53

4.5 Evaluation of nanogaps………………………………………….……..…...57

4.6 Novel dry stamping method……………………………………..…………..58

4.7 Characterization of 2D TMDs on the top of nanogaps……………….………….60

4.7.1 AFM mapping on the suspended 2D materials……………….………..…60

4.7.2 SEM and Dark field imaging of the suspended 2D material………………...………61

4.7.3 Raman Mapping………………………………..……………...……….……..62

4.8 Depositing the dielectric layer……………………………………………..64

4.9 TEM of cross-section…………………………………………………….…...64

4.10 Electrical characterization of suspended TMDs…………………….…………….67

4.11 Summary and conclusion…….......………………………………………..70

CHAPTER 5 SENSING FROM SUSPENDED 2D FET DEVICE…………….…....72

5.1 Introduction……………………………………………………………………..72

5.2 Ionic gating of suspended FET…………………………...………………74

5.3 pH sensing………………………………………………..……….…..…….76

5.4 Bacteria sensing from suspended FET……………………………….…….……….…………..….79

5.5 Summary and conclusion…....………………………………………….……….…….……...…85

CHAPTER 6 CONTRIBUTION AND FUTURE OUTLOOK………..….….……….…....87

6.1 Summary of contribution………………………………………..…….…..….…….....87

6.2 Future Outlook………………………………………………..……….……………..…..90

APPENDIX……………………………………………………………….………....…..92

Appendix A…………………………………………………..………….……..…..….…92

REFERENCE………………………………….………………………….……...........101

ABSTRACT……………………………..……………………………….……...……...118

AUTOBIOGRAPHICAL STATEMENT…..………………………………….……..120

LIST OF TABLES

Table 3.1 Different 2D TMDs material grown in the CVD……………………………….49

Table 5.1 Comparison of 2D FET based biosensor………………………………………..85

Table 6.1 Comparison of Suspended FET with other materials…………………………...89

LIST OF FIGURES

Figure 1.1 a) Schematic of FET based Biosensor with source and drain, biorecepter, and target molecules (b) Conduction band profile of tradition FET……………………………..2

Figure 2.1 Flow chart of elements of the biosensor (sampling, biological receptors, transducers, and detection) ………………………………………………………………………5

Figure 2.2 Electrostatic effect of biomolecule (a) bulk materials (b) nanomaterials……………..7

Figure 2.3 (a) Molecular bond of the Graphene (b) Band gap of Graphene……………………10

Figure 2.4 (a) Graphene based FET sensor for detecting the E-coli bacteria (b) I_D-V_{LG} curve of the FET before and after incubation of the E-coli bacteria; 100 CFU/mL. (c) I_D-V_{LG} of the bare graphene, linkers, anti E-coli, Ethanolamine, and tween20. (d) I_D-V_D characteristics at different concentration of the E-coli. ……………..……………….11

Figure 2.5 (a) Molecular diagram of MoS_2 (b) Band gap of MoS_2……………………………...12

Figure2.6: (a) Schematic of MoS_2 biosensor with HfO_2 dielectric coating, bioreceptor, and target biomolecules with Ag/AgCl biasing from the electrolyte (b) I_D-V_{LG} profile of different pH (3,4, and 5) (c) I_D-V_{LG} profile of buffer and 100fM streptavidin. …….14

Figure2.7 Scattering effect from substrate……………………………………………………...15

Figure 2.8 (I) MoS_2 device fabrication process (a) creating contacts via e-beam lithography on the top of supported MoS_2 crystal (b) Etch SiO_2 in Buffer Oxide Etch and (c) followed by entanol washing and then critical point dryer is used to remove all wet contaminants (d) Final schematic

(II) Final device image of suspended MoS_2 underneath the electrodes (a) optical microscope (b) SEM (c) AFM (d) AFM line profile. ………………………………...17

Figure 2.9 Ionic gating of suspended MoS_2 device (a) Schematic and (b) optical image (c) SEM image of suspended device (d) I-V characteristics of different bias voltage (e) I-V transfer curve of suspended MoS_2 at two different temperature. …………………...18

Figure 2.10 Free standing layer of 2D TMDs (MoS_2) is sagging on wide spacing electrode and (b) functionalization of antibodies, which might interact with supporting substrate……21

Figure 2.11 Free standing layer of 2D TMDs (MoS_2) is robust on nano spacing electrode and (b) allows the functionalization of antibodies without interacting with supporting substrate……………………………………………………………………………...23

Figure 3.1. (a) In-house CVD for TMDs growth (b) Schematic representation of the experimental setup for CVD growth. (c) Process flow of typical MoS_2 growth. ………………….27

Figure 3.2 (a) SEM image of MoS_2 CVD growth at low temperature (b) EDAX of MoS_2 at low temperature..........28

Figure 3.3 (a) XRD of MoS_2 growth at lower temperature (b) Optical image of the biproducts at lower temperature (c) Raman mapping of bulk MoS_2..........29

Figure 3.4 (a) SEM image of large MoS_2 (b)Optical image of MoS_2 high magnification (c) Optical image of MoS_2 at low magnification..........30

Figure 3.5 Morphology of flakes associated with Pressure, which is related to the sulfur concentration while growing MoS_2 in the CVD (a) low magnification image of square flakes at 0.5-1 KPa (a') high magnification image of square flake at 0.5-1 KPa (b) low magnification image of hexagonal flakes at 1 KPa (b') high magnification image of square flake at 1 KPa (c') low magnification image of triangular flakes at 5 to 8 KPa (c') high magnification image of triangular flake at 5 to 8 KPa (d) low magnification image of star flakes at <20 KPa (d') high magnification image of star flake at <20 KPa..........31

Figure 3.6 Growth and Morphological characterization on different substrate: (a-a') low and high magnification of triangle on SiO_2 substrate (b-d) low and (b'-d') high magnification SEM images of $MoSe_2$ morphology grown at (b, b') 760 °C (c, c') 850 °C (d, d') 950 °C. Scale bars: 10 µm and 1 µm..........33

Figure 3.7 (a) SEM image of large MoS_2 on SiO_2 surface (b) and (c) EDAX mapping of MoS_2 triangle with Sulphur and Molybdenum atom distributed evenly. (d) SEM image of $MoSe_2$ nanoflower high magnification (e) and (f) EDAX mapping of $MoSe_2$ nanoflower with Selenium and Molybdenum atom distributed evenly..........35

Figure 3.8: (a) Low magnification TEM mage of MoS_2 (b)Optical image of MoS_2 high magnification (c) Optical image of MoS_2 at low magnification (d) (e)&(f) EDAX mapping of MoS2 triangle with Sulphur and Molybdenum atom distributed evenly..........36

Figure 3.9: (a) SEM image of pyramid MoS_2 (b) and (c) EDAX mapping of pyramid structure of MoS_2 (d) STEM image of the 1L and 2L (e) EDAX spectra of pyramid MoS_2.......37

Figure 3.10 Raman characterization of triangular (a) MoS_2 (b) $MoSe_2$ (c) WS_2 (d) WSe_2.........38

Figure 3.11 X-ray diffraction pattern of of CVD grown triangular flakes where samples displays its characteristic (002) plane peak and their relative intensities at temperature 760°C, which is the signature of the well stacked crystalline structure of (a) MoS_2 and (b) $MoSe_2$..........40

Figure 3.12 (a) AFM mapping of the triangular MoS_2(b) Line profile of the triangular of MoS_2 layer……………………………………………………………………………41

Figure 3.13 Process flow to achieve 2 µm IDE by using optical lithography……………………42

Figure 3.14 (a) Process flow for wet transferring of MoS_2 triangle (I) MoS2 triangles on the substrate (II) Coating of the PMMA as a sacrificial layer (III) Etching of the SiO_2 in the KOH solution (IV) RCA cleaning of the fragile MoS_2 flake to remove inorganic and organic contamination (b) Low magnification, SEM image of the IDE electrodes (scale bar 100 µm) (c) High magnification of IDE electrode with MoS_2 traingular flake (scale bar 10 µm) ……………………………………………………………………...43

Figure 3.15 (a) Schematic of the back gate 2D MoS_2 (b) SEM image of the MoS_2 triangle transfer on electrodes, which are separated by 4 µm. (c) I_D-V_{BG} linear transfer curve where gate potential is applied from the back side of the highly doped wafer (d) Logarithmic I_D-V_{BG} transfer curve of MoS_2 where SS is 1.5 V/dec (d) I_D-V_{DS} characteristics to check the ohmic contact…………………………………...………………………...44

Figure 3.16 (a) Band aligment of source/drain metal for p-type and n-type with the triangular WSe_2 (b) I_D-V_{BG} linear transfer curve of channel WSe_2 where gate potential is applied from the back side of the highly doped wafer at voltage 100 mV and 500 mV (c) Logarithmic scale of WSe_2……………………………………...………………………46

Figure 4.1 (a) Schematic of the 2D top gate FET with the scattering phenomenon from the supporting substrate (b) schematic of tunneling of the electron from source to drain with scattering effect. …………………………………..……………………..51

Figure 4.2 (I) Si/SiO_2 wafer (II) flood exposure of 1811 (III) Photoresist 1811 coating in spinner at 3000 rpm (IV) Exposing and developing 1811 (V) Depositing metal Cr/Au/Ti (VI) Lift-off 1811 (VII) Coating 1811 for second electrode (VIII) Developing 1811 photoresist (IX) Second electrode metallization Au/Ti (X) Stripping of 1811 and LOR (XI) Two Au/Ti electrodes separated by nanogap………………..………………...54

Figure 4.3 (a) LOR A fabrication of Nanogap (b) Thin layer of Chromium reluctant to lift off Au (c) second layer gold and chromium (d) lift of the chromium with constant nanogaps…………………………………………………………………………..55

Figure 4.4 (a) Wafer scale production of the nanogap with different structures (b) Nanogap array device at low magnification (c) high magnification of the nanogap array with proper lift of the chromium (d) Wafer scale flexible substrate (e) low magnification of nanogap array on the flexible device (f) high magnification of the nanogap electrodes on the flexible substrate……………………………………………………………………...56

Figure 4.5 Electrical characterization of nanogaps (a) I-V characterization of open circuit (no connection of electrode). Scanning voltage: -0.5 V to 0.5 V. (b) I-V characterization of short circuit (connection of the nanogap). Scanning voltage: -0.4 V to 0.4 V………..57

Figure 4.6 Dry transfer of CVD grown MoS_2 (a) Process flow of dry stamping of MoS_2 on nanogap electrodes (b) Image of the transferring PMMA on the glass slide (c) Image of aligning MoS_2 triangle with nanogaps in the microscope & (d) Lift off the micromanipulator on z-axis at 100°C..........58

Figure 4.7 Optical image, AFM mapping, and line diagram of nanogaps (a) without MoS_2 (b) with MoS_2..........60

Figure 4.8 (a) high magnification SEM image of MoS_2 on the top of nanogaps (scale bar: 100 nm) (b) Optical dark field image of MoS_2 triangle on the top nanogaps. 62

Figure 4.9 (a) Optical image of nanogap and highlighted Raman mapping area points P1 - supported and P2 - suspended, (b) Schematic of device arrangement for Raman mapping, (c) Raman spectra for supported and non-supported MoS_2 and (d) Photoluminescence intensity of MoS_2 on supported and non-supported substrates...63

Figure 4.10 (a) A device with multiple nano gap electrodes, (b) Deposition of multiple Pt layers to form a 10µm × 2µm island, (c) Add markers to milling back and front side of the Pt deposition, (d) Sequences of milling makes trances, (e) L-Shaped milling done and lamella is free standing, (f) Micromanipulator carefully picks the lamella and welded to the TEM grid, (g) Slow thinning of the sample to get rid imperfections during milling, (h) cross section images after fine thinning and (i) high magnification cross-section images shows a nanogap of 10 nm..........65

Figure 4.11 (a) TEM image of the cross section of suspended 2D material (b) EDAX overlay image of Mo, Au, and Hf, elemental mapping in the TEM instrument of (c) Mo (d) Au (e) Hf..........67

Figure 4.12 Top gate I_D-V_{BG} transfer curve of the suspended at 100 mV of (a) WSe_2 (b) MoS_2; (c) top gate I_D-V_{DS} charaacteristics of WSe_2 and MoS_2..........68

Figure 4.13 (a) PMOS WSe_2 and NMOS MoS_2 suspended inverter where negative input potential gives positive output and positive input provides negative output..........69

Figure 5.1 (a) Image of biosensor device with Source, Drain, and Gate (Ag electrode) connection (b) Schematic of Biosensor with E-coli and antibodies..........73

Figure 5.2 (a) back gating of suspended MoS_2 with 90 nm channel length (b) Ionic gating of suspended MoS_2. Current-drain voltage characterization (a') Suspended MoS_2 with back gating from -10 V to 30 V. (b') Suspended MoS2 with ionic liquid gating from -1 V to 1V..........75

Figure5.3 Schematic of protonation and deprotonation on HfO_2 substrate..........77

Figure 5.4 pH detection of suspended MoS_2 FET (a) I_D-V_{LG} curve of different pH concentration on the suspended MoS_2 (subset: Linear graph of I_D-V_{LG}). (b) Sensitivity of pH in subthreshold, saturation, and linear regions from pH 5 to pH 7. (c) experimental threshold voltage of suspended MoS_2 FET from pH 3 to pH 9 (Left-axis); experimental current corresponds to threshold voltage (Right-axis) ……………………………..78

Figure 5.5 I_D-V_{LG} curve at constant bias 100 mV (a) APTES linkers with antibodies (Blue), 100 CFU/mL E-coli bacteria (Magenta) (b) Dithiol linkers with antibodies (Black), 100 CFU/mL E-coli bacteria (Red) ………………………………………………...79

Figure 5.6 Inducing of electron by APTES molecule (a) schematic of the APTES molecule and the equivalent dipole (b) I_D-V_{LG} curve at V_{DS} 100 mV of buffer solution (Cyan) and functionalization of APTES (Red) ……………………………………………..80

Figure 5.7 Schematic diagram of self-assembly process for immobilization of E-coli bacteria on HfO_2 surface……………………………………………………………………..81

Figure 5.8 (a) I_D-V_{LG} curve of SAM process at 100 mV bias; Functionalization of APTES (Red), immobilization of E-coli antibodies (Blue), buffer solution 0.01 M PBS solution of pH 7 (Cyan), and detection of E-coli bacteria of 100 CFU/mL (Magenta). (b) I_D-V_{LG} characterization of E-coli bacteria from 0 CFU/mL to 10^3 CFU/mL………………..82

Figure 5.9 (a) Comparison of I_D-V_{LG} characterization of E-coli and P. aeruginosa bacteria (100 CFU/mL) with PBS buffer solution………………………………………………..83

Figure 5.10 (a) Sensitivity measurement of E-coli bacteria at subthreshold, linear, and saturated regions. (b) Sensitivity comparison of three suspended MoS_2 FET devices by immobilizing the 100 CFU/mL E-coli bacteria……………………………………...84

CHAPTER 1 INTRODUCTION

Biosensors are prominent devices in the medical field, which are proliferating in other domains such as forensic industries, national security, and ecological monitoring (water and air) [1]. Especially, electrochemical field-effect transistor (FET)-based biosensors are attracting much attention due to their compatibility with electronic chips to achieve real-time data, low power consumption, label-free detection of specific biomolecules, and low-cost mass production [2]. Traditional FETs consist of a semiconducting channel connected with two electrodes (source and drain) where gate electrodes manipulate channel conductance by using an electrostatic field called the gating effect [2]. Generally, the gating effect is produced by applying a voltage through a metal gate electrode, which is capacitively attached with the semiconductor via a thin dielectric layer. However, in the case of a FET-based biosensor, a physical metal electrode is replaced by a specific receptor for selective target biomolecules. The trapped charged biomolecules generate a gating effect and change the conductivity of the channel, which is easily measured by transistor characteristics such as the source to drain current [3, 4]. Silicon dioxide (SiO_2) is usually used as a dielectric layer in transistors, but in biosensors, it is replaced by polymers and lipids, i.e., a bioreceptor, which can be easily functionalized on the semiconducting channel by using selective linkers as shown in Figure 1.1 (a).

For a semiconducting channel in FET-based biosensors, many materials have been categorized for better performance. These materials can distinguish according to their structures, such as bulk, *i.e.*, 3 dimension (3D), and nanomaterials, such as 0 dimension (0D), 1 dimension (1D), and 2 dimensions (2D). Among the two types of semiconducting materials, nanomaterials are attracting much attention because of their high surface to volume ratio that provides higher sensitivity. In nanomaterials, 0D and 1D such as fullerene (C_{60}), Si nanowires, and carbon

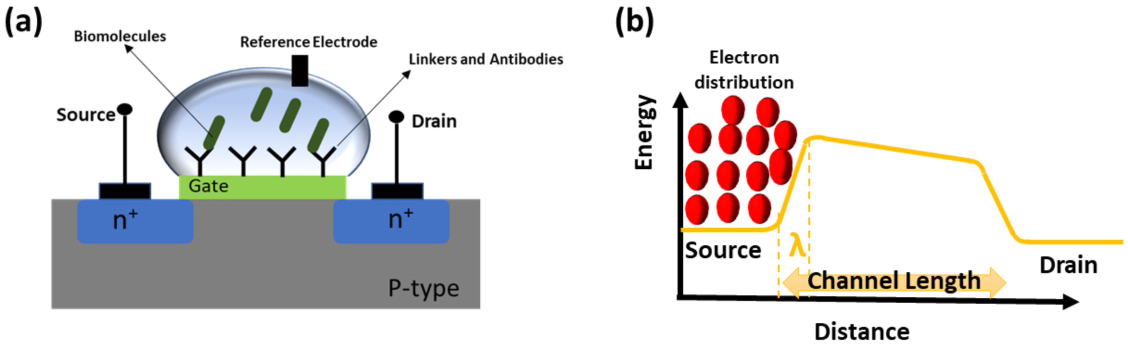

Figure 1.1 : (a) Schematic of FET based Biosensor with source and drain, biorecepter, and target molecules (b) Conduction band profile of tradition FET

nanotubes (CNT) are well studied as semiconducting materials for biosensor applications to drive high current with small changes in gate potential [3-5]. Despite the higher sensitivity of 0D and 1D materials, there are difficulties in the fabrication process, which is the major hindrance in the success of 0D and 1D technologies [6, 7]. The top-down method to fabricate 0D and 1D materials is expensive, and the production rate is slow, whereas the bottom-up approaches have severe integrability issues that hinder the practical usage of these structures [8]. These issues can be eliminated by using 2D materials which have pristine structure and can provide an excellent electrostatic effect due to the thin atomic layer [9]. The main parameter in FET based biosensor, which improves the efficient electrostatic from the gate to the semiconducting channel is the natural length scale (λ) as demonstrated in Figure 1.1 (b) [10]. The natural length depends upon the gate capacitance (C_g) and semiconducting channel permittivity (ε_s) as well as thickness (t_s) as illustrated in expression 1.1.

$$\lambda = \sqrt{{}^{\varepsilon_s}/{}_{C_g}\, t_s} \ldots\ldots\ldots\ldots\ldots\ldots..(1.1)$$

To achieve a better electrostatic effect in the FET transistor, λ should be smaller than the channel length (L_g) [11]. From equation (1.1), λ is directly proportioned to the thickness of the semiconductor. Hence 2D materials are highly promising for the semiconducting channel, where

t_s i.e. thickness is in nanometer size. Therefore, 2D material possesses better electrostatic effect by varying the small magnitude of the gate potential. In addition, 2D materials are easy to pattern due to planar structure, and dangling bond free surface, which is well suited as a semiconducting channel in FET than 1D and 0D materials.

In the 2D domain, graphene has shown great potential since last decade because of their exclusive properties in electrical, optical, mechanical, and chemical [14]. After the great achievement of graphene, recently, some new materials interest has emerged in 2D transition metal dichalcogenides (TMDs) such as MoS_2, $MoSe_2$, WS_2, and WSe_2 [14]. The properties of ultrathin 2D TMDs are intriguing fundamentally as well as technologically, in contrast of graphene, which is semi-metallic in nature, TMDs have a direct bandgap in monolayer and indirect in bulk [16]. Monolayer TMDs bandgap and carriers (n-type or p-type) can be tailored between compounds depending on their chemical composition [14, 15]. Due to the variation in the chemistry of different compounds and the crystal structure tends towards dramatic changes in their electronics properties, TMDs nanosheet has been widely studied and applied in various applications.

Despite these merits, the performance and consistency of such atomic layer crystals are easily affected by supporting substrate interaction. This interaction of supporting substrate and atomic layer TMDs implies that the control of interface is vital for the performance and reliability of electronic devices. In specific, SiO_2 substrate are highly disordered morphology as well as chemically active due to the trapped atmospheric gases, chemical species, unidentified functional group, and electrostatic charges [12]. Therefore, transferring another layer of 2D TMDs on the top of SiO_2 cannot contribute to charge transport clearly, which leads to the unreliable function of every single device. In recent years, many efforts have been made to enhance the quality of the substrate active layer interface such as using Poly(methyl methacrylate) (PMMA) and polymer electrolytes [9] which elude chemical bonding or surface roughness and improve mobility, but it cannot be useful in specific applications such as biosensor. In addition, suspended 2D layer devices have been reported by wet etching silicon dioxide underneath the monolayer. Freestanding 2D TMDs has shown better performance than the supporting on the SiO_2 substrate in terms of back gating electronic conduction [13]. However, the existing SiO_2 requires hazardous chemical etchants such as hydrofluoric acid (HF), which is difficult to handle and affects the 2D film structure and purity [14]. Secondly, freestanding MoS_2 sags between the two electrodes because of the large spacing (~ 2 µm), which makes it impossible to coat another layer such as hafnium oxide (HfO_2) and antibodies on top of monolayer. Therefore, this structure impedes making top gate FET biosensors and integrated circuits, which allows for only back gating. However, the back gate FET requires more power (input gate voltage) to turn ON the device than the top gate, which hinders making a low power and highly sensitive FET-based biosensor because of the sensitivity of a sensor in the subthreshold region inversely proportion to the change in input gate voltage discussed in chapter 5 [15, 16]. Secondly, when linkers/antibodies are directly attached to the sagging bare channel, the transduction mechanism is the combination of the electrostatic gating, direct charge transfer, and mobility modulation. This type of structure cannot provide reliable output. Therefore, it is desirable to eliminate the density of defects by covering the bare channel material with insulating material and then functionalizing linkers and antibodies on the top of the insulator for reliable output and specific detection [15, 17].

CHAPTER 2 BACKGROUND AND LITERATURE REVIEW

The first biosensor was presented in 1962 by Clark and Lyons based on the enzyme electrode biochemical to detect the chemical components in the blood [1]. Since then, a steep progression in bio-sensing technology is evolved and create a significant impact on global human healthcare, environmental monitoring, drug delivery, and food safety [18]. The biosensor consists of the transducer that produces a measurable signal by varying physical or chemical properties of the active material. Till now, there are various types of transducing mechanism investigated and commercialized from which optical, piezoelectric, and electrochemical are well known. In optical sensing, change in the light absorption, reflection, and emission are occurred due to the variation in biomolecules [19]. Whereas, piezoelectric transducer works on the change in mass induced by the change in the concentration of bio-recognition event [20]. Lastly, electrochemical transducers comprise a change in the electrical impedance, potential, current, and modulation of the conductance by means of the sensing materials [21]. From these three types, electrochemical

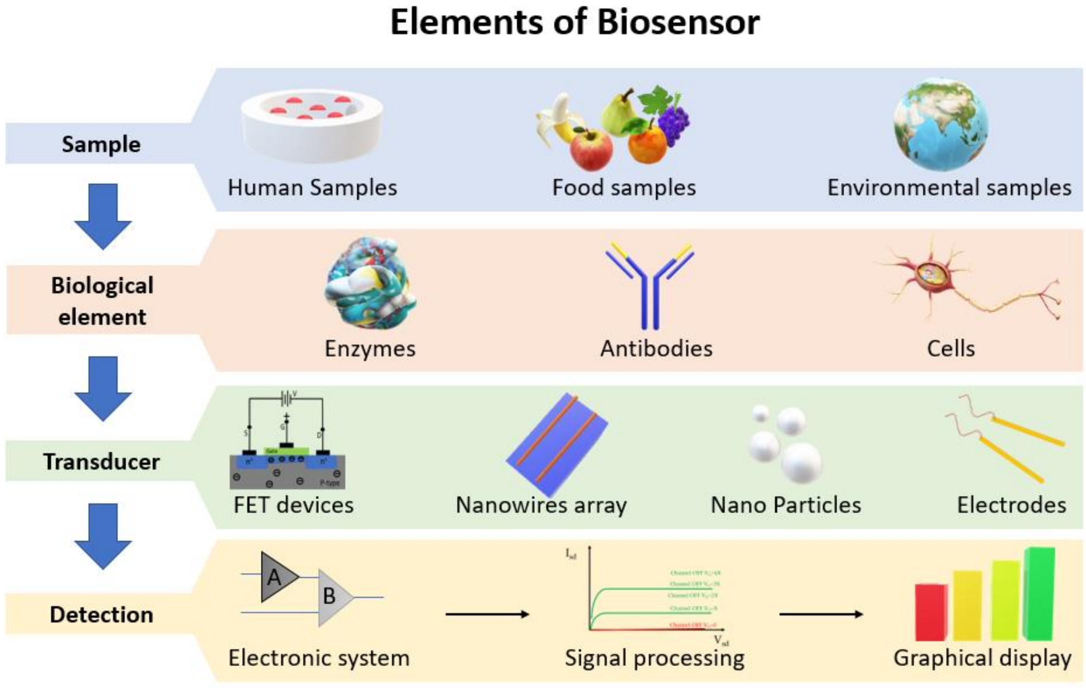

Figure 2.1 Flow chart of elements of the biosensor (sampling, biological receptors, transducers, and detection)

transducers are gained more attention due to the easy fabrication, fast in response, portable, and low power requirement [22]. Electrochemical transducers can be further distinguished according to their electrical interface with the samples and electronics system, as shown in Figure 2.1. From these electrical interfaces, FET based device are well known due to the excellent sensitivity and selectivity, cost-effective wafer-scale fabrication, label-free detection, and easy to integrate with modern electronic devices such as a smartphone.

2.0 FET-based biosensor

Field Effect Transistor (FET) based biosensor is the excellent combination of biological analytes and electronics, where biomolecules related elements induce potential on the gate and change the output current in between two electrodes called source and drain. The gate electrode is capacitively coupled with the semiconductor channel by a dielectric layer, which brings the modulation in the channel through electrostatic effect. In the FET based biosensor, the gate voltage is given from the electrolyte buffer solution, i.e., the conductance variation in the channel modulated by the ions present in the electrolyte. Therefore, such type of biosensor is known as an ion-sensitive field-effect transistor (ISFET). In ISFET, semiconducting materials play a significant role because the sensitivity and response time of the sensor depends upon the transconductance in the channel. Hence, many semiconductors are evaluated and investigated for better electrostatic effect from the gate in the biosensor domain [23]. The first-generation semiconductors used in ISFET as a channel material are a silicon (Si), gallium arsenide (GaAs), silicon carbide (SiC), gallium nitride (GaN), and indium gallium arsenide (InGaAs). These materials are well known in electronics industries for consistency in output response and having a matured fabrication technology. However, due to the bulk atomic structure, the electrostatic effect from the gate is not severe, which leads to the reduction of the sensitivity, recovery time, and the speed of response. In recent years, nanomaterials are generated an enormous amount of interests in the semiconducting channel due to the high surface-to-volume ratio and decrease the mean free path of an electron, which increases the performance of the sensors [24].

2.1 Nanomaterials

As a materials dimension reduced in the nanometer regime (1-100 nm), the surface to volume ratio, i.e., the ratio of surface atoms to the interior atoms is high. This type of structure is beneficial in the semiconducting channel of ISFET because of the external influence (electrostatic effect from the gate) penetrates interior as well as surface atoms, as shown in Figure 2.2 (a) and (b). Therefore, a small change in the charged particles or biomolecules on the gate electrode brings a significant variation in conduction of nanomaterials, which can increase the sensitivity and reduce the detection limit. The atomic arrangement in the nanometer domain is confined, which reduce the internal scattering phenomenon of electron and decrease the mean free path [25, 26]. This advantageous atomic arrangement helps to enhance mobility as well as reduce the response time of detection. In addition, some nanomaterials are easily functionalized with the bioreceptor without any modification for specific detection of the biomolecule due to the tailoring of the wettability [27, 28]. Therefore, nanomaterials-based ISFET provides the best sensing platform by

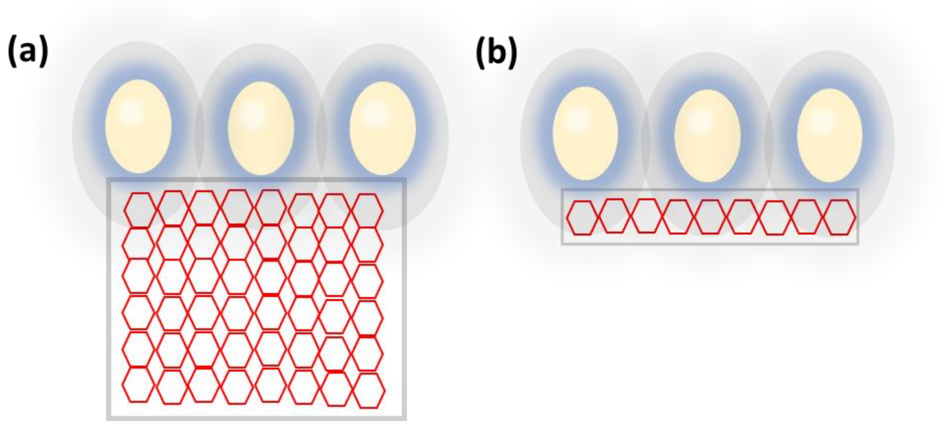

Figure 2.2 Electrostatic effect of biomolecule (a) bulk materials (b) nanomaterials

offering an excellent interface with bioreceptor, facilitate the binding of biomolecules, and reduce overall system power due to nano-level of operation.

The performance of the nanomaterials in semiconducting channel depends upon the structure and the morphology, which are distinguished in 0D, 1D, and 2D. Each dimension exhibits unique properties that contribute tremendous potential in biosensing and bioelectronics applications. 0D and 1D are known as the first generation of the nanomaterials such as fullerene (C_{60}), Carbon nanotubes (CNT), Silicon nanowires, gold nanoparticles, etc. These materials have shown better performance in FET based biosensor by driving high current with small gate potential from charged particles and biomolecules [29]. Detection of the single-molecule and improvement of the sensitivity with these structures have been reported. Despite the various merits of 0D and 1D, this technology is not successful in flourishing at biosensor domain due to the low electronic mobility, bandgap tuning is vigorous and impossible to fabricate in large scale. These flaws of the 1D and 0D nanomaterials are eliminated in 2D structure due to the pristine nature, compatible with recent nano/microfabrication, and easy to tune the bandgap.

2.2 2D Materials

In 2004, a single layer of graphite had been isolated by Andre Geim’s group at the University of Manchester, known as graphene [30]. Prompted by these an ample number of reviews and articles have been publishing on 2D materials and its applications. The emergence of 2D materials has significantly changed the path of FET based sensors. These materials are biocompatible, extremely sensitive, and feasible of batch mode fabrication. Patterning of 2D materials has further broadened the biosensor and bioelectronics applications. Numerous techniques for patterning of 2D materials have been recognized in the past decades [31-35]. It has just begun to apply a photolithography technique for patterning graphene films [36, 37]. Shortly the market for 2D materials is expected to compete for the reliability of silicon-based electronic sensor because of designing in micro and nanoscale. Furthermore, patterning these nanomaterials on various substrates holds promising development in healthcare wearable, and portable, flexible sensors [38, 39]. In this section, properties of the various 2D materials are discussed along with the feasibility of the patterning as well as there potential application in the biosensor domain.

There are various methods has been performed to acheive one atomic layer sheets. Micromechanical cleavage, also known as micromechanical exfoliation is one of the technique to get yielding films containing several layers of 2D materials [40]. Laser ablation and photo exfoliation are a controlled technique to achieve a 2D layer by removing material from the solid surface using laser beam [41]. Liquid-phase-exfoliation is a method to extract individual layers from solid materials in the liquid environment that involves three steps dispersion in a solvent, exfoliation, and purification [42, 43]. Chemical vapor deposition (CVD) is a widely used method to achieve 2D monolayers and fabricate large area films of single to few layers [44, 45]. This method is inexpensive and scalable to fabricate 2D material devices because of easy to transfer on a non-specific substrate like SiO_2/Si [46].

2.2.1 Graphene

Graphene is the first example of one atom thick layer of tightly bond sp^2 carbon, which provides a whole new range of unusual properties for investigating, as shown in Figure 2.3 (a). Many of the extraordinary properties of graphene stem from its peculiar electronic bandgap and dimensionality in which the electrons mimic relativistic particle [47]. Therefore electrons in graphene are usually known as massless Dirac Fermions, which is ideally suitable to study the relativistic effect of condensed matter physics [48]. As shown in Figure 2.3 (b) at a single point, the valence and the conduction band in graphene touch each other which compromise few electronics states near the Fermi level [49]. That is why graphene is usually called semi-metal or a zero bandgap semiconductor [50]. Single point contact makes graphene bandgap highly vulnerable to any change of electric field, doping, mechanical deformation, and adsorbates. This fragility of graphene bandgap opens the door to a new area in the sensing field encompasses some of the highly sensitive sensors [51, 52].

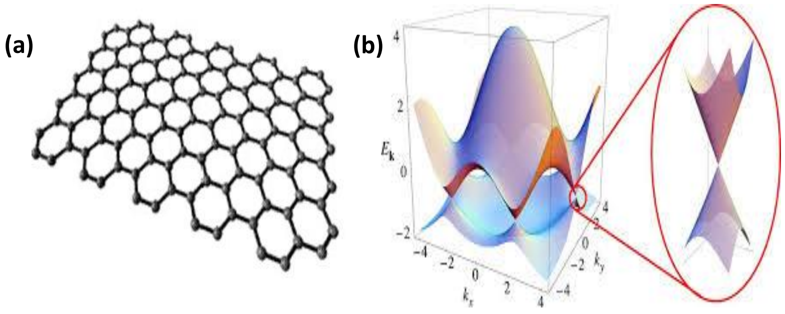

Figure 2.3 (a) Molecular bond of the Graphene (b) Band gap of Graphene [49].

A graphene-based FET biosensor was demonstrated by Yinxi et al. by detecting the E-coli bacteria [53]. CVD grown graphene was functionalized by linkers and anti-E-coli to achieve specificity, as shown in schematic Figure 2.4 (a). It is interesting to notice that, E-coli induce the hole on the graphene sheet and increase the conductivity on the left side of the Dirac point, as shown in Figure 2.4 (b). Drain current-gate voltage (I_D-V_{LG}) transfer curve of bare graphene, and functionalize steps of linkers, anti-E-coli, ethanolamine, and tween 20 is demonstrated in Figure 2.4 (c). Drain current-Drain voltage (I_D-V_D) also performed at different concentration of the E-coli bacteria to detect the limit of the sensor as illustrated in Figure 2.4 (d). The detection limit of graphene biosensor was found to be 10 CFU/mL, which vary the conductivity of the graphene by 3.24%. This graphene sensor demonstrates high sensitivity, easy to fabricate, high response time,

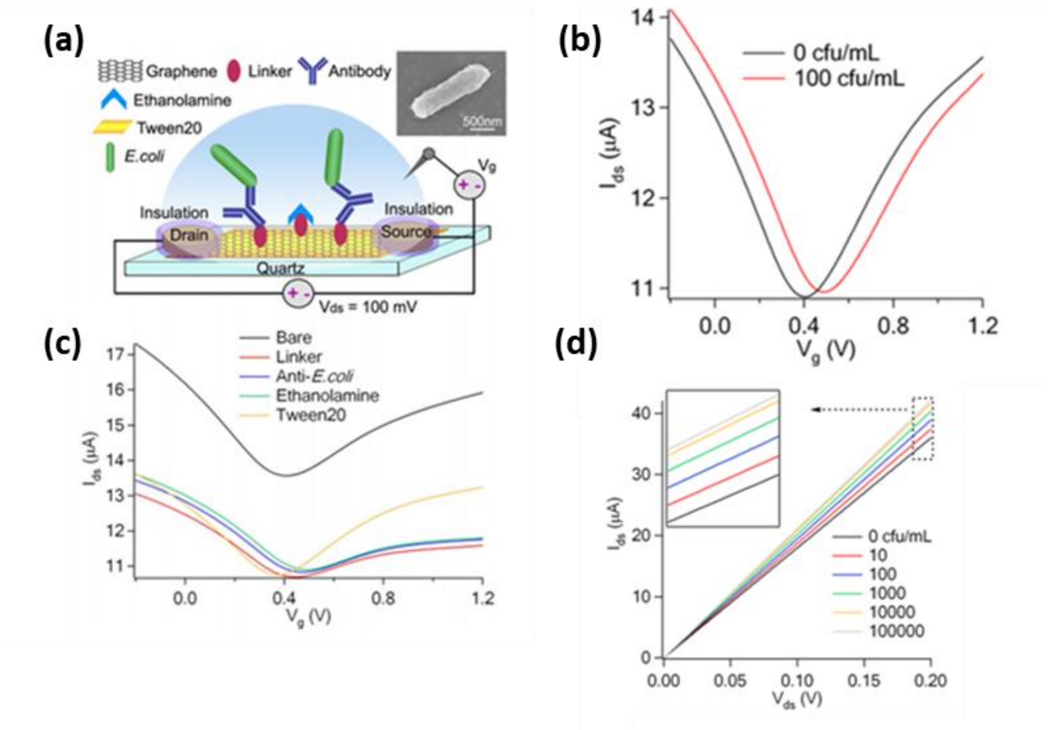

Figure 2.4: (a) Graphene based FET sensor for detecting the E-coli bacteria (b) I_D-V_{LG} curve of the FET before and after incubation of the E-coli bacteria; 100 CFU/mL. (c) I_D-V_{LG} of the bare graphene, linkers, anti E-coli, Ethanolamine, and tween20. (d) I_D-V_D characteristics at different concentration of the E-coli [53].

and label-free detection, which demonstrates the 2D materials has potential in the next generation of biosensing. However, the absence of a bandgap in graphene makes this material unsuitable in the semiconductor field. In case of the small bandgap/semimetallic semiconductors, electrons can tunnel through barrier very easily and increase the leakage current and reduce the performance of the sensor by increasing the subthreshold swing. Thus, researchers are diverted their interest to the other 2D single layer semiconducting material which has an appropriate bandgap to turn ON/OFF devices and negligible leakage current. In specific, considerable attention has been centering on the single-layer semiconducting materials, such as TMDs monolayer. 2D TMDs demonstrates very unique properties in the physical, optical, and electrical domains [54, 55].

2.2.2 TMDs

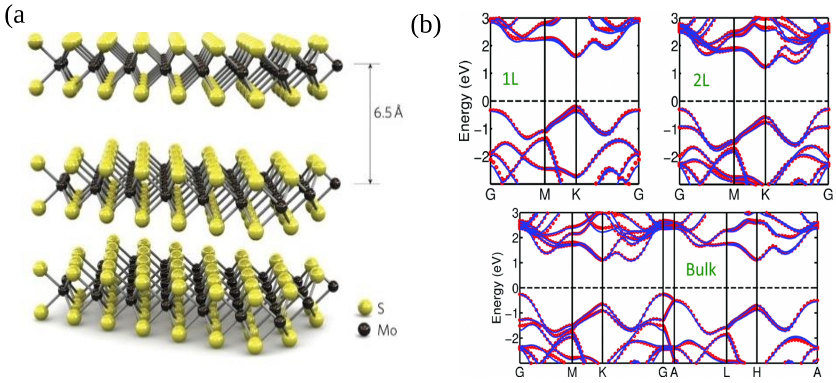

Figure 2.5 (a) Molecular diagram of MoS_2 (b) Band gap of MoS_2 [57]

TMDs monolayer is one atom thick semiconductor, where atomic composition contains MX_2 structure (M is a transition metal element from group IV, group V or group VI whereas X is a chalcogen). As shown in Figure 2.5 (a), TMDs form the layered structure of the arrangement X-M-X with two chalcogen atoms separated by transition metal atom in the hexagonal plane [56]. In semiconducting 2D TMDs, bulk layer posseses an indirect bandgap, whereas single layer contains direct gap. In case of Molybdenum disulfide (MoS_2), the bulk indirect bandgap is 1.3 eV while single layer direct band gap is 1.8 eV [57]. This direct bandgap makes the MX_2 semiconducting material suitable for many electronics and optoelectronic applications [58, 59].

The most studied 2D TMDs is MoS_2, which is similar to the graphene and has a thickness equivalent to the unit cell, which is hold by by weak van der Waals forces. MoS_2 planes contain molybdenum atoms sandwiched between two Sulphur atoms which demonstrate high electronic, mechanical, optical, and chemical properties [60, 61]. Therefore, 2D TMDs such as MoS_2 shows remarkable properties in the field of sensing applications [62, 63]. 2D TMDs are mostly stable in a liquid as well as oxygen comprising environmental medium because of the basal plane does not contain any dangling bonds, which facilitate their capable incorporation into sensing application [64]. Graphene and its oxides are semi-metallic contain either no or negligible band gap which limits this material to make more sensitive sensors (mostly FET based sensors). However, the overall sensitivity of device-based 2D TMDs, i.e., MoS_2 is much more significant because of the existence band gap (1.8 eV). The band structure in 2D MoS_2 contains d-orbital of Molybdenum in which 4 electrons from Mo fill the bonding state and the surface layers completed via lone pair of electrons [65, 66]. The d-orbital hybridization of MoS_2 leads towards the indirect to direct bandgap when it is exfoliated into a single layer, as shown in Figure 2.5 (b) [67, 68]. It has demonstrated that a single layer MoS_2 Field-effect transistor (FET) has turn ON/OFF ratio more than $10^{8,}$ which is specifically advantageous for highly sensitive FET based sensors. The maximum free career mobility was estimated 400 cm^2/Vs at room temperature whereas such high mobility of free carriers is impossible without high permittivity layers. The carrier lifetime of MoS_2 is ~100 ps, and the diffusion coefficient is ~20 cm^2/s [69]. This diffusion coefficient and carrier lifetime are apposite for making electrochemical and electric field-based sensors.

Figure 2.6 (a) shows the schematic of the MoS_2 based FET biosensor, where the first-time dielectric layer has functionalized with bio-receptors rather than the active material (2D materials) [16]. Because most of the specific molecules such as linkers and antibodies functionalize directly on bare channel surface which creates defects on the material and brings the considerable variation. In other words, when linkers/antibodies are directly attached to the bare channel, the transduction mechanism is the combination of the electrostatic gating, direct charge transfer, and mobility modulation. The combination of the gating effect can provide false results and does not measure the real concentration of the target molecules. Therefore, it is desirable to eliminate the density of defects by covering bare channel material with insulating material and then functionalize linkers and antibodies on the top of the insulator [5]. In such type of the architecture of FET biosensor,

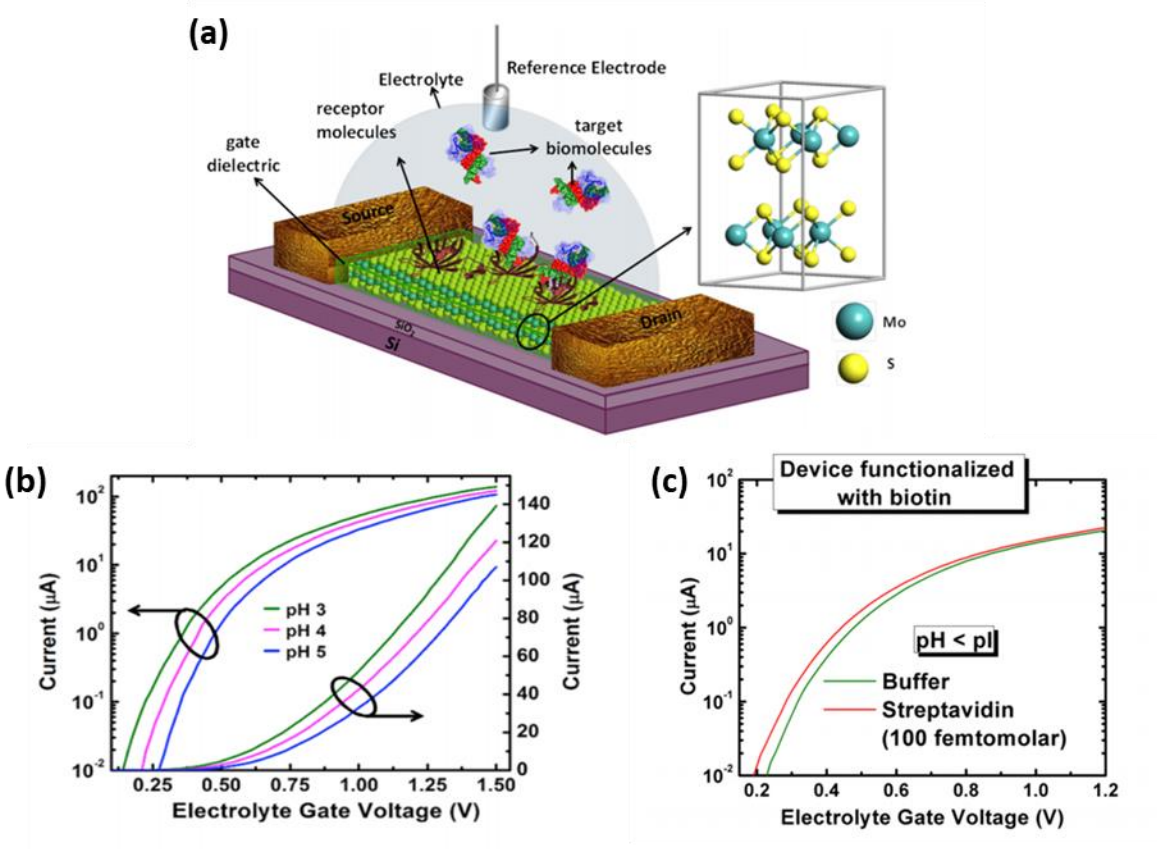

Figure2.6: (a) Schematic of MoS_2 biosensor with HfO_2 dielectric coating, bioreceptor, and target biomolecules with Ag/AgCl biasing from the electrolyte (b) I_D-V_{LG} profile of different pH (3,4, and 5) (c) I_D-V_{LG} profile of buffer and 100fM streptavidin [16]

Sarkar et al. achieved 723 sensitivity of pH sensing and 196 for the streptavidin at subthreshold region (SS) after functionalization of the dielectric layer as illustrated in Figure 2.6 (b) and (c) [16].

2.3 Challenges in 2D material: Transport and Scattering mechanism in 2D materials

The 2D material has the potential to create a significant impact on a large number of applications ranging from electronics to the energy system, catalysis, new generation sensors, etc. A large number of patents and articles are coming from the field of the 2D materials regarding synthesis, physical properties, and their applications. When graphene added in the 2D material family, it shows incredible achievement in the area of material science. Then, other materials have been investigated who has a unique bandgap structure, chiral fermions, biocompatibility, and rendering the quasiparticle in it formally identical to massless [48]. These properties of the 2D material can be useful in real applications such as FET based biosensors by enhancing the sensitivity and reliability of detection at low power [70]. However, the plane of the 2D layer has confined the transport and scattering of the carriers [71]. The following primary scattering mechanism that affected the mobility of the carriers: (a) acoustic and optical phonon scattering; (b) surface interface phonon scattering; (c) Coulomb scattering at charge impurities; (d) roughness scattering. The amount of scattering phenomena affect the carrier transport governs the thickness of the layer, temperature, carrier density, effective mass, phonon, and electronic band structures [72].

Coulomb scattering is also one of the critical cause to reduce the mobility of electrons in 2D materials. This phenomenon happens because of random charge impurities located in the 2D material or on its supporting surface [73]. The dielectric environment can improve mobility, as demonstrated for graphene [74] as well as for MoS_2 [75]. The bandgap and carrier concentration in the 2D material can tailor by using ionic impurities, but the mobility reduces because of scattering, the choice of doping depends upon the specific device performance. However, in extremely thin 2D materials (single atomic layer), the effect of roughness scattering and surface phonon is significant [76, 77].

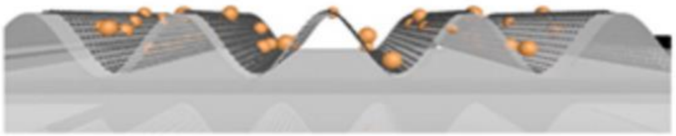

Figure2.7: Scattering effect from substrate [80].

However, despite from different scattering phenomenon in 2D materials, the presence of substrate scattering confines the electron mean free path to less than a micron which considers the significant barrier to developing devices from these low dimensional materials as shown in Figure 2.7 [78, 79]. Interface between low dimension material and supporting substrate plays a critical role in the performance of the sensing field or any other devices [80]. For instance, SiO_2 is the standard substrate for 2D material device fabrication which seems highly disordered topographically and chemically as well as it may harbor atmospheric gases, unknown functional group, chemical adsorbates and charges along with corrugation. This type of interface distortion affects the repeatability of the sensor data and decrement of mobility disturbs the response time and sensitivity of detection.

2.4 Solutions for Scattering

The 2D material has always required the support to fabricate a device. The surface of the supporting substrate is highly disordered topographically as well as chemically for such thin nanomaterials, which creates a scattering phenomenon and reduce the overall mobility and the consistency of the device [81]. There are various attempts have been taken to increase the mobility of 2D nanomaterials by upgrading the substrate. The high dielectric medium can be useful to reduce coulombic scattering and increase the mobility of the film. Lin *et al.* have demonstrated by coating a thin layer on the supporting substrate of electrolyte PEO and $LiClO_4$,which increase the mobility and reduce the contact resistance [82]. Bao et al. demonstrated that Poly(methyl methacrylate) (PMMA) could provide high dielectric support and enhance the mobility and transport of electron in the MoS_2 monolayer by eliminating the chemical bonding and surface roughness at the supporting substrate interface [83]. However, to reduce trapping of charges at the interface and upgrade transport properties, the 2D material should be suspended without any support seems a promising strategy towards high sensitive sensors and digital electronic devices. It has reported that suspended 2D material shows more mobility than the supported one [84].

2.5 Fabrication of Suspended 2D FET process flow

It has demonstrated that single and few layers of MoS_2 encapsulated with the high dielectric layer on a supporting substrate is very useful for FET's application [85, 86]. However, substrate disorder topography, unknown functional group, chemical adsorbates reduce the conductivity of the 2D material. To abbreviate these consequences and achieve high conductivity in 2D MoS_2 Jin *et al.* and coworkers demonstrated suspended MoS_2 FET on SiO_2 substrate by means of e-beam lithography and etching of insulator layer i.e. SiO_2 [87].

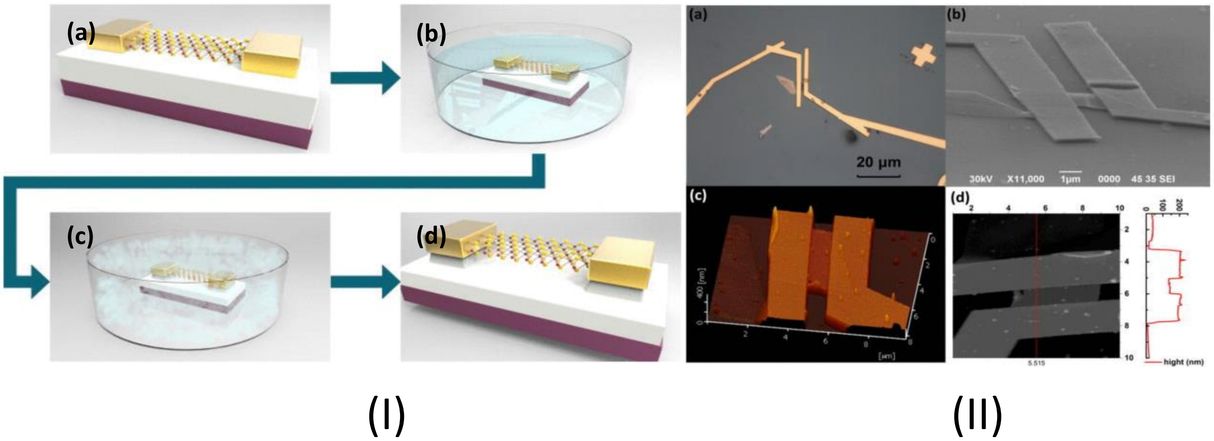

Figure 2.8
(I) MoS_2 device fabrication process (a) creating contacts via e-beam lithography on the top of supported MoS_2 crystal (b) Etch SiO_2 in Buffer Oxide Etch and (c) followed by entanol washing and then critical point dryer is used to remove all wet contaminants (d) Final schematic
(II) Final device image of suspended MoS_2 underneath the electrodes (a) optical microscope (b) SEM (c) AFM (d) AFM line profile [88].

As shown in Figure 2.8 (I) (a) Mechanical exfoliated MoS_2 transferred on an n-doped SiO_2/Si substrate (300nm SiO_2 thickness) followed by e-beam lithography to create metal electrode for electrical characterization. Then, to acheive suspended MoS_2, oxide layer etched in BOE (Buffer Oxide Etch) solution has been carried out to etch away half of the oxide thickness as shown in Figure 2.8 (I) (b). Afterward suspended MoS_2 device carefully transferred in ethanol solution and then dried out in critical point dryer (CPD) as illustrated in Figure 2.8 (I) (c) & (d). Figure 2.8 (II)

(a) shows the optical image of suspended MoS_2 and gold electrode whereas Figure (II) (b) (c) (d) shows SEM, AFM, and a line profile of AFM image. In this experiment Jin *et al.* and co-worker verified the mobility of suspended MoS_2 is 0.9 cm^2/Vs and supported one is 0.1 cm^2/Vs. Whereas on/off ratio is improved an order of magnitude in the suspended one, i.e., 10^5 [88]. This process of wet etching of SiO_2 underneath of 2D materials process has been employed in different ISFET sensor, where electrode spacing varies from the 1 µm to 2 µm.

2.5.1 Suspended MoS_2 FET device

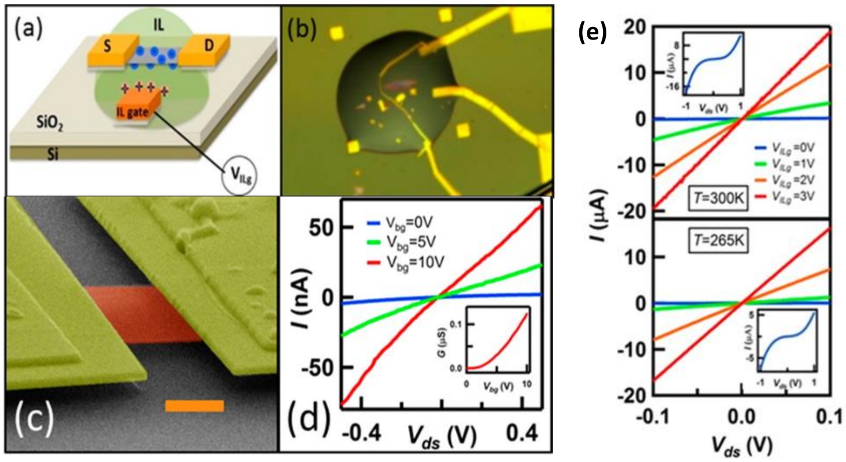

Figure 2.9 Ionic gating of suspended MoS_2 device (a) Schematic and (b) optical image (c) SEM image of suspended device (d) I-V characteristics of different bias voltage (e) I-V transfer curve of suspended MoS_2 at two different temperature [84].

Ionic liquid salt contains mobile ions (cations and anions), which are useful for ISFET sensing [89]. When an electric field is applied, ions in the liquid accumulate, forming an electric double layer on the top of the device by creating a nanogap capacitor with large capacitance. Ionic gating can induce the charge density is usually an order magnitude greater than the traditional back gating. Wang *et al.* and coworkers demonstrated the effect of ionic gating in the suspended MoS2 monolayer [84]. In this case, they have eliminated the scattering effect comes from the SiO_2/Si substrate as well as shown the top and bottom side of electric double layer gating. A droplet of ionic liquid deposited, as shown in the schematic of Figure 2.9 (a), and an optical image in Figure 2.9 (b). These devices usually suspended after addition of the Ionic liquid (IL). In this device, the conductance of typically increase 10^3 or 10^4, and the enhanced mobility found 46 $cm^2/(V\ s)$. Fabrication process to achieve suspended layer is same as mentioned in above [82]. The mechanically exfoliated MoS_2 sheet is coupled with Ti/Au electrodes and acquire free-standing layer by etching SiO_2 in hydrofluoric acid, as shown in Figure 2.9 (c). Suspended MoS_2 devices characterized in vacuum environment at room temperature as illustrated in Figure 2.9 (d), I-V characteristics at a different back gate voltage (mobility ~2.1 $cm^2/(V.s)$). A suspended IL gating device improves the performance regarding conductance increment in order of 103 or 104, and mobility of the device is 46 $cm^2/(V\ s)$. To recognize carrier transport mechanism in the fabricated devices by applying IL gating, Wang *et al.* and co-workers measured their transfer curve characteristics at different gate voltage as shown in Figure 2.9 (e) at temperature 300K and 265K. As gate voltage increased, the device conductance also improved from ~1 to ~180 µS, which indicates the Fermi level is shifted near to conduction band. As shown in Figure 2.9 (e) inset at lower gate voltage I-V curves are linear, but it becomes nonlinear at higher gate voltages. This IL gating suspended devices demonstrate such a drastic enhancement in conduction, which suggests that IL reduces the Schottky barrier at the interface of metal and the semiconductor. Also, the improvement in mobility indicates that charge impurities reduced because of the IL help to reduce electron scattering. These type of structure is very suitable for building the suspended reliable pH sensor.

2.6 Hypothesis

Among various 2D materials, TMDs has demonstrated impressive performance in FET based biosensor because of the tunable bandgap, biocompatibility, and high mobility. The nanometer thickness of these materials requires supporting substrate (SiO_2/Si) to fabricate the FET devices. However, supporting substrate has uneven morphology, harbor atmospheric gases, unknown functional group, corrugated charges, and chemical adsorbates, which degrades the transport properties of the 2D materials by scattering phenomenon. This effect implies that the interface control between 2D material and the supporting substrate is essential due to the unreliability output response from every single fabricated sensor. In recent years, many works have been published to reduce the scattering effect by increasing the dielectric properties and reducing the surface roughness of the supporting substrate by using PMMA and PEO [90]. However, due to biocompatibility, fabrication, and reproducibility issues, these layers cannot be employed in the biosensor domain. The other method to make freestanding 2D materials without interacting with the supporting substrate. The previous work for the fabrication of free-standing 2D material devices achieved by using the acid release of underlying SiO_2 substrates [91]. Freestanding 2D TMDs has shown improvement of carrier transport as compared to the supporting substrate. However, this type of fabrication possesses etching of SiO_2 underneath of 2D materials, which affects the purity and electronic properties of the 2D materials and counterfeit the idea of reliable and precision sensing of every single device. Secondly, this process consists of wide spacing in-between two electrodes due to which the 2D materials sags between electrodes, as demonstrated in Figure 2.10 (a) and (b). Therefore, the coating of another layer i.e. linkers, antibodies, and dielectric layer is impossible, which elude the specific detection of the biomolecules and other elements. In this architecture, the top gate transition is also impossible due to sagging nature of 2D TMDs, which leads to the only back gate transition. However, back gating requires more power than the top gate because of the thicker dielectric layer and reduce the mobility by two folds as shown in equation 2.1.

$$\mu_n = \frac{L}{CW} \cdot \frac{\Delta I_{ds}}{\Delta V_g} \cdot \frac{1}{V_d} \ldots\ldots\ldots\ldots\ldots\ldots\ldots\ldots (2.1)$$

Where μ_n is the mobility of the electron, L is the length of channel, C is the capacitance, W is the width of the transistor, $\Delta V_g$is the change in gate voltage, ΔI_{ds} and V_d are drain current and the voltage respectively. From the above equation, the mobility of the electron is inversely proportioned to the gate voltage. However, ΔV_g depends upon the thickness of the dielectric layer, which is defined as

back gate thickness

$$t_{\text{suspended, BG}} = (t_{\text{supporting}})+(t_{\text{oxide}})+(t_{\text{vacuum}})$$

and top gate thickness

$$t_{\text{suspended, TG}} = (t_{\text{oxide}})$$

Therefore, ΔV_g is much larger in the back gate than the top gating and increase the overall mobility i.e. large electrostatic effect on channel material with the small change in gate potential. Due to which top gate transition is important in 2D FET sensor to build highly sensitive and low power device. Finally, the freestanding 2D TMDs achieved using E-beam lithography technique to engrave electrodes, which is not suitable for large-scale fabrication. Therefore, the objective of this research is to study the scattering phenomenon at the interface of supporting substrate and 2D

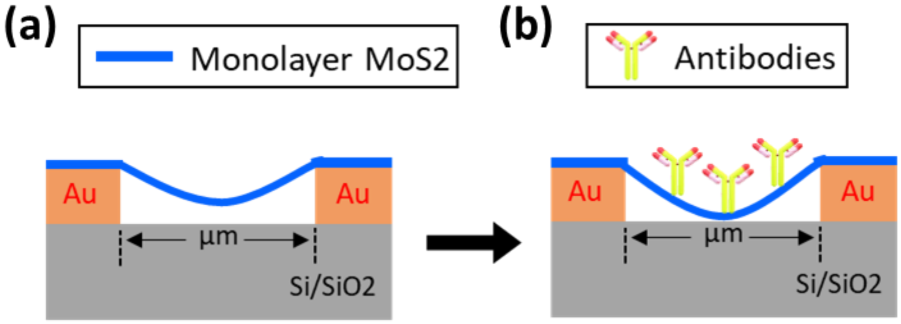

Figure 2.10 (a) Free standing layer of 2D TMDs (MoS_2) is sagging on wide spacing electrode and (b) functionalization of antibodies, which might interact with supporting substrate

material. Secondly, synthesize the 2D TMDs materials to fabricate freestanding top gate 2D based FET biosensor via photolithography without any wet chemistry.

2.7 Dissertation Objectives

The ***objectives*** of this thesis are to fabricate suspended 2D TMDs FET sensor without any interface effect from supporting substrate for reliable sensing. *(i)* 2D TMDs plays a pivotal role in channel material to achieve a better electrostatic effect by a small variation in gate potential. Therefore, it is essential to synthesize highly crystalline single-layer TMDs for creating ohmic contact with gold electrodes and achieve high gating effect. *(ii)* Freestanding of 2D materials can be achievable through nano-gaps without any wet etching of SiO_2. Therefore, the other task of this research is to fabricate nano spacing electrode through a novel self-assembly photolithography technique, transfer 2D materials by innovative dry stamping method, and evaluate the traditional top gate FET characterization. *(iii)* Finally, test this suspended 2D material devices in terms of the sensor by attaching antibodies of E-coli bacteria to the dielectric layer and check the sensitivity and lower detection limit of this pathogens through FET characterization.

2.7.1 Synthesis of 2D materials via CVD and FET characterization

Study the effect of growth parameters on 2D material morphology and achieve high crystalline nature of TMDs flakes. Two-dimensional (2D) nanomaterials, such as transition metal dichalcogenide (TMD) provide an opportunity to make ultra-sensitive sensors because of its atomic layer [92]. The existence bandgap of TMDs shows tremendous potential for detecting biomolecule (E-Coli) through FET biosensors. In this chapter, different TMDs have been investigated by tuning the bandgap, structure, and achieve crystallinity through the CVD technique. The characterization of TMDs crystallinity was evaluated through Raman, X-ray powder diffraction (XRD), Scanning electron microscope (SEM), Atomic Force Microscope

(AFM), Transmission electron microscopy (TEM), and Energy Dispersive Spectroscopy (EDS/EDAX) mapping. FET characterization is also performed to check the work function of MoS_2 TMD with metal electrodes.

2.7.2 Fabrication of nanogaps and characterization of suspended FET

The nanogap fabrication was achieved via a novel self-assembly technique, where chromium (Cr) was used as an inflation layer. The optimization of nanogap achieved by controlling the expansion of the Cr layer and the thickness of the gold electrodes. Wafer-scale fabrication of nanogaps attained in the controlled environment. A novel dry transfer method of 2D material was developed, which provides proper placement of CVD grown 2D TMDs on the desired area by keeping its crystallinity intact. These nano-spacing electrodes not only give suspension but also provide robust strength to the atomic layer, which remains freestanding after coating of the Hafnium oxide (HfO_2) as well as linkers and antibodies as explained in the schematic Figure 2.11 (a) and (b). The freestanding of the MoS_2 layer was characterized by using TEM, electron energy loss spectroscopy (EELS) mapping, AFM mapping, and Raman mapping. The FET characterization such as subthreshold swing and the threshold voltage of suspended MoS_2 and WSe_2 performed with top gate and back gate.

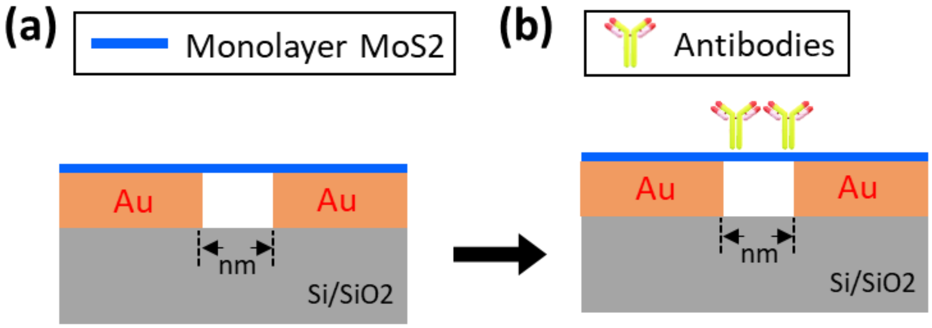

Figure 2.11 Free standing layer of 2D TMDs (MoS_2) is robust on nano spacing electrode and (b) allows the functionalization of antibodies without interacting with supporting substrate

2.7.3 Testing pH and E-coli bacteria concentration via suspended FET biosensor

The pH sensing on the HfO_2 strongly depends upon the protonation and deprotonation of ions. The pH value of the electrolyte solution varies the charge on the HfO_2 dielectric surface, which was measured through suspended MoS_2 FET characterization. Different pH values were performed and achieved ultra-high sensitivity on suspended ISFET sensor. Secondly, E-coli negatively charged biomolecule was used to check the specificity of the biosensor. Self-assembly molecule (SAM) was optimized to fabricate appropriate sensing of the E-coli. The deviation of the threshold voltage and the conductance of a transistor can be used to measure the number of charged biomolecules (E-coli) onto MoS_2 quantitatively. For reliability, three different suspended biosensor was fabricated and compared the sensitivity.

After completion of this research, it is expected to understand the fundamental nature of the 2D materials by tuning the composition, which leads to change in the properties at the quantum level. An innovative process flow is developed to distinguish between the suspended and supported 2D material electronic devices and learn the effect of the scattering. Finally, investigate the suspended device in terms of there reliability by sensing the pH and biomolecules.

CHAPTER 3 SYNTHESIS OF 2D MATERIALS VIA CVD METHOD AND FET CHARACTERIZATION

3.1 Synthesis of 2D materials

Transition metal dichalcogenides (TMDs) have attained much interest due to their two-dimensional structures and novel properties [93, 94]. In monolayer, the band structure of few TMDs transfer from indirect to direct bandgap due to interlayer interaction [56]. These properties of TMDs appeal to several potential applications in molecular electronics, optoelectronics, catalysis, and battery system [61, 95]. TMDs such as molybdenum disulfide (MoS_2), molybdenum diselenide ($MoSe_2$), Tungsten disulfide (WS_2) and Tungsten diselenide (WSe_2) most extensively studied due to its promising properties in the field of electronics to energy conversion [75, 96]. Many approaches have been considered in an account like chemical exfoliation, mechanical exfoliation, and chemical vapor deposition (CVD) to obtain a high quality single atomic layer of 2D TMDs [97-99]. Among all synthesis processes, CVD method draws much attention because of the scaled-up production and give better control over the sum of layers if growth happens via surface-mediated synthesis. All the CVD method reported to date for growing MoS_2 is used chemically inert solid-state dielectric substrates [100].

3.2 Chemical Vapour Deposition

Challenges involved in the CVD growth of the high crystalline TMDs layer are (a) continuous flow of Sulphur (b) amount of Transition metal oxide (TMO) and sulfur (c) Distance between the TMO and Sulphur (d) Growth time and (e) most important is temperature. The optimization of these parameters is vital to achieving the high crystalline TMDs on SiO_2/Si wafer. The flow of Sulphur optimized by the appropriate placing of the boat in the quartz tube to achieve a continuous stream at growth time. However, the amount of TMO is significant for high crystalline flakes because it is found in our previous CVD growths experience if the quantity of precursor is increased then the bulk layer of TMD is deposited on the SiO_2/Si substrate. For instance, MoO_3 can quickly reduce at elevated temperature in the presence of Argon gas to form monolayer MoS_2, but the amount of MoO_3 is increased then the bulk layer gets deposited on the dielectric surface due to a higher amount of MoO_3 reduction. Therefore, the amount of transition metal oxide (TMO) (such as MoO_3 and WO_3) is optimized to gain high crystalline atomic layer. The distance between TMO boat and Sulphur boat is also an essential parameter because it determines the concentration of Sulphur in every zone of the quartz tube at growth time. It is found that if the TMO boat is present high concentration zone, then the star flakes are deposited which consists of a high percentage of the Sulphur whereas if the distance is far then immature flakes is formed which consists of the bulk nucleation. Both types of crystals are resistive in nature, which impede the transport of the electron and reduce the sensitivity of sensor [101]. The other two parameters are the backbone of the TMDs growth i.e. growth time and temperature. As per our experimence it was found that if the pressure is increased then the reduction of MoS_2 flake is continuous with Sulphur which turns into star flakes and if the pressure is reduced then the immature flake is formed as well as other particles such as Molybdenum oxy-sulphide(MoOxS) and metallic MoO_2 are also present on the substrate [102]. Finally, temperature optimization is essential for high crystalline TMDs growth. These parameters are optimized in our studies to achieve a single atomic layer of the 2D TMDs.

3.2.1 Temperature and precursors optimization

Figure 3.1 (a) illustrated CVD unit assembled in our lab to grow 2D materials, where Sulphur/Selenium (chalcogen) are placed to the upstream whereas sprinkled TMO is used to synthesized nanomaterials in Ar environment. The atomic layer 2D MoS_2 were grown on a SiO_2/Si

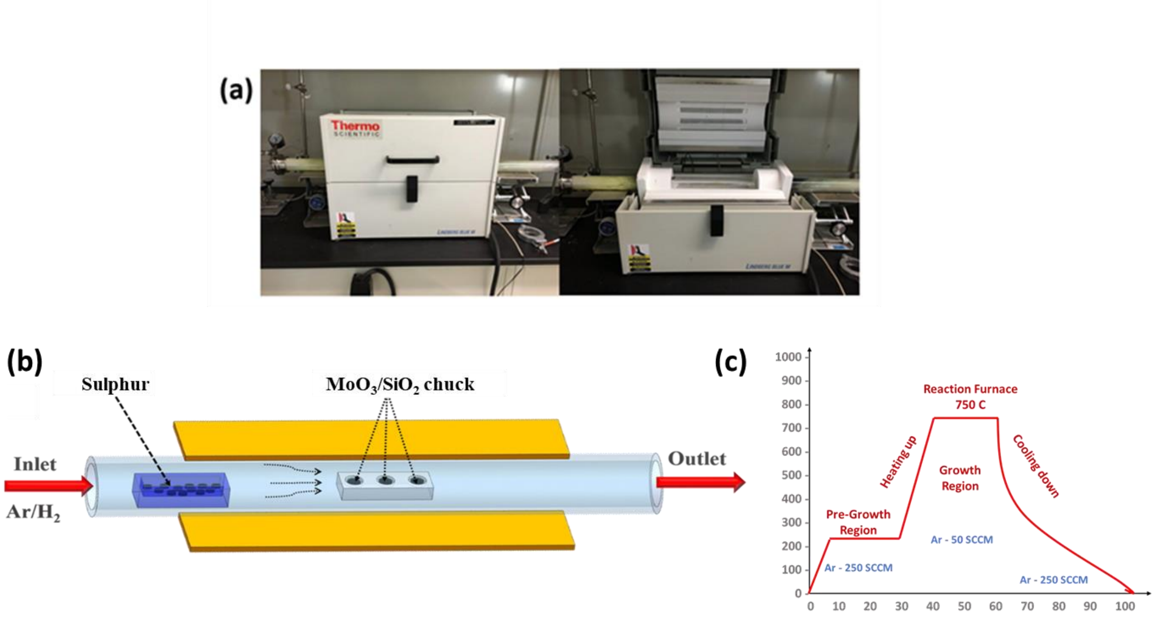

Figure 3.1. (a) In-house CVD for TMDs growth (b) Schematic representation of the experimental setup for CVD growth. (c) Process flow of typical MoS_2 growth.

substrate by using the CVD method as schematically illustrated in Figure 3.1 (b). To grow MoS_2 (growth procedure same for all 2D TMDs), a ceramic boat contains sprinkled MoO_3 precursor underneath of the SiO_2/Si chuck (1 × 1 cm^2) is placed at the high-temperature zone of the horizontal quartz tube and a small quartz boat contain sulfur pallets are kept in low-temperature region. CVD process was carried out at different temperature *viz.*, 650º C to 800º C to find the optimal growth conditions for MoS_2 enriched with high crystallinity. The typical process flow of CVD grown MoS_2 as shown in Figure 3.1 (c), where Argon gas (Ar) pass for 250 sccm for 20 mins to remove all environmental gases and then ramp up the temperature till 760°C in 15 mins and maintain the temperature for 20 mins called as growth time to achieve 2D TMDs followed by cool-down process.

Initially, the different temperature has been categorized to obtain a high crystalline monolayer of MoS_2. It is determined that the low-temperature growth of MoS_2 demonstrate the bulk deposition of material on Si/SiO_2 substrate [101] as illustrated in the SEM image of Figure

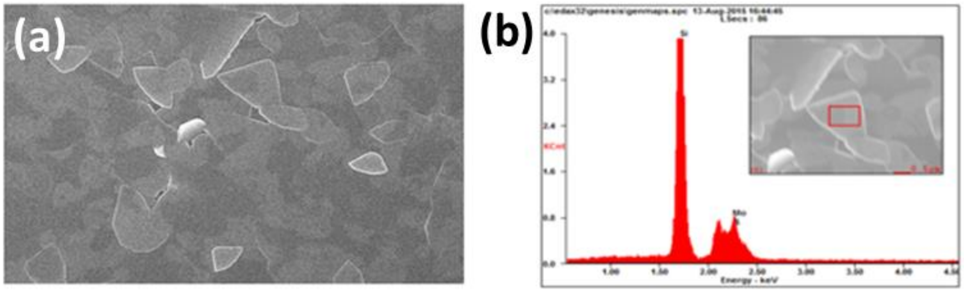

Figure 3.2: (a) SEM image of MoS_2 CVD growth at low temperature (b) EDAX of MoS_2 at low temperature

3.2 (a). The corresponding EDAX elemental profile exposed the non-homogeneous distribution of Mo and S atoms in a nanosheet on the SiO_2/Si substrate, as shown in Figure 3.2 (b). During MoS_2 growth, it was hypothesized that the kinetics of sulphurization process affects the layer orientation and morphology of nanosheets. At 650° C, due to the low reactivity of sulfur, their interaction with Molybdenum precursors proceeds sluggishly, which provides fewer nucleation sites and leads to the formation of few-layered planar nanosheets. At low temperatures, 600-700 °C the reaction is incomplete and leads to the formation of intermediate products due to the slow activity of reactants [92, 103]. The intermediate products are MoO_{3-x} and MoO_2, which are not adequately reduced on the SiO_2/Si surface, as shown in the following chemical reaction 3.1 and 3.2.

$$MoO_3 + \frac{X}{2}S \rightarrow MoO_{3-x} + SO_2 \ldots\ldots\ldots\ldots\ldots (3.1)$$

$$MoO_3 + \frac{1}{2}S \rightarrow MoO_2 + \frac{1}{2}SO_2 \ldots\ldots\ldots\ldots\ldots (3.2)$$

XRD spectra were performed to confirm the bi-product such as MoO_3 and MoO_2 with the MoS_2 nanoflakes. This characterization suggested that the reaction does not take place entirely at low temperature i.e. 650° C as shown in Figure 3.3 (a). Whereas Figure 3.3 (b) shows the optical image of all bi-products including sufficiently reduced MoS_2, this flake is not useful for the FET based biosensors due to the presence of impurities and bulk nature of MoS_2. For further evaluation of

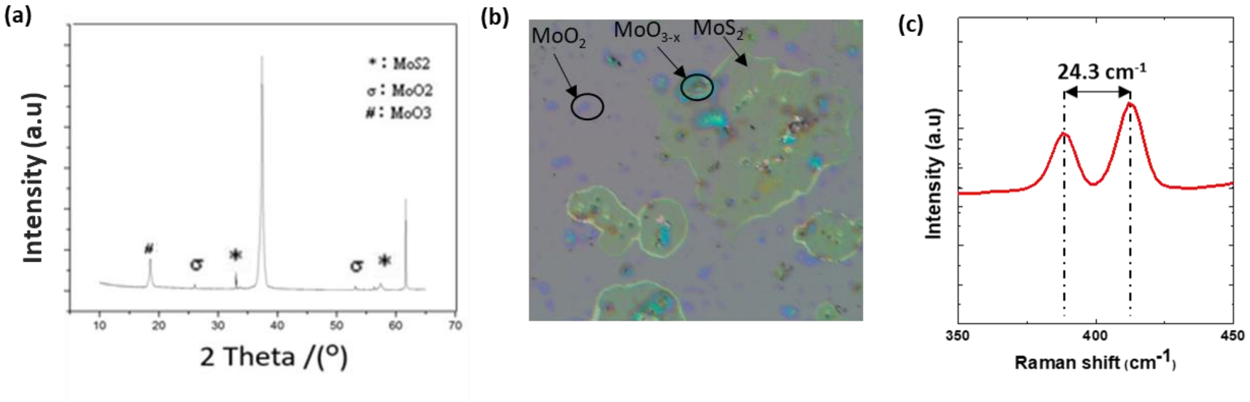

Figure 3.3: (a) XRD of MoS_2 growth at lower temperature (b) Optical image of the biproducts at lower temperature (c) Raman mapping of bulk MoS_2

bulk material, Raman spectra were performed on the low temperature deposited MoS_2 flakes, which shows the nanosheets encompasses multiple numbers of layers as illustrated in Figure 3.3 (c). However, a bulk sheet of TMDs consists of the indirect bandgap due to which the electron is not able to tunnel properly from valence band to conduction band and leads to the reduction of the mobility.

For achieving the proper reduction of the transition metal oxide (TMO), we emphasize several experiments via elevating temperature by 10° C. After some iteration, at 760° C, Sulphur reactivity is augmented and produces many nucleation sites which tend to form a large number of nanosheets on the surface of SiO_2. At elevated temperature, reductive nature of SiO_2 also enhances the reduction of MoO_3 to convert into MoO_{3-x} ($x>1$) nucleolus, which further reduces by the diffusion of Sulphur vapors and converts into metallic MoO_2. More sulfur vapors diffuse along the lateral side, which provides atomic layer orientation of MoS_2 nanoflakes [104] as shown in the following chemical reation 3.3, 3.4 and 3.5.

$$MoO_3 + \frac{X}{2}S \rightarrow MoO_{3-x} + SO_2 \ldots\ldots\ldots\ldots\ldots.(3.3)$$

$$MoO_{3-x} + \frac{X}{2}S \rightarrow MoO_2 + SO_2 \ldots\ldots\ldots\ldots\ldots(3.4)$$

$$MoO_2 + \frac{X-7}{2}S \rightarrow MoS_2 + \frac{3-X}{2}SO_2 \ldots\ldots\ldots\ldots\ldots(3.5)$$

In our inhouse CVD unit, we achieved a high-quality atomic layer of the MoS_2 at 760°C, as shown in Figure 3.4 (a) and (b). The density of the triangles can be varied on the SiO_2 surface by managing the concentration of TMO. The high amount of the TMO leads to the bulk formation of the MoS_2 with impurities. Therefore, it is important to maintain the concentration of TMO precursors underneath the growth substrate. In our case, we have sprinkled very small amount of the MoO_3 or WO_3 on the ceramic boat to achieve a high quality of triangle with a medium density, as shown in Figure 3.4 (c).

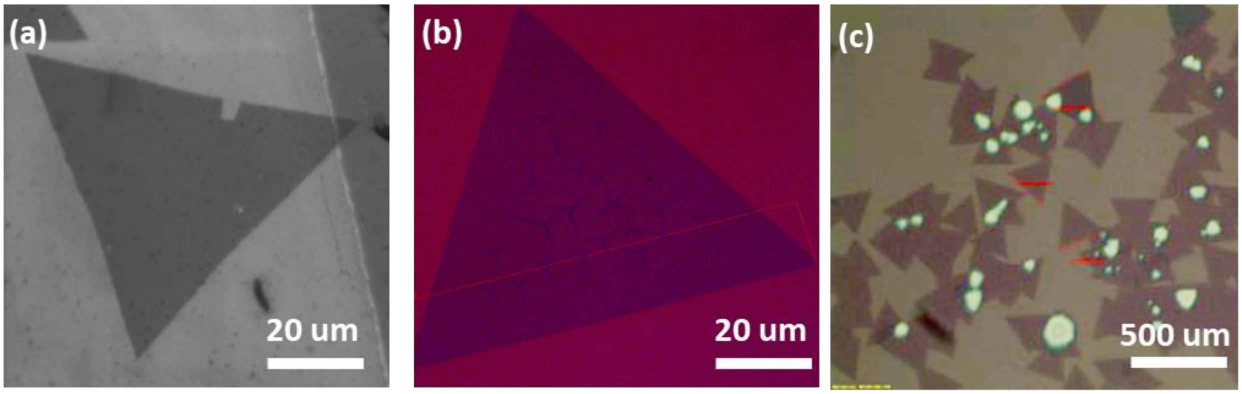

Figure 3.4: (a) SEM image of large MoS_2 (b)Optical image of MoS_2 high magnification (c) Optical image of MoS_2 at low magnification

The other important factor, which creates the TMD, i.e. MoS_2 sharp edges is the amount of Sulphur (selenium for selenide based TMDs), sharp edges related to the high crystalline nature of atomic layer. The crystalline TMDs exhibits the appropriate ratio of the Mo and S atoms in the atomic layer crystal (Mo:S::1:2). Therefore, it is essential to maintain the appropriate amount of the S content while growing because it attributes the electronic properties (crystallinity) of TMDs.

3.2.2 Pressure Optimization

The other parameter interrelated the Sulphur/Selenium concentration in the tube is pressure [105]. As the Sulphur/Selenium evaporate in the CVD tube, the pressure also gets increased. This pressure can be controlled by outgoing flow and the position of the Sulphur/Selenium boat, which maintain the amount of sulfur/Selenium content in the tube. The following discussion of growth based on the pressure dependency i.e. chalcogen of the TMDs structure. In this section, we have iterated different concentration of Sulphur for achieving atomic layer MoS_2, whereas the same parameters are implemented for selenium and another atomic layer growth. As the pressure is close to the atmospheric pressure (0.5-1 KPa), then the rectangular shape crystal form, which shows the TMO i.e. MoO_3 is not adequately reduced as shown in Figure 3.5 (a) and (a'). When the further increase of the pressure (Sulphur content), these rectangle granular convert into the hexagonal shape and leading towards the atomic layer as shown in Figure 3.5 (b) and (b'). However, this type of structure does not show excellent electronic properties due to the uneven concentration of Mo and S atoms. Secondly, the flakes consist of multiple layers, which leads to the indirect bandgap

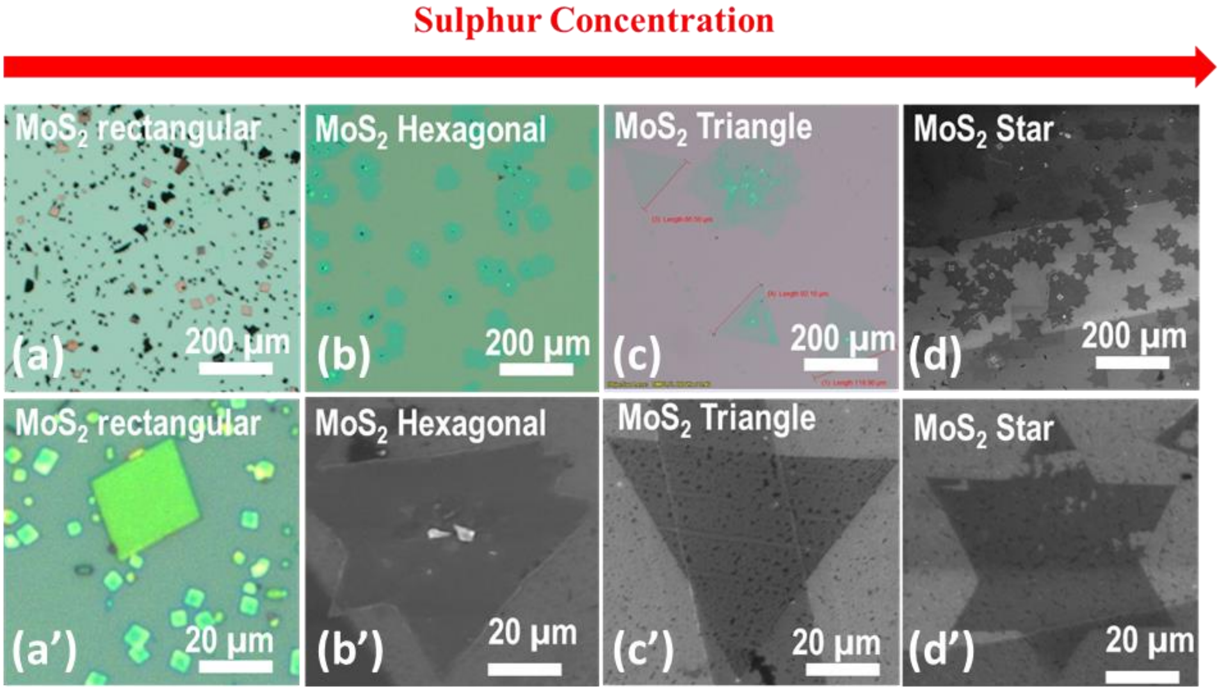

Figure 3.5: Morphology of flakes associated with Pressure, which is related to the sulfur concentration while growing MoS_2 in the CVD (a) low magnification image of square flakes at 0.5-1 KPa (a') high magnification image of square flake at 0.5-1 KPa (b) low magnification image of hexagonal flakes at 1 KPa (b') high magnification image of square flake at 1 KPa (c') low magnification image of triangular flakes at 5 to 8 KPa (c') high magnification image of triangular flake at 5 to 8 KPa (d) low magnification image of star flakes at <20 KPa (d') high magnification image of star flake at <20 KPa

of the MoS_2. When the pressure is further increased from (5 to 8 KPa), the MoO_3 powder reduced totally and form a triangular shape crystal. This triangular shape has the proper amount of Mo and S distribution and consists of the single atomic layer, which possesses the direct bandgap, as shown in Figure 3.5 (c) and (c'). As the maximum pressure reaches (<20 KPa) this triangular shape converted into a star and other morphology as shown in Figure 3.5 (d) and (d'). In conclusion, the Sulphur content is significant to determine crystallinity and the shape of the atomic layer, which define the electronic properties of the 2D materials via tuning the bandgap.

3.2.3 Growth Surface Optimization

The catalyst i.e. surface is also an essential factor for the structural growth of the TMDs. To study the different orientation, we have grown TMDs on SiO_2 and the 3D structure of carbon material. The quartz and SiO_2 surface provide lateral growth of the atomic layer due to the diffusion of sulfur on the edges of nucleation of MoO_3 at high temperature (discussed in section 3.2.1). Therefore these surface have shown growth of atomic layer parallel to the surface i.e XY plane, as shown in Figure 3.6 (a) and (a'). However, in the 3D structure of the carbon cloth (CC), the growth is dramatically augment the reduction of MoO_3 and promote the formation of MoO_{3-x} ($x>1$) to react with selenium/Sulphur vapor which further converts into $MoSe_2$/MoS_2 layers. The reducing of MoO_3 to MoO_{3-x} ($x>1$) suggest that carbon is more reductive at elevated temperature. Carbon assisted in creating MoO_{3-x} ($x>1$) on the layer of CC, and it is well known that further reduction of $MoO3_{-x}$ ($x>1$) to MoO_2 at present of selenium/sulfur vapor and hydrogen generates TMDs (MoS_2 and $MoSe_2$) layers. In addition, the defective nature of CC makes it more reactive for molybdenum source, creating a sizeable interacting surface for MoO_{3-x}. Thus, carbon fibers

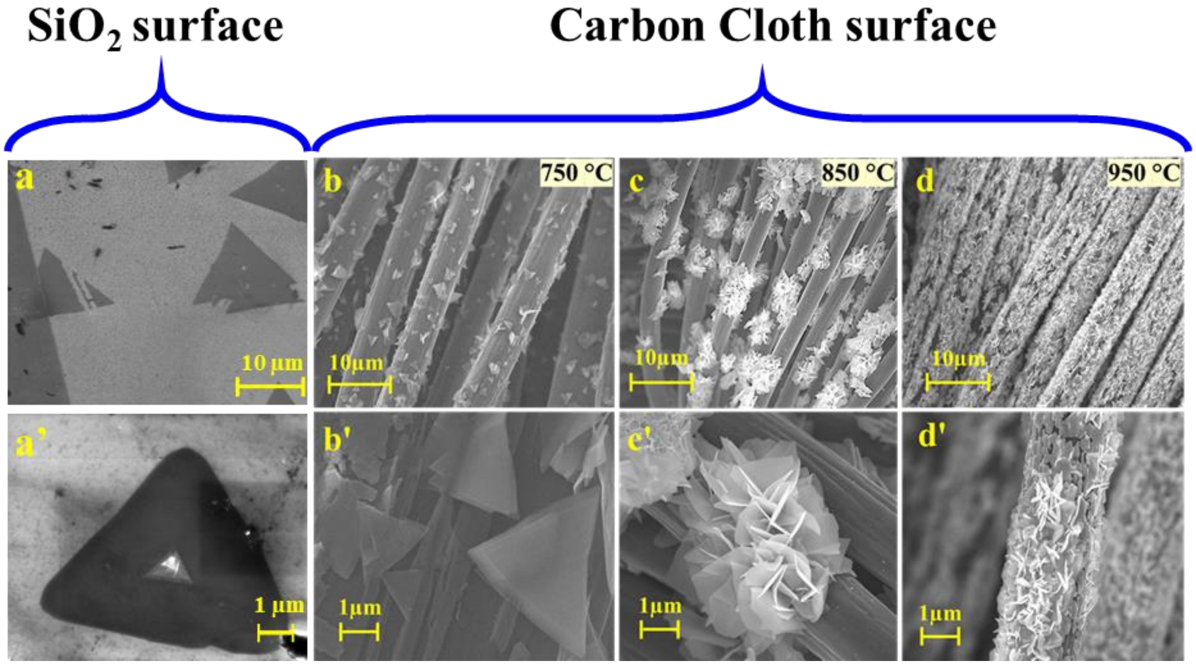

Figure 3.6: Growth and Morphological characterization on different substrate: (a-a’) low and high magnification of triangle on SiO_2 substrate (b-d) low and (b’-d’) high magnification SEM images of $MoSe_2$ morphology grown at (b, b’) 760 °C (c, c’) 850 °C (d, d’) 950 °C. Scale bars: 10 μm and 1 μm.

help to enhance the growth of TMDs with improved reactivity and efficiency. The mechanism behind the formation of nanoflower morphology can be explained as following, the vertical orientation of MoS_2/$MoSe_2$ nanosheets is due to the 3D nature of the CC surface that restricts the diffusion of selenium vapor to the bottom side and paves the way for nucleation followed by growth in a perpendicular direction by diffusing van der Waals layer [106]. Therefore, the diffusion occurs in the perpendicular direction exhibits the growth of the nanosheets on the YZ plane. Afterward, the vertically aligned discrete nanosheets coalesce to reduce the surface energy and convert into a nanoflower morphology. Figure 3.6 (b-d, low magnification) and 3.6 (b’-d’, high magnification) SEM images demonstrated that the $MoSe_2$ growth density, lateral dimensions, and morphology vary with temperature. Interestingly, it was found that the $MoSe_2$ nanosheets patterned into nanoflower morphology and distributed evenly at 850 °C, whereas incomplete growth and excessive coverage of nanosheets were observed at 760 ºC and 950 ºC, respectively. These experiments illustrates that the structure of the catalyst surface is essential to achieve appropriate morphology for particular applications.

3.3 Characterization of monolayer TMDs

Since it was already reported that the controlling the chemical composition in the reaction leads to the transition of the crystal shape from hexagon to the inverted triangle as well as other properties in the embedded systems [117]. To achieve the preferential edge orientation to dominate electronic transport activity, compositions of elements (Mo and S) are very critical because it elucidates the shape, edge, and magnetism of monolayer MoS_2 [118]. This investigation is explained the comprehensive experimental observations about the morphology of TMDs monolayer is a function of the chemical potential of Mo-rich or Se-rich. Based on density functional theory (DFT) and experiments in previous reports, it was found that the equivalent number of both elements in flake makes it suitable for electronic device and sensing application [119, 120]. Therefore, the TMDs was characterized by SEM and energy-dispersive X-ray spectroscopy (EDAX) mapping, Transmission electron microscopy (TEM), Raman, X-ray diffraction (XRD), and Atomic force microscopy (AFM).

3.3.1 Scanning Electron Microscopy and energy dispersive X-ray spectroscopy

SEM images have shown the flakes are triangular and high in density, which determined the concentration of both materials Mo and S/Se are in the same proportion as displayed in Figure 3.7 (a). This makes CVD grown crystal with optimized parameters has excellent electronic properties, which lead towards the better transduction mechanism in the FET device. Interestingly, TMDs nanosheets turn into the atomic layer and triangular morphology at 760º C. To confirm the distribution of the composition, we have performed EDAX mapping, which demonstrates that distribution of Mo and S are homogeneously distributed on atomic layer on SiO_2 as shown in Figure 3.7 (b) and (c). The even distribution of the composition possesses better tunneling effect of electron and reduce the contact resistance with metal to achieve an ohmic contact. We have performed SEM and EDAX imaging of the selenide based nanoflowers to show both conducting and the nonconducting surface can provide high crystalline 2D TMDs as shown in Figure 3.7 (d), (e), and (f).

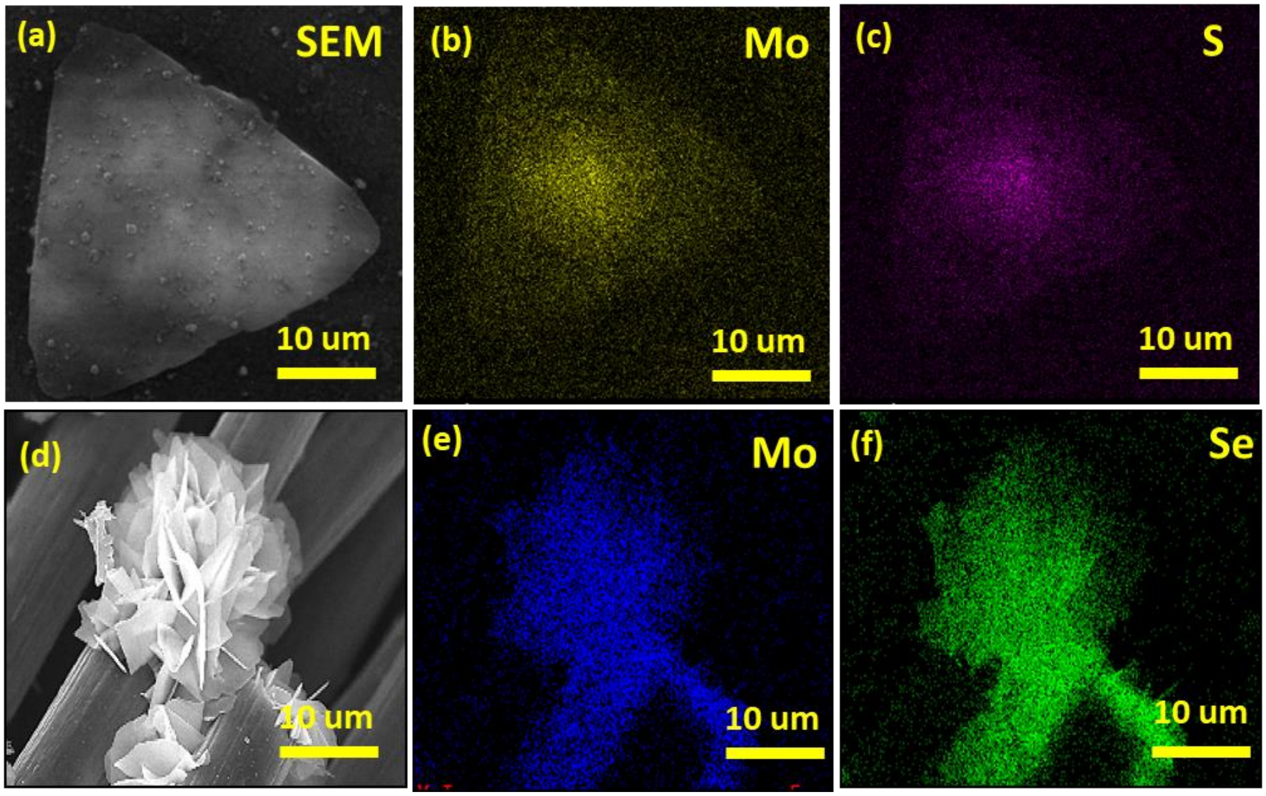

Figure 3.7: (a) SEM image of large MoS_2 on SiO_2 surface (b) and (c) EDAX mapping of MoS_2 triangle with Sulphur and Molybdenum atom distributed evenly. (d) SEM image of $MoSe_2$ nanoflower high magnification (e) and (f) EDAX mapping of $MoSe_2$ nanoflower with Selenium and Molybdenum atom distributed evenly.

3.3.2 Transmission Electron microscopy

A microscopic understanding of the CVD grown TMDs is essential to evaluate the crystallinity and the defects in the film. We have performed TEM and HRTEM on single-layer MoS_2 by transferring on the Copper TEM grid (Transfer method mentioned in section 3.4.2). Figure 3.8 (a) demonstrates the 4k×4k resolution of the TEM image, where aperture size 150 µm at 200 kV. Figure 3.8 (b) represents the low magnification HRTEM image of MoS_2, whereas Figure 3.8 (c) shows the high magnification HRTEM of single-layer MoS_2. This image displays monolayer film consists of negligible defects, which helps the electron tunnel from the film very quickly. Optimized parameters of CVD grown film has a proper arrangement of the atom and possesses high crystallinity with a direct bandgap.

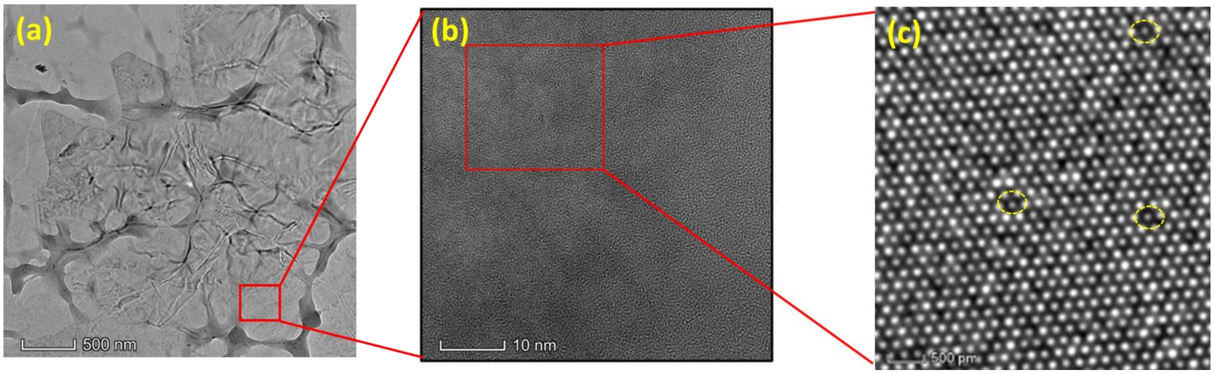

Figure 3.8: (a) Low magnification TEM mage of MoS_2 (b)Optical image of MoS_2 high magnification (c) Optical image of MoS_2 at low magnification (d) (e)&(f) EDAX mapping of MoS2 triangle with Sulphur and Molybdenum atom distributed evenly.

To distinguished the multiple layers atomic arrangement of the monolayer, we have grown the pyramid structure of MoS_2 and performed STEM and EDAX mapping. Figure 3.9 (a), (b) & (c) illustrates the SEM and EDAX mapping of the pyramid structure (stack of MoS_2 nanolayers) grown at the long period of the time. This crystal consists of the improper composition of the elements (Mo and S), which has a single layer on the edges and the number of layers increase when it goes to the center of the flakes. Figure 3.9 (d) represents the STEM mapping of the single

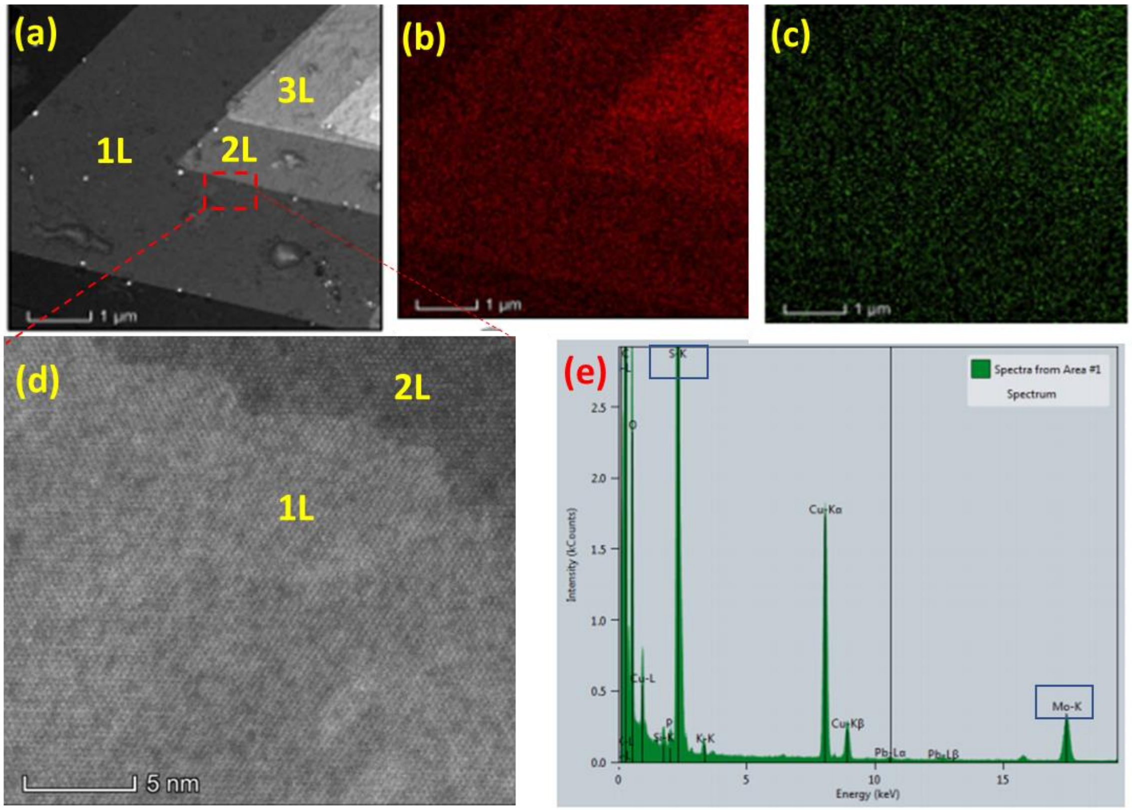

Figure 3.9: (a) SEM image of pyramid MoS_2 (b) and (c) EDAX mapping of pyramid structure of MoS_2 (d) STEM image of the 1L and 2L (e) EDAX spectra of pyramid MoS_2.

layer, and the multiple layers, which approves the atomic arrangement in a single layer (white color) is stable with each Mo consists of 2 S atoms, whereas two layers of the nanosheets have uneven crystal structure and geometry with a high number of defects (more than the single layer). These studies show that the geometry of atoms in a single layer with a lower number of defects consists of better electronics and optical properties with high carrier mobility. The corresponding EDAX elemental mapping exposed the uneven distribution of Mo and S atoms in a pyramid structure, as shown in Figure 3.9 (e). Therefore, a stack of multiple layers is not viable for FET based applications due to the indirect bandgap and uneven structure of the layer increase the mean free path of the electron.

3.3.3 RAMAN Spectroscopy

Raman spectroscopy is another way to investigate the number of layers in the 2D nanoflakes. The crystal structure of the MX_2 (M is the transition metal, and X is the chalcogen) belongs to the D_{3h} point group [107]. At the center of the Brillouin zone (Γ), there are 18 lattice phonon modes present [108]. These dynamical modes are as follows $\Gamma = A_{1g} + 2A_{2u} + B_{1u} + 2B_{2g} + 2E_{1u} + E_{2u} + 2E_{2g} + E_{1g}$. However, in TMDs the the two Raman modes are very active in the atomic layer, E_{1g} mode and A_{1g}, which involves the in-plane and out-plane vibration of the transistion metal and chalcogen [109]. For investigating CVD grown MoS_2 monolayer, as prepared

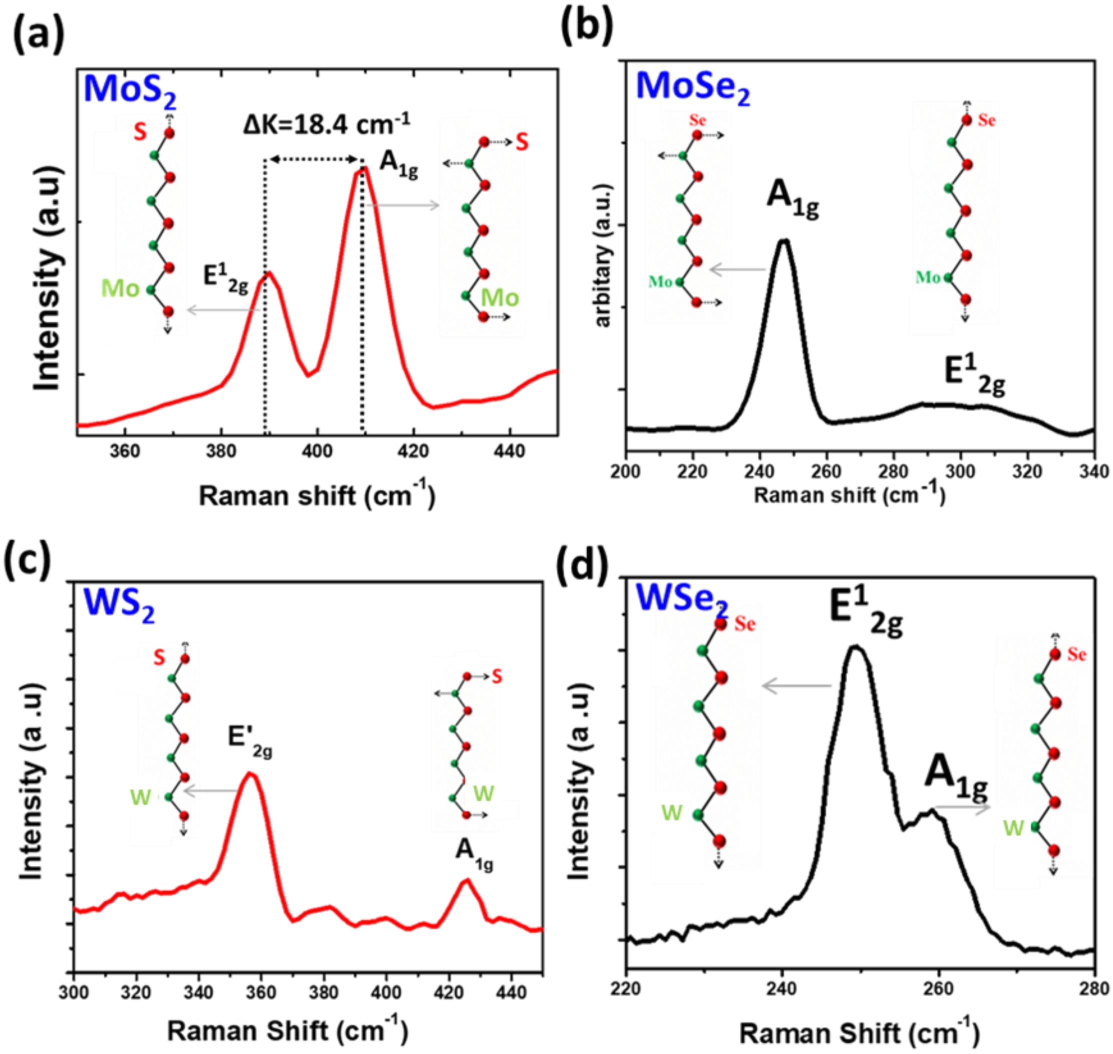

Figure 3.10: Raman characterization of triangular (a) MoS_2 (b) $MoSe_2$ (c) WS_2 (d) WSe_2

MoS_2 triangle are characterized by Raman Spectroscopy using 514 nm laser. This characterization shows the phonon vibration modes of both the in-plane (E2g) and out-of-plane (A_{1g}) of TMDs. As the number of layers reduces, the A_{1g} mode shifts to the lower number called as softening, whereas E^1_{2g} mode shifts to higher number referred to as stiffening [121, 122]. This description is very suitable for illustrating the number of layers in the crystal because monolayer has higher mobility than the bulk one which can easily distinguish in the Raman spectroscopy. Figure 3.10 (a) represents the MoS_2 Raman spectroscopy of the triangular structure. The difference between the two phonon modes represents the 18.4 cm^{-1}, which is the characteristics of the single atomic layer. Similarly, Raman spectra of other TMDs such as WS_2, $MoSe_{2,}$ and WSe_2 were carried out, as shown in Figure 3.10 (b),(c)& (d). The acquired Raman spectrum of $MoSe_2$ characteristics at 760 °C has associated the atomic layer, where A_{1g} mode found at around 241.82 cm^{-1} and E^1_{2g} active mode observed around 287 cm^{-1}. These numbers have confirmed the agreement with recent Raman studies of $MoSe_2$ in terms of the softness of E^1_{2g} peak and stiffness of A_{1g} peak formation of layers $MoSe_2$ nanosheets [98, 110]. For WS_2 CVD grown monolayer the phonon modes found at E_{12g} at 356.3 cm^{-1} and A_{1g} at 417.8 cm^{-1}. Whereas the WSe_2 flakes exhibit one prominent peak E^1_{2g} and other is small shoulder A_{1g} at 250 cm^{-1} and 256.8 cm^{-1} respectively. From these characteristics, we can differentiate the number of the layer in the triangle of sulfide and selenide based TMDs. In sulfide-based TMDs, the phonon peaks difference (A_{1g} and E^1_{2g}) represents the number of the layer, whereas in the selenide based one phonon peaks becomes stiff and other gets broadened illustrates the stacking of the atomic layer [111]. In our case, CVD grown TMDs demonstrate the single layer, which is characteristics of the direct bandgap and high crystallinity.

3.3.4 X-ray diffraction (XRD)

X-ray diffraction (XRD) is one of the essential characteristics for evaluating the crystallography of film and its epitaxial nature. Figure 3.11 (a) represents the XRD of the MoS_2 triangle, which exhibits four peaks at 14.7°, 33.3°, 37.7°, 44.7° corresponds to the (002), (100), (103), and (103) respectively [112]. The characteristics peak of the MoS_2 was detected at 14.7°, which is sharp and exhibits the FWHM 0.53°. Figure 3.11 (b) illustrated the crystal structures of $MoSe_2$, which was systematically investigated by using XRD. At appropriate temperature 760ºC for $MoSe_2$, peak intensities are high, which indicate the high purity of the prepared samples. The XRD diffraction peak around 13.9º from the family of (002) planes, which corresponds to the interlayer distance of $MoSe_2$ layers [51]. This peak positions fit with the (00l) plane of the $MoSe_2$ (JCPDS No. 77-1715) [52, 53]. The obtained peaks in XRD spectra of molybdenum sulfide and selenide are well defined, and absence of MoO_3 (byproducts) fingerprints indicates that as grown MoS_2/$MoSe_2$ are having high purity.

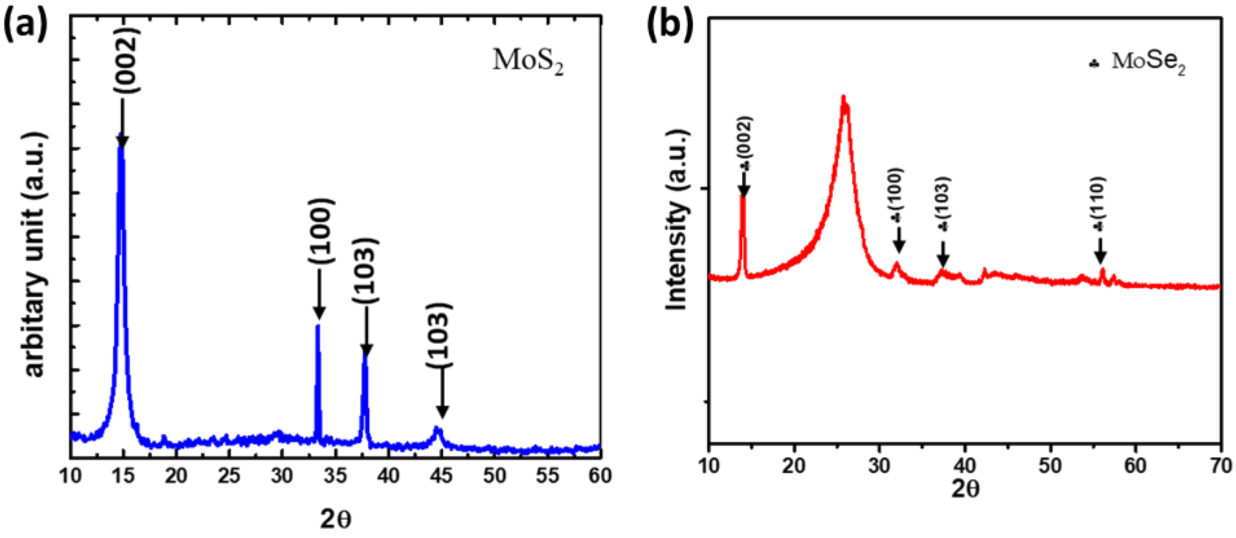

Figure 3.11: X-ray diffraction pattern of of CVD grown triangular flakes where samples displays its characteristic (002) plane peak and their relative intensities at temperature 760°C, which is the signature of the well stacked crystalline structure of (a) MoS_2 and (b) $MoSe_2$

3.3.5 Atomic Force Microscopy (AFM)

To know the thickness of the CVD grown triangular TMDs, we have performed the AFM mapping on triangular shape MoS_2. Contact mode AFM was used to scan the triangle on the surface of SiO_2. Due to the sub-nanometer thickness of the 2D TMDs, we have to customize the cantilever tip for the AFM scanner, which has less distortion due to the thickness and perpendicular to the substrate. After several iterations, we have achieved the mapping of TMDs and measure the thickness of the layer. Figure 3.12 (a) represents the topography of triangular monolayer TMD, whereas Figure (b) shows the single line profile of atomic layer. This characteristic represents that the thickness of the MoS_2 is 0.8 nm, which is satisfied with the previous reports of the monolayer thickness of the MoS_2 [113].

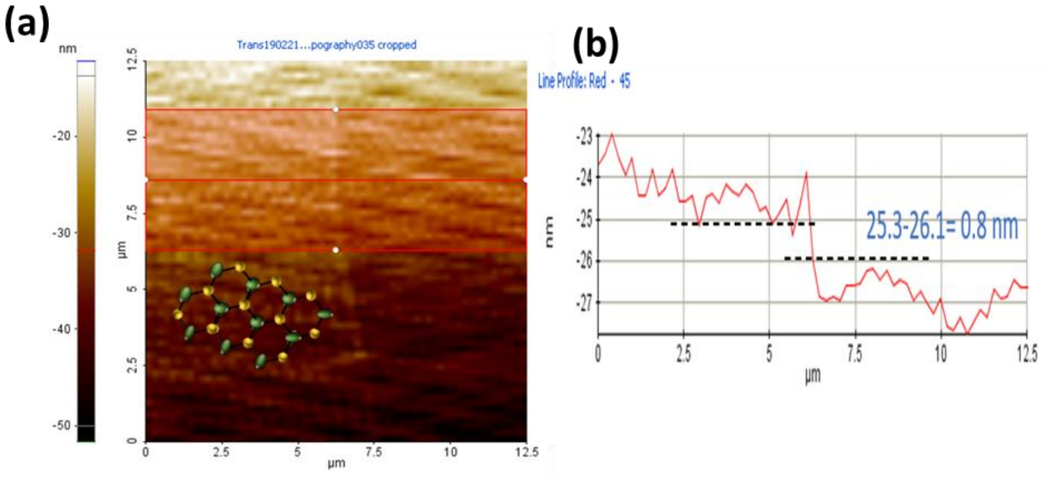

Figure 3.12: (a) AFM mapping of the triangular MoS_2(b) Line profile of the triangular of MoS_2

3.4 Electrical characterization of CVD grown TMDs

3.4.1 Fabrication of 2D FET

After characterization and confirming the crystallinity and the thickness of the monolayer TMDs, we have fabricated the FET devices to measure the voltage current response of the device. To achieve the FET device, we have fabricated two gold electrodes by using optical lithography. The electrodes patterned on the 4 inch of Si/SiO_2 wafer. At first, the wafer was cleaned using

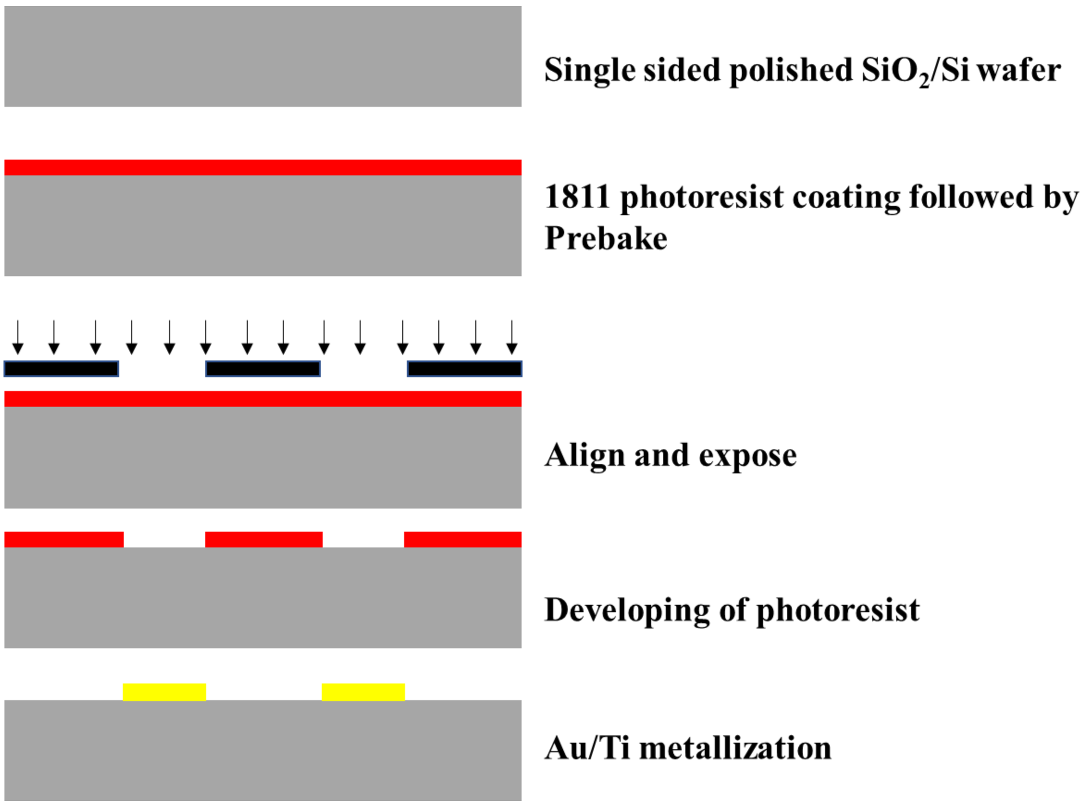

Figure 3.13: Process flow to achieve 2 µm IDE by using optical lithography

piranha solution, which removes all inorganic and organic contamination from the surface. Next, positive photoresist was coated at 3000 rpm for 1 min, followed by prebake for 2 mins at 120°C on a hot plate. After prebaking, the wafer was processed for mask alignment and expose at 35 mJ/cm^2 energy. Later, wafer was developed to achieve Interdigited electrodes (IDE) patterned. A thin Titanium (15 nm) and Gold (70 nm) was deposited through electron beam evaporator onto a substrate. The photoresist layer was then stripped out using acetone in an ultrasonic bath. The process of fabrication of electrodes as shown in Figure 3.13.

After achieving the electrodes, it is essential to transfer monolayers TMDs from growth substrate (catalyst) to the arbitrary substrate (gold electrodes). CVD grown TMDs transfer on the patterned substrate by using the etch transfer method. In this technique PMMA (Poly(methyl methacrylate)) as a sacrificial is used, where it coat on the growth surface as shown in Figure 3.14

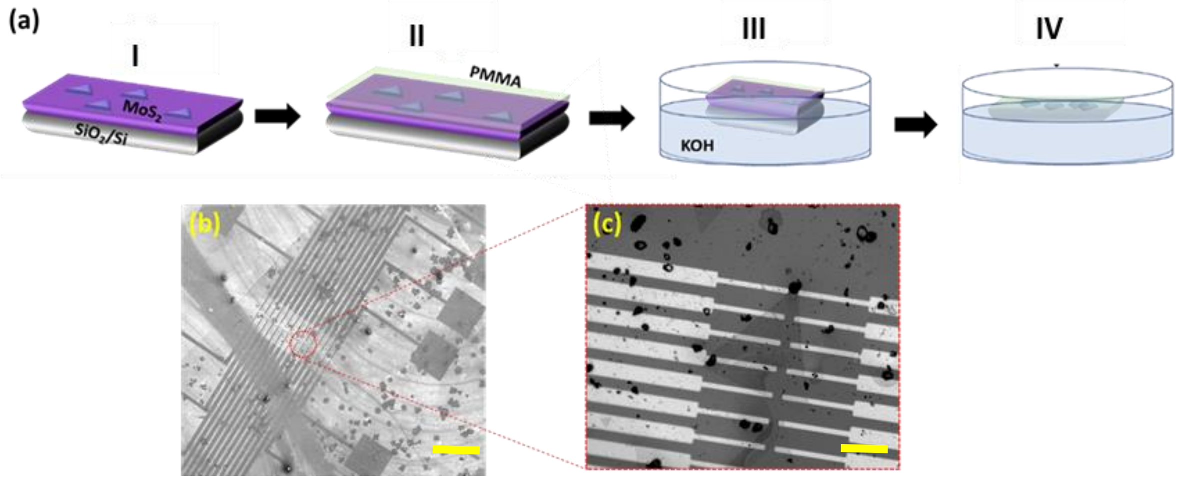

Figure 3.14: (a) Process flow for wet transferring of MoS_2 triangle (I) MoS2 triangles on the substrate (II) Coating of the PMMA as a sacrificial layer (III) Etching of the SiO_2 in the KOH solution (IV) RCA cleaning of the fragile MoS_2 flake to remove inorganic and organic contamination (b) Low magnification, SEM image of the IDE electrodes (scale bar 100 µm) (c) High magnification of IDE electrode with MoS_2 traingular flake (scale bar 10 µm).

(a) step I. The PMMA coating parameter are 3000 rpm for 45 seconds and then postbake at 120 °C on the hot plate for 1 min. The PMMA deposited substrate dice properly into 5×5 mm^2 and place in the KOH solution as shown in Figure 3.14 (a) step II. SiO_2 present undereneath of the TMDs monolayer starts etching in KOH solution at 50°C in DI water. SiO_2 completely etch out in 1 hr by leaving floating fragile layer (PMMA and monolayers) on the water surface as shown in Figure 3.14 (a) step III. Then the arbitrary substrate (glass slide) is used to transfer monolayer from KOH solution to DI water and keep it for 2 Hrs. After removing all the residues of KOH from the fragile layer, we performed the RCA cleaning i.e. remove all inorganic and organic contamination from the TMDs as shown in Figure 3.14 (a) step IV. After cleaning, carefully TMDs have transferred on the fabricated IDE electrodes as shown in the Figure 3.14 (b) & 3.14 Figure (c).

3.4.2 FET characterization of MoS_2 and WSe_2

In the FET characterization, it is found that MoS_2 creates an n-type of the channel due to the presence of Sulphur vacancies and fermi layer present near to the conduction band. The intrinsic majority carrier in the MoS_2 is the electron with the bandgap of 1.8 eV, which is direct in the monolayer and indirect in the bulk form. The fabrication of back gate MoS_2 FET is discussed in the previous section 3.4.1 and 3.4.2, where we have used 300 µm highly p-doped Si wafer. Ti/Au metal was used as metal contact as a source and drain, and the gate voltage is applied from the backside of the Si as shown in schematic Figure 3.15 (a). Figure 3.15 (b) represents the SEM image of the transferred triangle on the IDE electrodes, where the spacing between source and drain are 2 µm. From this, it is clear that the MoS_2 channel is interacting with the supporting

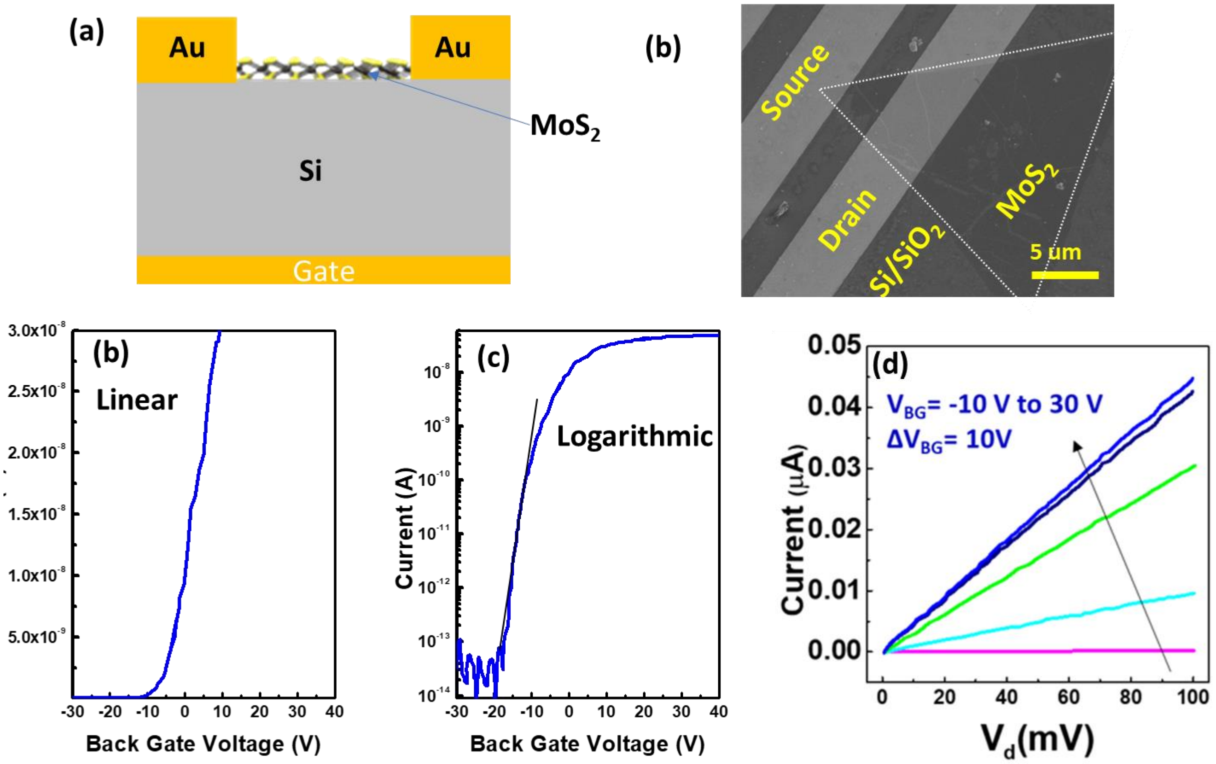

Figure 3.15: (a) Schematic of the back gate 2D MoS_2 (b) SEM image of the MoS_2 triangle transfer on electrodes, which are separated by 4 µm. (c) I_D-V_{BG} linear transfer curve where gate potential is applied from the back side of the highly doped wafer (d) Logarithmic I_D-V_{BG} transfer curve of MoS_2 where SS is 1.5 V/dec (d) I_D-V_{DS} characteristics to check the ohmic contact.

substrate between the electrodes. Afterward, electrical characterization was carried out at the room temperature by using the Keysight B2912A source meter. Here, we have first illustrated current-voltage (I_D-V_{BG}) transfer curve by sweeping back gate voltage (V_{BG}) from -30V to 20V, where biased voltage (V_{DS}) is 100mV as shown in Figure 3.15 (c). The back gate MoS_2 FET ON/OFF ratio found to be 10^6 with an on-state current 10^{-7} and off-state current is 10^{-13}. The threshold voltage (V_T) of the FET to turn on the device illustrated -9V at room temperature. Whereas subthreshold swing (SS) exhibits 1.5 V/dec. SS is an essential factor in the FETs, which is defined as a change in the current with respective dielectric surface potential, as shown in equation 3.6.

$$SS = \frac{dV_{gate}}{d\log_{10} I_{drain}} \dots\dots\dots\dots\dots (3.6)$$

Where dV_{gate} and I_{drain} are a change in gate potential and drain current respectively. The mobility of the FET sensor is calculated by equation 3.7.

$$\mu_n = \frac{L}{CW}.\frac{\Delta I_{DS}}{\Delta V_{GS}}.\frac{1}{V_{DS}} \dots\dots\dots\dots\dots (3.7)$$

Where,L and W are the channel length and the width, ΔI_{DS} is the change in current from source to drain at achange in the surface gate potential ΔV_{GS}, V_{DS} is the drain to source voltage (bias voltage), and C is defines as the capacitaqnce of the insulator. C in the back gate FET derive from the equation

$$C = \frac{\varepsilon_{0x}}{t_{ox}} = \frac{\varepsilon_{r.ox}\varepsilon_o}{t_{ox}}$$

Where, t_{ox} is the thickness of the oxide, ε_{0x} is the relative permittivity of the oxide, which is further define as the relative permittivity of the SiO_2 and permittivity of the vacuum (8.854187817 × 10^{12} F/m). In our case at 300 nm of SiO_2 layer, the resulting capacitance of the dielectric layer to the semiconductor was calculated 11.45 nF. The mobility of the back gate field voltage is found to be 0.12 cm^2/V.s at room temperature from I_{DS}-V_{BG} transfer curve. Figure 3.15 (d) illustrate the I_{DS}-V_{DS} back gate characteristics, which represent the 2D material achieved ohmic contact with metal electrodes.

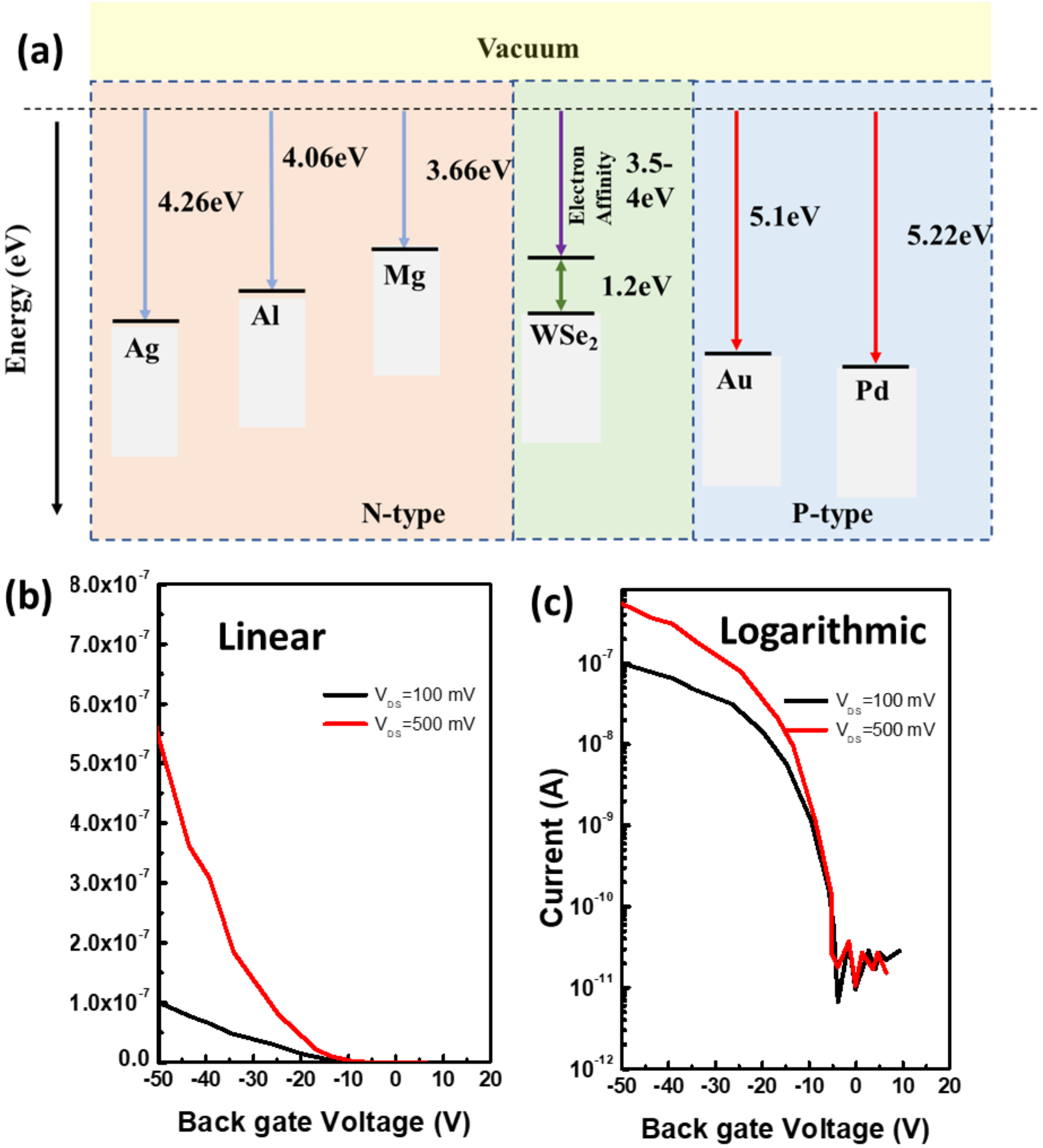

Figure 3.16: (a) Band aligment of source/drain metal for p-type and n-type with the triangular WSe_2 (b) I_D-V_{BG} linear transfer curve of channel WSe_2 where gate potential is applied from the back side of the highly doped wafer at voltage 100 mV and 500 mV (c) Logarithmic scale of WSe_2

Similarly, we have demonstrated p-type of semiconductor by using CVD grown WSe_2 monolayer. 2D WSe_2 is ambipolar in nature where it creates p-type or n-type behavior with different metals depending on the work function [25−34]. There have a few reports where researchers have used this dual behavior to make complementary gate circuits [26,27]. In the schematic shown in Figure 3.16 (a), WSe_2 possesses p-type functionality when gold is employed as a source and the drain, whereas other metal such as Al and Ti creates the n-type FET transistor. Therefore, the polarity of electrons and hole injected at the source metal contact determine which the type of FET to be formed [114]. Work function differences and Schottky height barrier play a significant role with the polarity and injection efficiency of the carriers. Hence the selection of contact metal with larger work functions is crucial for having control over the Schottky barrier heights [115]. Therefore, in our case, to achieve the p-type FET, we have transferred WSe_2 on the gold electrode and performed I_{DS}-V_{BG} on two different bias voltages 100 mV and 500 mV. Figure 3.16 (b) & (c) demonstrate the linear and logarithmic constant bias, where the gate voltage is sweep from 0 to -50 V from the back gate of 300 nm SiO_2. In this case, the threshold voltage is illustrated from the I_{DS}-V_{DS} transfer curve -15V to turn ON the device, and the mobility is found to be 0.021 $cm^2/V.s$ at 100mV bias.

3.5 Summary and conclusion

In summary, we have grown semiconducting monolayer and few-layers TMDs by the CVD technique. The challenges involved to achieve high crystalline monolayer TMDs in CVD are solved by optimizing the flow rate of Sulphur, amount of TMO, pressure, temperature, and growth time. The optimization of these parameters is vital to achieving the high crystalline TMDs on SiO_2/Si wafer. TMDs growth has been performed on different catalyst substrate to illustrate the morphology and the structure. It was found that the SiO_2 substrate helped to attain pristine triangular monolayer growth, whereas the other 3D structure of CC employed the vertical growth of the TMDs. Afterward, the composition of Mo and S elements elucidate to understand the shape, edge and magnetism of 2D TMDs [116]. Therefore, the TMDs were characterized by optical microscope, SEM, Transmission electron microscopy (TEM), Raman, X-ray diffraction (XRD), and Atomic Force Microscopy (AFM). Particularly, optical, SEM, and EDAX mapping has shown the flakes are triangular, which determined the concentration of both materials Mo and S are in same proportion. This makes CVD grown crystal has better electronic properties, which lead towards the better transduction mechanism. Sulfide and Selenide based TMDs are characterized by Raman Spectroscopy using 514 nm laser as illustrated, which represents the presence of the phonon vibration modes of both the in-plane (E_{2g}) and out-of-plane (A_{1g}) of TMDs. These two modes can be helpful to differentiate the number of layers in the crystal. X-ray diffraction (XRD) of MoS_2 was performed for evaluating the crystallography of film and epitaxial nature. XRD also confirms there is no immature residue in the supporting substrate such as Molybdenum oxy-sulphide (MoOxS) and metallic MoO_2. TEM characterization has been acheived to study the molecular structure of flakes which is very important to understand the crystallinity of the material. AFM mapping is carried out on the single MoS_2 layer to elucidate the thickness, which is found to be 0.8 nm. These characterizations demonstrated that the CVD grown TMDs are crystalline without defects and proper in composition, which attain better mobility by reducing the mean free path of the electron during FET characterization.

MoS_2 and WSe_2 FET devices were fabricated to evaluate the electrical characterization of TMDs by using photolithography and wet transferring techniques. The overall FET device behavior was explained by the mobility of electron and holes through these 2D materials. The Back gate voltage is given from 300 nm of SiO_2/Si wafer to evaluate the electronic mobility and the SS of the crystal from transfer curve I_{DS}-V_{BG}. CVD grown MoS_2 shown ohmic contacts with the metal electrodes by achieving mobility of 0.12 cm^2/Vs. Whereas CVD grown WSe_2 is ambipolar in nature, which illustrates both p-type and n-type depending upon the source to drain metal electrodes. In our case, we have transferred WSe_2 on the gold electrodes and fabricated p-type of the FET, where the holes are the majority carrier and mobility were demonstrated 0.021 $cm^2/V.s$.

At present, we have grown different monolayer materials such as MoS_2, WS_2, $MoSe_2$ and WSe_2 on the various catalytic substrate, as shown in Table 3.1. However, from these materials, MoS_2 and WS_2 were found more appropriate for the building the biosensor because of the biocompatibility and hydrophobicity [115]. The wettability and the biocompatibility are essential parameters for fabricating biosensors because biocompatible material is inactive in the reaction of biomolecules and hydrophobicity use to direct attachment of the linkers and antibodies. Due to these advantages of Sulphide based materials in the biosensor, we have chosen the MoS_2 from CVD grown materials library as a 2D semiconducting material for FET based biosensor.

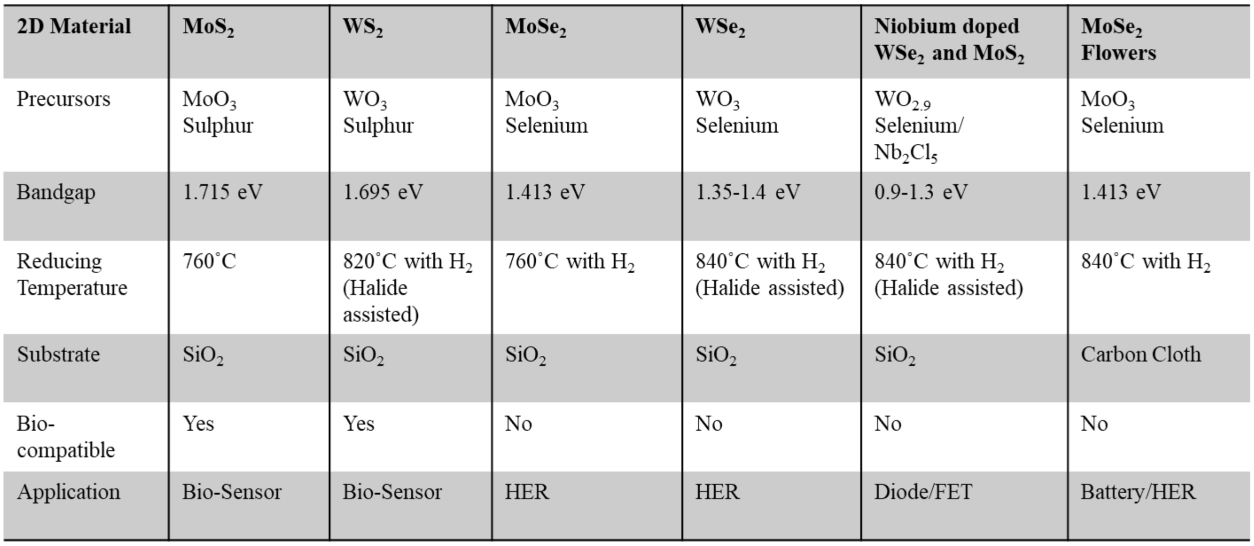

2D Material	**MoS_2**	**WS_2**	**$MoSe_2$**	**WSe_2**	**Niobium doped WSe_2 and MoS_2**	**$MoSe_2$ Flowers**
Precursors	MoO_3 Sulphur	WO_3 Sulphur	MoO_3 Selenium	WO_3 Selenium	$WO_{2.9}$ Selenium/ Nb_2Cl_5	MoO_3 Selenium
Bandgap	1.715 eV	1.695 eV	1.413 eV	1.35-1.4 eV	0.9-1.3 eV	1.413 eV
Reducing Temperature	760°C	820°C with H_2 (Halide assisted)	760°C with H_2	840°C with H_2 (Halide assisted)	840°C with H_2 (Halide assisted)	840°C with H_2
Substrate	SiO_2	SiO_2	SiO_2	SiO_2	SiO_2	Carbon Cloth
Bio-compatible	Yes	Yes	No	No	No	No
Application	Bio-Sensor	Bio-Sensor	HER	HER	Diode/FET	Battery/HER

Table 3.1: Different 2D TMDs material grown in the CVD

CHAPTER 4 SUSPENDED 2D MATERIALS FET

4.1 Introduction

Designing the energy-efficient and steep transistor integrated circuits is the key to enhance the global Information and sensing industries. However, 3D materials such as silicon are the traditional material used in the FET transistors, which requires high power and trying to scale down under 10 nm channel length. This is because when the silicon channel length is reduced, the leakage current becomes high even though the transistor in the off state, which loss the electrostatic control from the gate. Moreover, in the 3D structure of the silicon, the electron mobility get reduces and the mean free path to travel electron from the channel is more, which impedes to make ultrafast and ultrasensitive FET devices. Therefore, 2D materials can be overcome these problems due to their unusual properties that stem from their quantum and surface effect [117, 118]. Graphene is well-studied material in the field of 2D morphology, and it has some extraordinary properties like super thin, transparent, highly conductive as well as large mechanical strength [118]. However, due to semimetallic in nature, it cannot be implemented in the FET channel. The other 2D materials are transition metal dichalcogenides (TMDs), which holds great potential for many electronic and optoelectronic applications due to heavier carrier effective mass, bandgap is more, in-plane dielectric constant is less which leads to the lower down the tunneling effect [119].

Semiconducting TMDs, such as molybdenum disulfide (MoS_2) and tungsten diselenide (WSe_2) are very well studied materials because of excellent carrier mobility, high ON/OFF ratio and good sub-threshold swing in a field-effect transistor (FET) that pave the way towards ultimately scaled low-power electronics. In the FET, MoS_2 creates an n-type of the channel due to the presence of sulfur vacancies and fermi layer present near to the conduction band whereas WSe_2 consists of intrinsic hole mobility which makes p-type of the channel. These semiconducting 2D

TMDs with both n-type and p-type intrinsic mobility and thin-film pristine structure (MoS_2-0.65 nm and WSe_2-0.7nm) are a suitable candidate for low power consumption FET devices for future integrated circuits and bioelectronics.

4.2 Challenges involve in 2D FETs

Using these 2D materials, researchers have demonstrated optical and electronic devices by tuning its bandgap, surface energy and strain control. Despite direct bandgap and high mobility like silicon, the performance and reliability of such atomic layered crystal are easily affected by the supporting substrate interaction, as shown in Figure 4.1 (a). 2D materials are fragile in nature and it is impossible to make devices without any supporting substrate. However, the interaction between supporting substrate and WSe_2/MoS_2 leads to the reduction of the carrier mobility and the increase the subthreshold swing [120]. The mechanism of charge scattering drastically changes from substrate morphology by inducing local corrugation and strain, charge impurities, and surface phonos. In specific, Si/SiO_2 substrate impede the mobility of electron by trapping of charges, which imply that interface control is vital for the performance of devices made up by atomic layers as illustrated in Figure 4.1 (b). Secondly, the atomic layer on the top of the supporting substrate

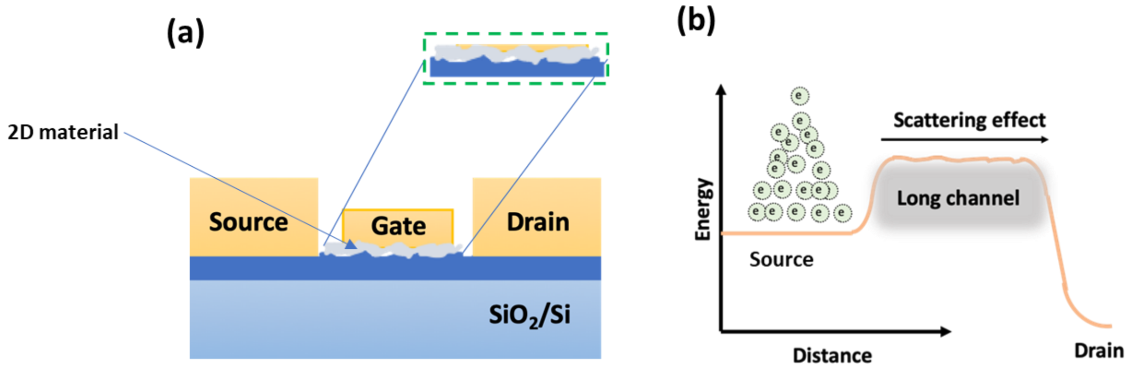

Figure 4.1: (a) Schematic of the 2D top gate FET with the scattering phenomenon from the supporting substrate (b) schematic of tunneling of the electron from source to drain with scattering effect.

cannot contribute clearly mean free path of the electron in 2D materials, which produce unreliability in every single device.

4.3 Suspended 2D FET via nanogaps

Our approach to achieve freestanding 2D materials are creating the nanogap electrode by using a self-assembly photolithography technique. Nano-spacing between the thick electrode does not allow the atomic membrane (0.65 nm) to touch the supporting substrate and it is present flat on the two electrodes and eliminates the interaction of the supporting substrate. This structure not only eliminates supporting substrate effect but also reduce the channel length and shows the feasibility for further miniaturization of the device. Due to the eradication of the supporting substrate, the mobility of the electron/holes is enhanced, which is derived as follows

$$\mu_n = \frac{L}{CW}.\frac{\Delta I_{DS}}{\Delta V_{GS}}.\frac{1}{V_{DS}} \ldots\ldots\ldots (\mathit{Suspended\ and\ Supported\ FET\ mobility}) \ldots\ldots 4.1$$

Where L and W are the channel length and the width, ΔI_{DS} is the change in current from source to drain at a change in the surface gate potential ΔV_{GS}, V_{DS} is the drain to source voltage (bias voltage), and C is defined as the capacitance of the insulator. In the above equation ΔI_{DS} depends upon the gate potential (inversion charges, Q_{inv}) and the transit time (t_r) as shown in equation 4.2.

$$I_{DS} = \frac{Q_{inv}}{t_r}.WL \ldots\ldots\ldots\ldots (4.2)$$

However, the freestanding nature of 2D material, electron/holes can tunnel very smoothly without any scattering from supporting substrate and reduce the time of transit from source to drain. This increase the I_{DS} which is directly proportional to the mobility of the FET device. Secondly, the reduction of channel length further reduces the transit time and lower down the subthreshold swing

(SS). SS is defined as the steepness in I_{DS}-V_G transfer curve i.e. the time requires to turn ON the FET device, which is defined as shown in equation 4.3.

$$SS = \frac{dV_G}{d\log_{10} I_{DS}} \ldots \ldots \ldots \ldots \ldots (4.3)$$

Therefore, freestanding 2D materials on the nanogaps open up the new avenues in the field of FET based integrated circuit and ultrafast sensing domain.

4.4 Fabrication of the nanogaps

There have been different techniques reported to achieve nano-gap spacing in-between two electrodes such as electron beam lithography and scanning probe microscopy [121-123]. Although, these techniques for creating nanogaps between two electrodes are suitable for prototyping, but it is impractical for mass production. Therefore, in this section, we are demonstrating suspended 2D material devices fabricated by a self-assembly lithography technique to create single or arrays of nanogap electrodes for wafer-scale fabrication.

Nanogap electrodes have fabricated by self-aligned photo-lithography technique, which consists of thermally grown 300 nm oxide layer on 330 µm double-sided Silicon wafer. The wafer is cleaned via RCA and dried it out in the dryer. By using lift-off method, the first electrode layer is patterned by metallization through electron beam evaporation of 10 nm of Titanium, 80 nm of Gold and 100 nm of Chromium (Cr) layers as shown in Figure 4.2 steps (I) to (VI). In the first electrode, the Cr thickness is more than the gold electrode because Cr acts as a sacrificial layer. After step (VI), wafer kept at ambient temperature for overnight results in an oxide layer Cr_xO_y form which overhangs few nanometers to 10x nm depends upon the temperature (40ºC to 120ºC) on the edges of Ti/Au. Following step (VI), a similar method has been used to deposit the second electrode of Ti/ Au, as shown in Figure 4.2 steps (VII) to (IX). While depositing the second electrode, enlargement of Cr_xO_y in few nanometers protect second electrode (Ti/Au) to meet the

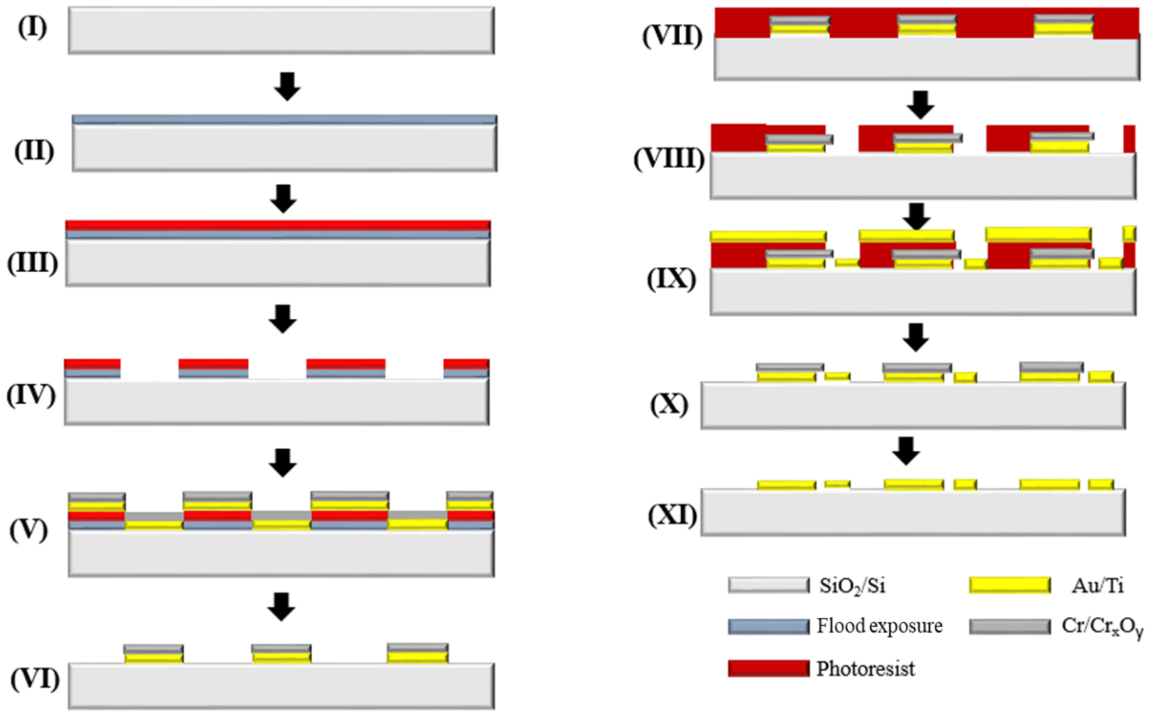

Figure 4.2: (I) Si/SiO$_2$ wafer (II) flood exposure of 1811 (III) Photoresist 1811 coating in spinner at 3000 rpm (IV) Exposing and developing 1811 (V) Depositing metal Cr/Au/Ti (VI) Lift-off 1811 (VII) Coating 1811 for second electrode (VIII) Developing 1811 photoresist (IX) Second electrode metallization Au/Ti (X) Stripping of 1811 and LOR (XI) Two Au/Ti electrodes separated by nanogap

first electrode and creates nanometer spacing. In steps (X) photoresist strips by using acetone whereas in step (XI) chromium/chromium oxide layer etch in chromium etchant solution and two Ti/Au electrodes which are separated by nanogap retain on Si/SiO2 wafer.

Here, few parameters were optimized while fabrication such as lift-off resists thickness, rpm rate of spinning photoresist, baking, developing photoresist, avoiding the residues during fabrication and most important optimization thickness of metal electrode layer. Initially, a lift of resist (LOR) considered for the lift-off method. However, a photoresist peeled out the chromium layer while doing lift off, as shown in Figure 4.3 (a). This lift-off happens because of the thick layer of chromium exert more force while etching photoresist in PGMI remover. In the next batch, LOR A has been eliminated, and the self-made recipe was considered, where two layers of Micro-

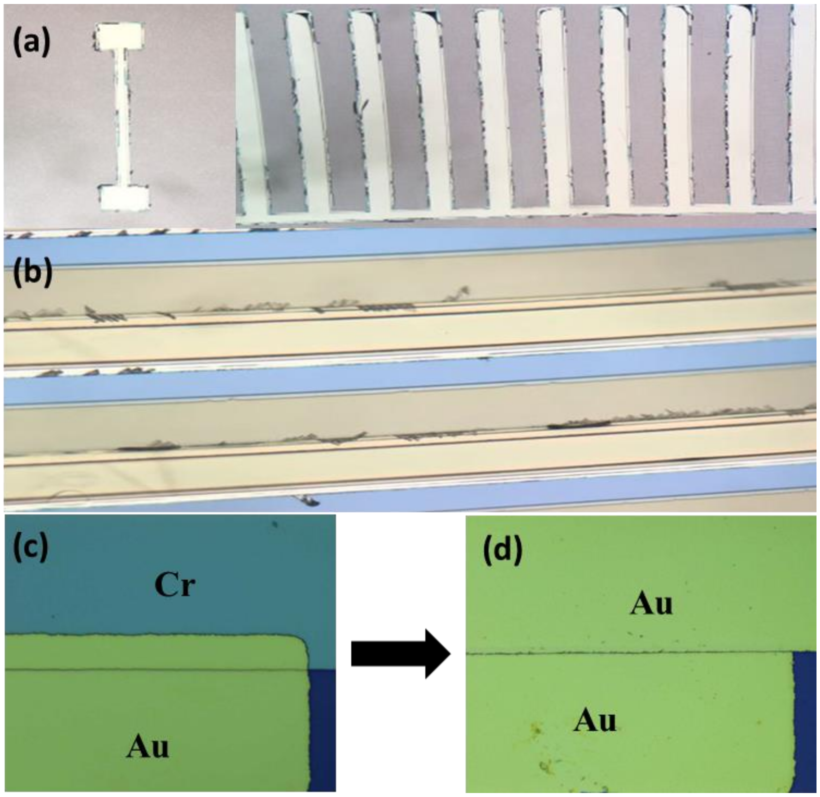

Figure 4.3 (a) LOR A fabrication of Nanogap **(b)** Thin layer of Chromium reluctant to lift off Au (c) second layer gold and chromium (d) lift of the chromium with constant nanogaps.

resist 1811 has patterned and thickness of gold/chromium is reduced. In this new technique, patterning the first electrode was carried out by coating the positive photoresist (MICROPOSIT S1800) and expose it for 80 mJ/cm^2 (flood exposure). Then another layer of photoresist 1811 is coated on the top and pattern it with design chrome mask followed by evaporation of the Ti/Au/Cr. After patterning three metal layers Ti/Au/Cr, wafer kept for a night to thermal expansion of the chromium to achieve nanogap. Nano-spacing between electrodes only depends upon the thermal expansion of the chromium. Therefore, it is essential to maintain the temperature as well as environmental gases of the wafer constant for overnight. Initially, the thin layer of Chromium is reluctant to lift off the second layer of gold, as illustrated in Figure 4.3 (b) due to the Au thickness. Therefore, to achieve the proper pattern of the second layer, the thickness of Ti/Au (second layer) thickness reduce by 50% of chromium. After optimization of the thickness, lift off the chromium as well as second Au electrode was processed in chromium etchant solution, which came out effortlessly. Figure 4.3 (c) illustrates the optical image after depositing the second electrode on the top of chrome, whereas Figure 4.3 (d) represents the optical image of nanogap after etching chrome (sacrificial layer).

Figure 4.4 (a) represents the optical image of the wafer-scale nanogaps, which has a constant spacing throughout the wafer. Figure 4.4 (b) and (c) demonstrate the low magnification and high magnification of the array on the SiO_2/Si substrate. While nanogap fabrication, we have achieved a different range of the nanogaps from 10 nm to 150 nm by varying the temperature and environmental conditions. After confirming the process flow to achieve nanogaps at various temperature and show the feasibility at wafer-scale, the different substrate has been used to check the process flow viability. Given the importance of flexible electronics, we have patterned nanogaps on the flexible PET sheet, as shown in Figure 4.4 (d). Figure 4.4 (e) and (f) shows the high and low magnification of the nanogaps electrode on the flexible PET sheet

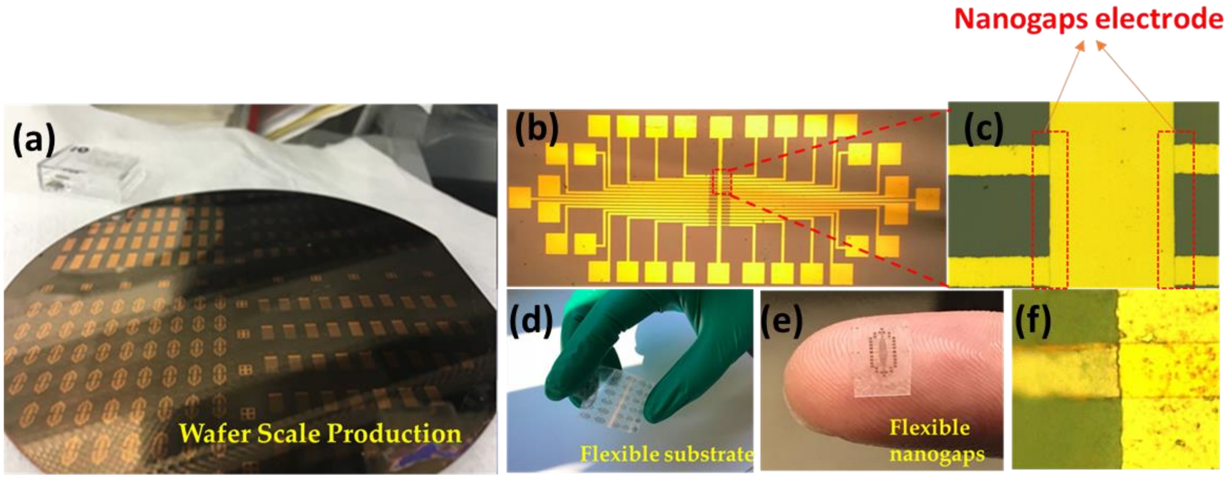

Figure 4.4 : (a) Wafer scale production of the nanogap with different structures (b) Nanogap array device at low magnification (c) high magnification of the nanogap array with proper lift of the chromium (d) Wafer scale flexible substrate (e) low magnification of nanogap array on the flexible device (f) high magnification of the nanogap electrodes on the flexible substrate

4.5 Evaluation of nanogaps

Self-assembly is considered as a superior technique to fabricate the nanogaps electrodes for reliable, reproducible, and wafer-scale fabrication. However, due to the involvement of the whole wafer, it is very challenging to check electrodes that are not touching together using SEM and other imaging methods. Therefore, I-V characterization has considered for evaluating the connection between the two electrodes. As shown in Supplementary Figure 4.5 (a), when the circuit is open, i.e., two electrodes are not touching together, then there is no current flowing. However, when two metals touch together, then the I-V curve is a straight line with a slope, which resemblance of the flow of current, as shown in Figure 4.5 (b). It is a very viable and controlled method to check the nanogap electrodes in the whole wafer.

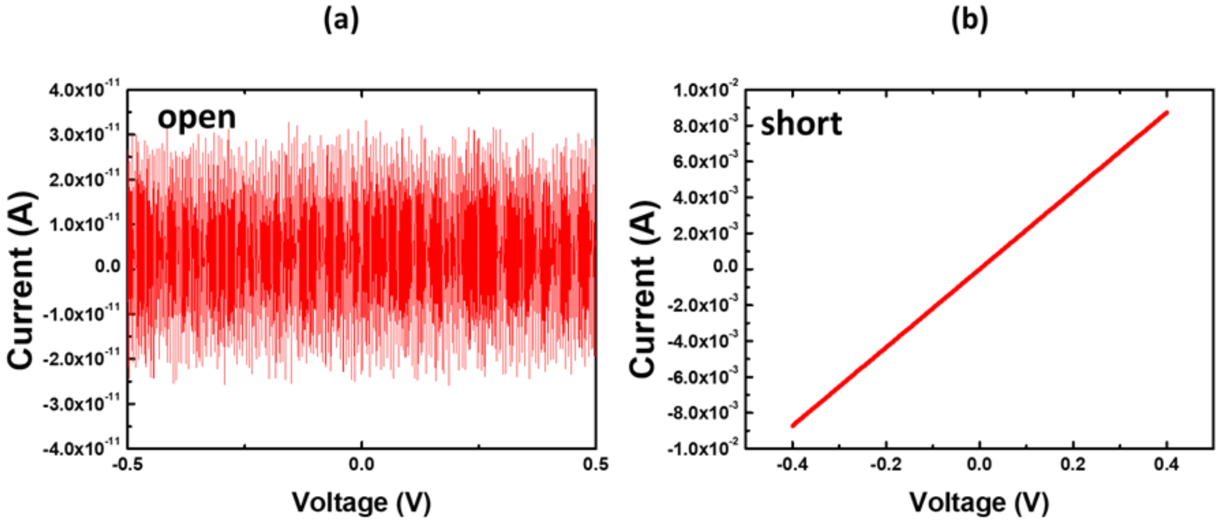

Figure 4.5: Electrical characterization of nanogaps (a) I-V characterization of open circuit (no connection of electrode). Scanning voltage: -0.5 V to 0.5 V. (b) I-V characterization of short circuit (connection of the nanogap). Scanning voltage: -0.4 V to 0.4 V

4.6 Novel dry stamping method

The traditional method for transferring the 2D materials on the arbitrary substrate requires wet chemistry (detail discussion in chapter 3). However, while transferring the 2D materials in nanogaps through the wet transferring method, some of the moisture trap into the nanogap and reduce the overall mobility. Therefore, we have developed novel the dry stamping method of the 2D TMDs (MoS_2) on the nanogaps by using a thin film of PDMS (Polydimethylsiloxane). Initially,

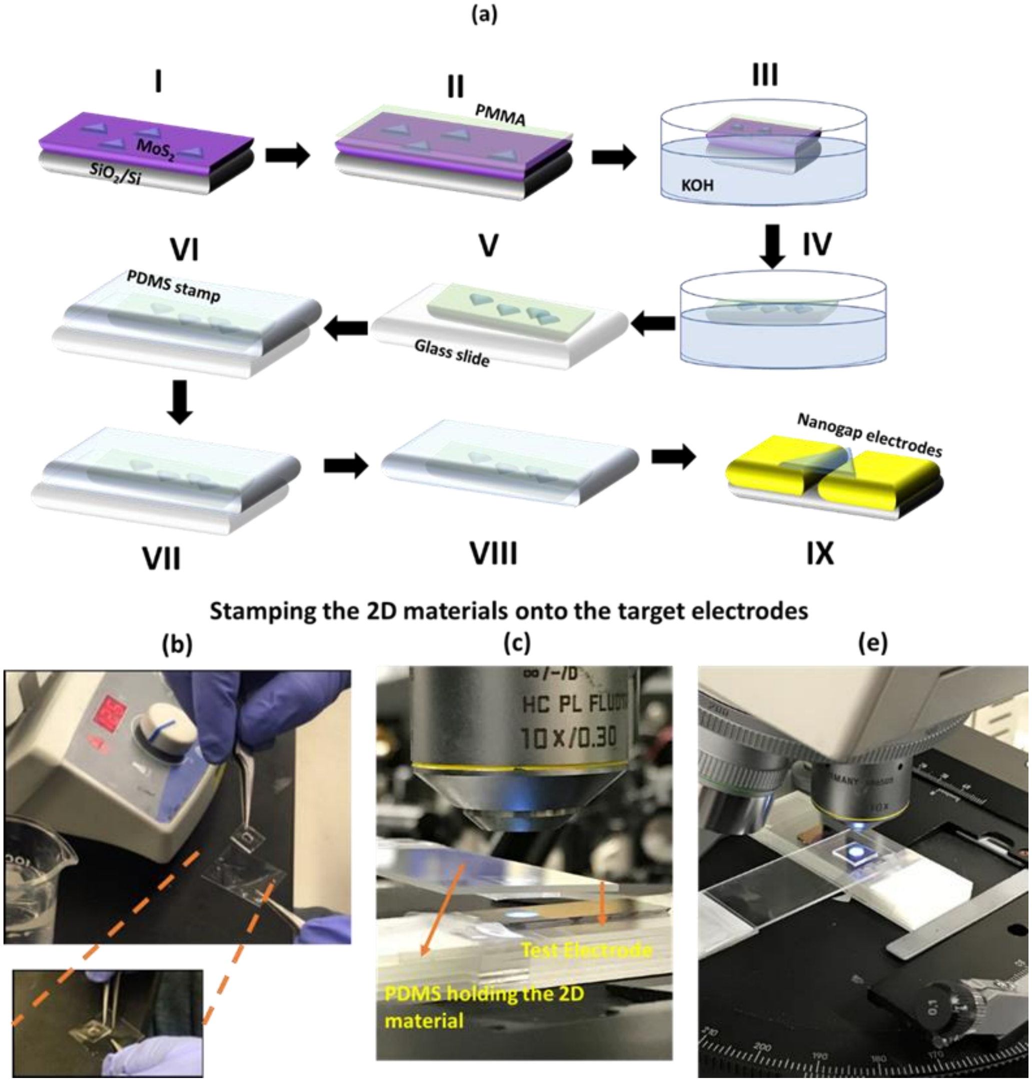

Figure. 4.6: Dry transfer of CVD grown MoS_2 (a) Process flow of dry stamping of MoS_2 on nanogap electrodes (b) Image of the transferring PMMA on the glass slide (c) Image of aligning MoS_2 triangle with nanogaps in the microscope & (d) Lift off the micromanipulator on z-axis at 100°C

MoS_2 has grown on Si/SiO_2 chuck via CVD method, which is controlled technique and provide a uniform thickness of atomic layer triangle as shown Figure 4.6 step I. Once the process is done then PMMA (Poly (methyl methacrylate)) as a sacrificial layer is coated on the synthesized MoS_2 crystals (step Figure 4.6 II). In the step Figure 4.6 III, SiO_2 was etched out in KOH solution, which gives monolayer MoS_2 with PMMA sacrificial layer floating on the solution. Afterward this PMMA layer clean in DI water and transferred from the solution on the glass slide as illustrated in Figure 4.6 step IV and V. However, step I to step V are a traditional method to exfoliate CVD grown atomic layer and transfer on the arbitrary substrate, but it is challenging to transfer the micron level triangles on the desired region [124]. Therefore, to transfer MoS_2 on an appropriate area, dry stamping method has been applied, in which PDMS was considered as a transfer film. PDMS stamp layer of 2-3 mm thick prepared by using commercially available silicone elastomer kit (SYLGARD® 184). Synthesized PDMS stamp placed on the top of the glass slide, where exfoliated PMMA layer easily peel out on the PDMS stamp as shown in Figure 4.6 step VI to VIII. Figure 4.6 (b) represents the exfoliation of the PMMA layer from the glass slide on the PDMS. The PDMS stamp and PMMA have higher surface energy than the glass; therefore, layered crystals are easily peeled out from glass substrate [125]. Afterward, the other side of PDMS were carefully adhered on the glass slide and mounted on the in-house XYZ micromanipulator, as shown in Figure 4.6 (c). Due to the transparent nature of the glass and PDMS, it is easy to locate the triangle as well as nanogap electrodes, which was aligned carefully. Once PDMS stamp properly pressed on the nanogaps, the heater present underneath of the substrate was raised till 100°C for 15 mins. At 100°C to 120°C PMMA adhered on the nanogap electrodes with high surface energy and PDMS wettability changes with temperature and degraded it adhesion with PMMA [126]. Finally, the PDMS stamp moved up (z-axis) at 100 °C as represented in Figure 4.6 (e) and PMMA with atomic crystal left behind on the nanogaps electrode as illustrated in step IX from Figure 4.6 (a).

4.7 Characterization of 2D TMDs on the top of nanogaps

4.7.1 AFM mapping on the suspended 2D materials

After transferring the nanogap on the top of the electrodes, it is important to evaluate the 2D TMDs is suspended on the electrodes. Therefore, we have performed AFM mapping via a custom-built AFM tip (height-14 µm) from the App nano. This tip is a super sharp whose radius

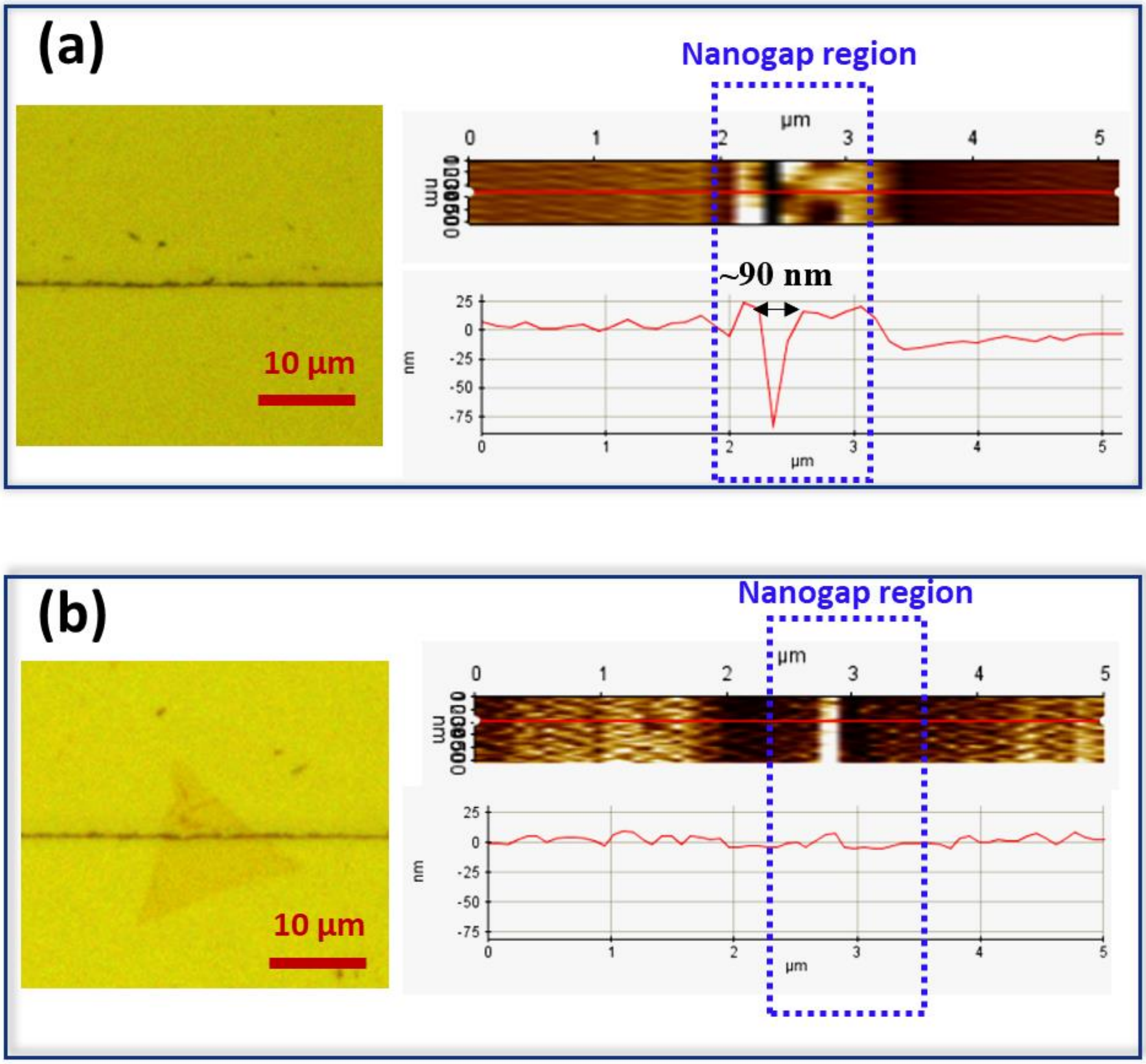

Figure 4.7 : Optical image, AFM mapping, and line diagram of nanogaps (a) without MoS_2 (b) with MoS_2.

is less than 3 nm and can be useful for high-resolution mapping i.e. the minimum lateral feature size it can detect 0.5 nm. After several iterations, we have successfully able to achieve proper line diagram and imaging from the AFM. Figure 4.7 (a) shows the optical image and AFM mapping with the line profile of the nanogap area without MoS_2 flake. AFM line profile of nanogap electrodes demonstrates the step height of 75 nm in between the two Au electrodes, which confirms the two metal layers are separated by nanometer spacing. Figure 4.7 (b) represents the optical image and AFM mapping of transferred MoS_2. AFM line profile of transferred MoS_2 on the top of nanogap indicates the flat line and no step height, which verify that the atomic membrane is suspended and remarkably stiff as well as robust. This stiffness of the atomic layer confirms that it is not interacted with supporting substrates and eliminates the scattering phenomena of the interface between the 2D material and the holder substrate. This mechanical strength provided by nano spacing does not allow the monolayer sags between the electrodes, which permits depositing another layer, i.e. HfO_2 and for sensing application, it facilitates the attachment of biological receptor for selective sensing.

4.7.2 SEM and Dark field imaging of the suspended 2D material

To further validate the rigid suspension of the MoS_2 monolayer, scanning electron microscope (SEM) and dark field image of the MoS_2 triangle on the top of the nanogaps were performed. Figure 4.8 (a) shows the SEM top view image of the fabricated suspended device, where MoS_2 is present as a flat membrane on the top of two Ti/Au electrodes. Whereas, Figure 4.8 (b) represents the dark field image of the MoS_2 triangle on the top of the nanogaps; this image clearly illustrates that the MoS_2 triangle does not sag in between the nanogap spacing, it is suspended and flat on the surface. From this imaging, it is clearly illustrated that the MoS_2 triangle sturdy in between the nanogap spacing, it is suspended and flat on the top of two Au electrodes.

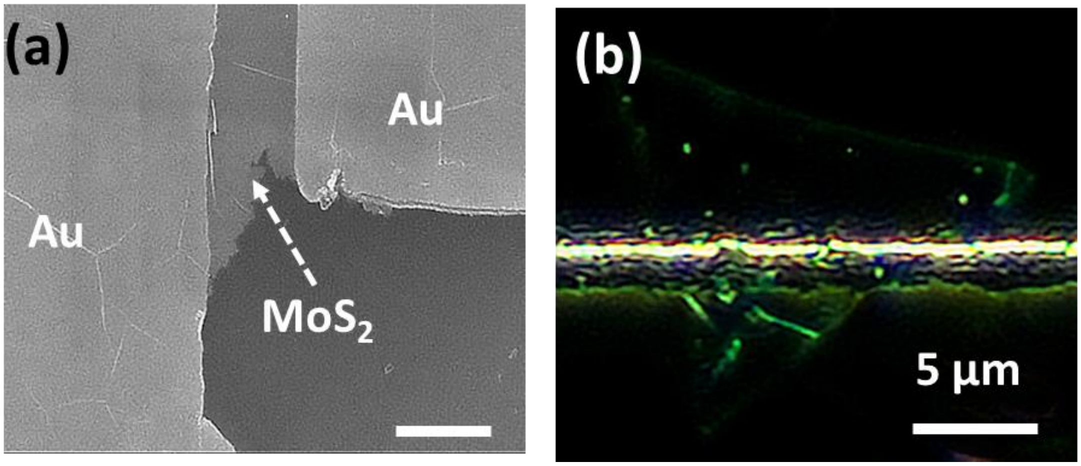

Figure 4.8: (a) high magnification SEM image of MoS_2 on the top of nanogaps (scale bar: 100 nm) (b) Optical dark field image of MoS_2 triangle on the top nanogaps.

4.7.3 Raman Mapping

To further evaluate the suspension of the 2D TMDs on the nanogaps, we have performed the Raman mapping. The Raman spectroscopy gives us experimental evidence to differentiate between suspended and supported monolayer MoS_2 on Nano gap electrodes. An area of 11pixel × 8 pixel was selected on the nanogap electrode for scanning Raman map, with excitation energy of 2.41 eV (532 nm) as illustrated in Figure 4.9 (a). A beam spot of 400 nm was focused on sample with 1% power and integration time set to 10%. Raster scanning was implemented, which collected about 88 points of the scanning Raman map. Two points P1(supported) and P2(suspended) on the map are examine. The Raman peaks at points P1 and P2 show linear intensity change and shift in peak positions as shown in Figure 4.9 (b). At a glance, we can see that there is a linear decrease in intensity from the supporting substrate. This difference in intensity can be explained by the absence of scattering substrate underneath the MoS_2. When the Raman beam an incident on the supported area MoS_2 the signal bounces back with higher laser power than compared to suspended MoS_2 in

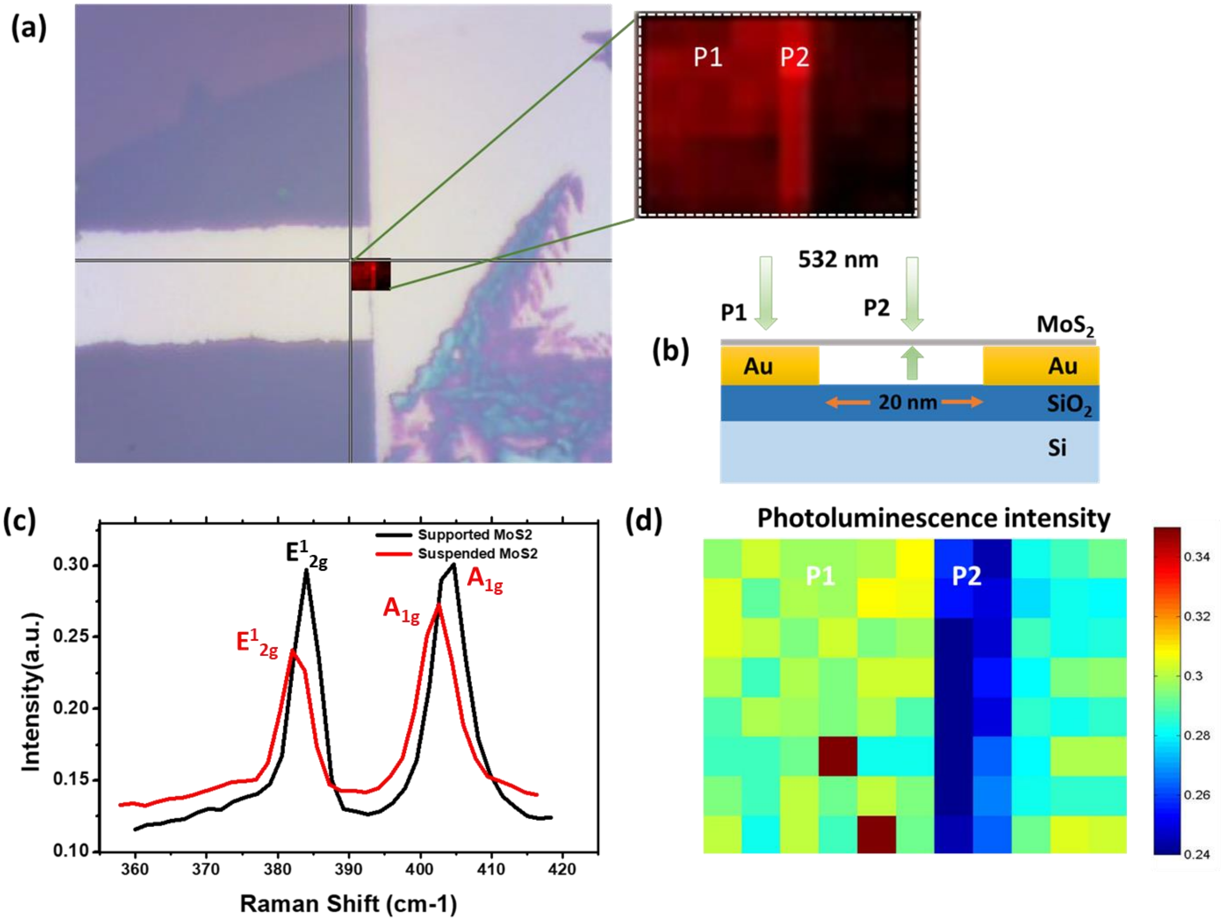

Figure 4.9: (a) Optical image of nanogap and highlighted Raman mapping area points P1 - supported and P2 - suspended, (b) Schematic of device arrangement for Raman mapping, (c) Raman spectra for supported and non-supported MoS_2 and (d) Photoluminescence intensity of MoS_2 on supported and non-supported substrates.

the absence of substrate. On the other hand, the relatively low intensity of suspended MoS_2 is due to increase in out-of-phase motion of the Sulphur atoms with reduced surface scattering.

Further inspection of the Raman spectra evaluates that there is a slight shift of 2 cm^{-1} (blue shift) associated with E_{12g} and A_{1g} on the supported as shown in Figure 4.9 (c). It can be understood that changing the number of layers will affect the intensity and location of the E_{12g} and A_{1g}. A blue shift of A_{1g} and red shift of E_{12g} is prominent as layer increase as demonstrated in Figure 4.9 (d) [127]. In previous reports, it has shown that MoS_2 suspended having a red shift due to contributions from residual strain, stress and doping [127, 128].

4.8 Depositing the dielectric layer

Top gating is very important in the FET devices because the back-gate FET requires more power (input gate voltage) to turn ON the device than the top gate, which hinders making a low power integrated circuits and highly sensitive biosensor. Secondly, it is found that the mobility of the electron is 100 times smaller than the top gate, where mobility is inversely proportioned to the gate voltage, as shown in equation 4.1. The voltage requires to turn on the transistor in back side gating is more because it emphasizes the thickness of the Si and oxide, whereas in the top gate the dielectric thickness is only a few nanometers. Therefore in the nanogap device, we have used the top gating to achieve high transconductance by a small change in the gate potential. HfO_2 is considered as a dielectric material, and it was deposited by using atomic layer deposition (ALD) to passivate active material and electrodes. Since freestanding 2D material present on the nanogaps, which is robust and sturdy and does not allow to interact with the substrate after HfO_2 layer, the metal layer and for bioelectronics application linkers and antibodies.

4.9 TEM of cross-section

To further verify the MoS_2 is suspended after coating HfO_2 and metal electrode on the top of the nanogaps, we have done cross-section TEM imaging by fabricating TEM nanogap sample as shown in Figure 4.10 (a). In this experiment, a FIB/SEM dual system with a high resolution of (1 nm) transmission electron microscope with 40-120 kV range was used to create the sample. This type of sample preparation is most commonly known as FIB Lamella preparation, where SEM and FIB are arranged in 52° with each other. The sample preparation involves *i)* deposition of Pt on top of the sample, *ii)* milling top and bottom wedges to make the L-shaped bridge, *iii)* mounting the super sharp needle to the TEM sample and *iv)* Mount the wedges sample to the TEM grid to take the cross-section images. In this technique, a rectangular window of the Pt layer (10µm × 2µm

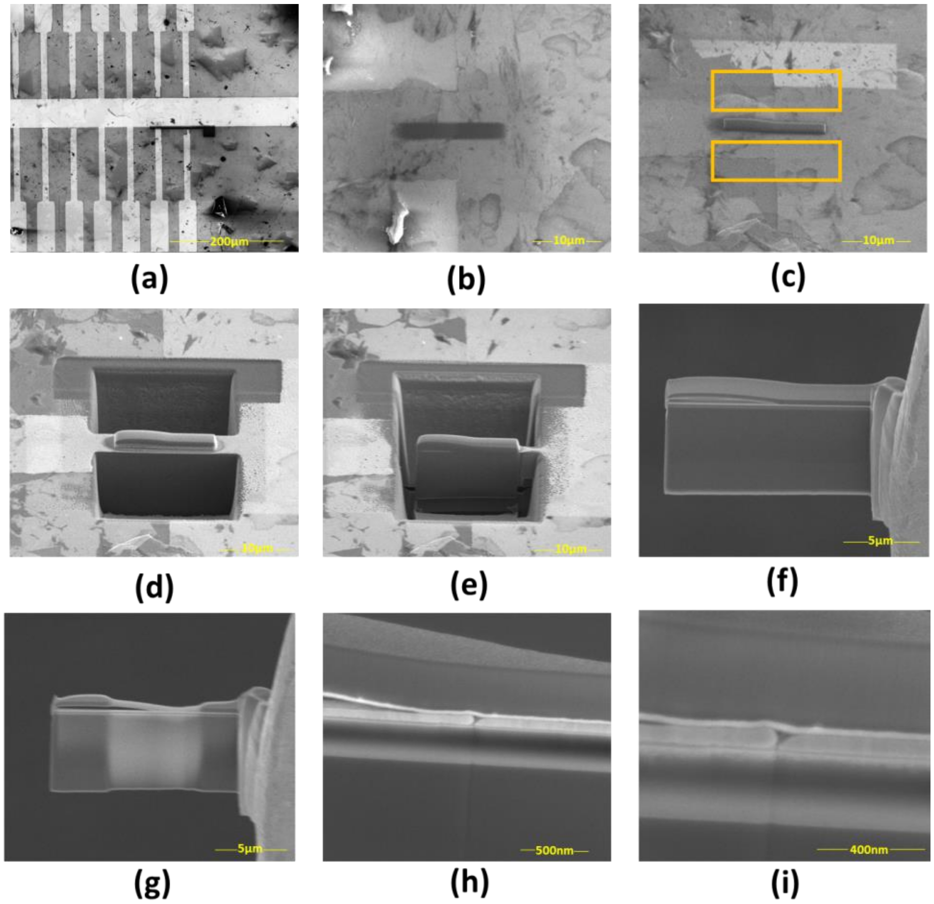

(a) (b) (c) (d) (e) (f) (g) (h) (i)

Figure 4.10: (a) A device with multiple nano gap electrodes, (b) Deposition of multiple Pt layers to form a 10µm × 2µm island, (c) Add markers to milling back and front side of the Pt deposition, (d) Sequences of milling makes trances, (e) L-Shaped milling done and lamella is free standing, (f) Micromanipulator carefully picks the lamella and welded to the TEM grid, (g) Slow thinning of the sample to get rid imperfections during milling, (h) cross section images after fine thinning and (i) high magnification cross-section images shows a nanogap of 10 nm.

× 300 nm) deposited on the selected area, as demonstrated in Figure 4.10 (b). The Ion-beam was set to standard deposition setting at 30 KV and 0.5 nA. The Pt island helps to recognize the assigned area to be milled and acts as a protective layer. Afterward, the milling has performed around the Pt island, it is important to make sure these highlighters are placed a few microns away from the island to protect from ion-beam damage as shown in Figure 4.10 (c). The sample is tilted by 52° toward the ion-beam for etching the backside and front side milling with a thickness of 20µm and 15µm respectively, as illustrated in Figure 4.10 (d). This milling is achieved in a few sequences of steps moving away from the Pt island. It takes about 30 min and creates a step pattern on the milled area. Once these trenches are formed, we have wedged the left side and shrill the bottom area to achieve the L shape of the milled sample (lamella) as shown in Figure 4.10 (e). Afterward, this lamella is welded on the manipulator and rest of the attached area is etched out to attain freestanding sample. Now the sample is carefully welded on to a TEM grid location, as shown in Figure 4.10 (f). Further milling was carried out to achieve appropriate thickness for TEM imaging as well as it removes the contamination came from welding, as shown in Figure 4.10 (g). The sample is then rotated by 90° to check the cross-section/plane view. Figure 4.10 (h) & (i) represents the SEM images of 10 nm gap between the electrodes, where MoS_2 and HfO_2 are suspended on it.

After making the cross-section TEM grid, we have performed transmission microscopy on the crystalline structure of the suspended MoS_2 film on the top of nanogaps. Figure 4.11 (a) represents the TEM image of the cross-section, where 2D MoS_2 is suspended between 10 nm of the gold electrodes even after coating of the dielectric layer and thick Pt metal. This image illustrates that the nanogap provides a very high mechanical strength to the atomic layer and shows the feasibility of the top gate transition. To further evaluate the image, we have performed the EDAX mapping to confirm the MoS_2 and HfO_2 are suspended in between the source and the drain. Figure 4.11 (b) represents the spatial distribution of Hf, Mo, Au was observed in EDAX mapping of the device region, thus confirming that MoS_2 is suspended in between the electrodes. Whereas Figure 4.11 (c), (d) & (e) shows the individual elemental mapping of the elements. This experiment

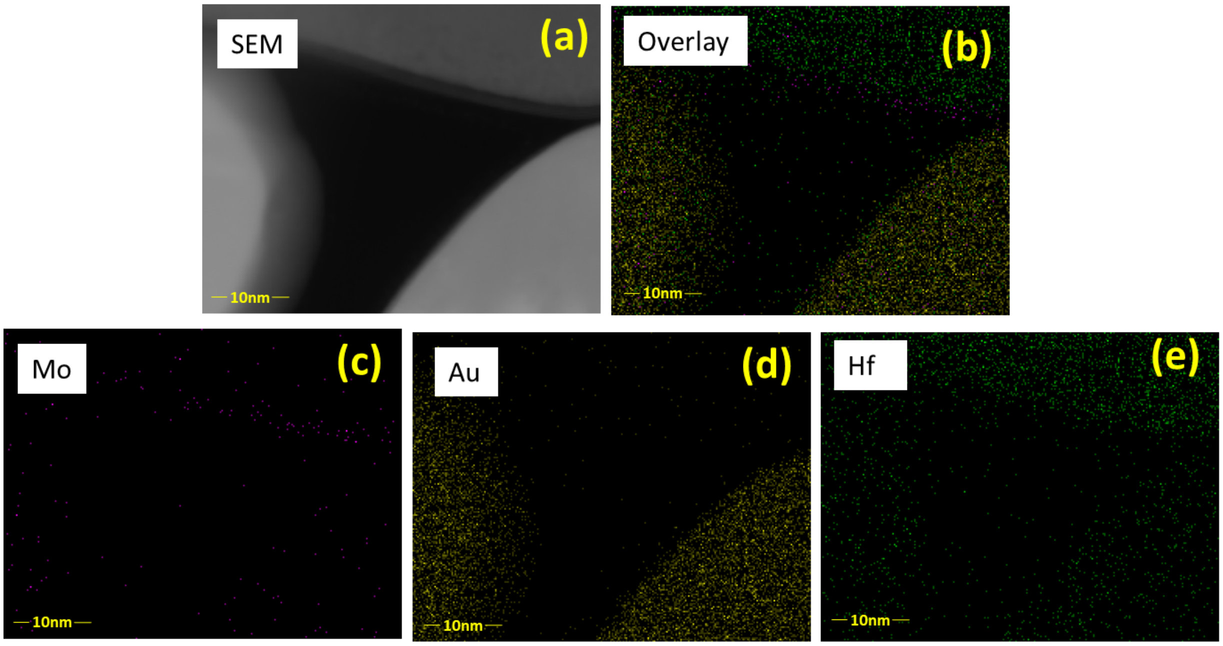

Figure 4.11: (a) TEM image of the cross section of suspended 2D material (b) EDAX overlay image of Mo, Au, and Hf, elemental mapping in the TEM instrument of (c) Mo (d) Au (e) Hf.

confirms that the nanogap provides strength to allow the use of top gating by eliminating the scattering phenomenon from the substrate.

4.10 Electrical characterization of suspended TMDs

After confirming the atomic layer are suspended in between the nanogaps and doesn't have any scattering effect even though the coating of the dielectric layer. The electrical properties of the p-FET WSe_2 and n-FET MoS_2 channel are performed by applying gate potential from the metal electrode deposited on the top of the oxide layer. Figure 4.12 (a) shows the p-FET transfer curve (I_{DS}-V_{TG}) by applying the gate voltage from 1.0 V to -1.0 V at voltage 100 mV. Whereas, the n-FET transfer curve of channel material MoS_2 as represented in Figure 4.12 (b), where top gate voltage sweeps from the -1.5 V to 0.5 V. It is interesting to find that, WSe_2 creates the p-type of the transition with the gold electrode, where holes are the majority carrier (discussed in section 3.4.2). According to these two-transfer curves (I_{DS}-V_{TG}), 2D WSe_2 i.e. p-FET shows the higher

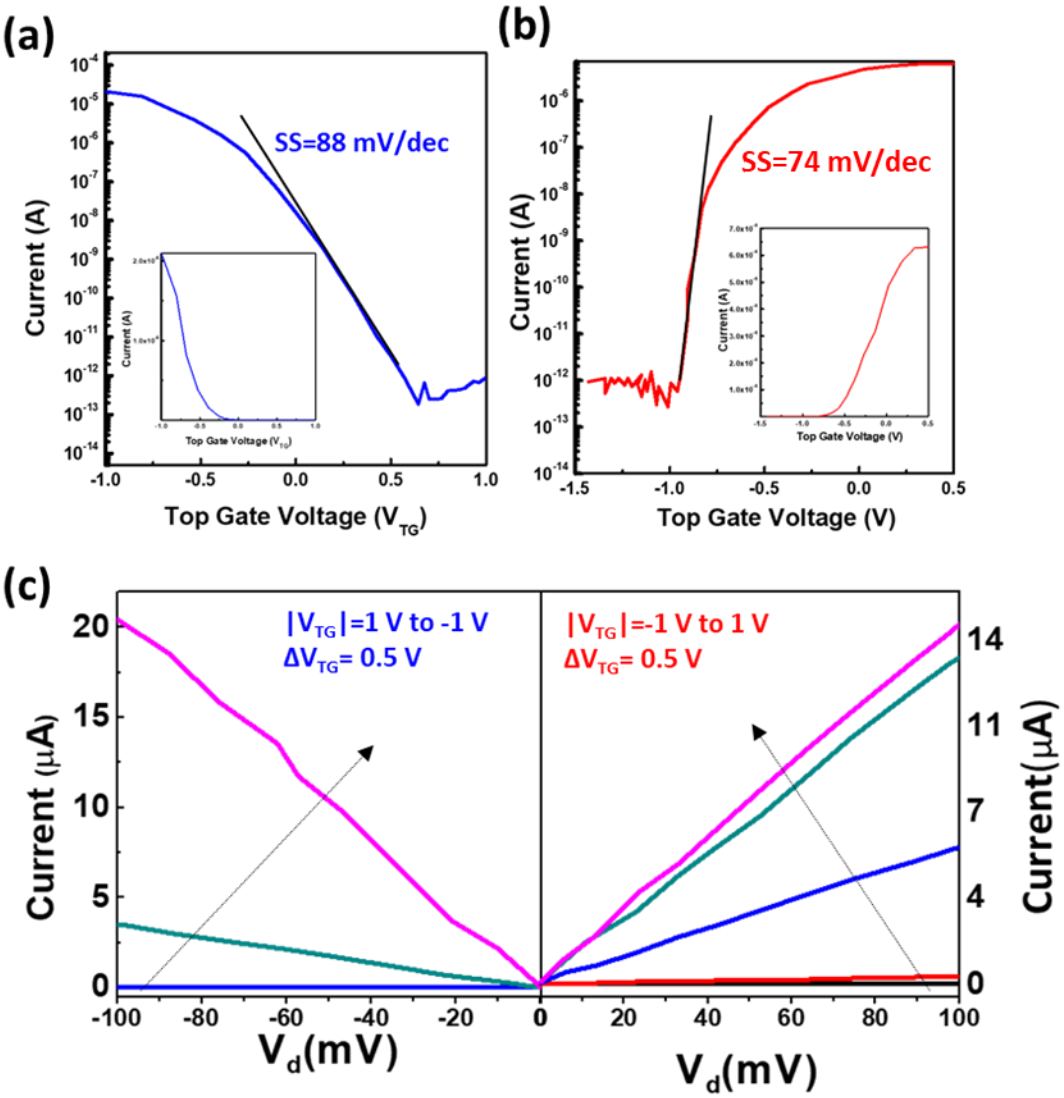

Figure 4.12 Top gate I_D-V_{BG} transfer curve of the suspended at 100 mV of (a) WSe_2 (b) MoS_2; (c) top gate I_D-V_{DS} charaacteristics of WSe_2 and MoS_2

magnitude of the current than the n-FET MoS_2, where threshold voltage (V_T) is found to be-0.37 V (p-FET) and -0.6 V (n-FET). As compared to the bottom gate, this is one order magnitude smaller i.e. top gate requires less power than the bottom gate to turn ON the device. The SS of these two transistors is found to be 88 mV/dec (p-FET) and 74 mV/dec (n-FET), which is far smaller than the back gating, which represents the suspended 2D FET is fast in response. The turn ON/OFF ratio of WSe_2 and MoS_2 channels as a top gate transition was found to be 10^8 and 10^8.

The mobility of the electron in the n-type is 1.2 cm^2/Vs and the p-type transistor is 1.4 cm^2/Vs calculated by equation 4.1, where capacitance is found to be 1.02 μF/cm^2. However, this is not the intrinsic mobility of 2D TMDs in nanogap channel length. To achieve real mobility, we have to consider the contact resistance between the metal and the semiconductor. Afterward, to evaluate the contact resistance, we have performed the I_{DS}-V_D characteristic at a different voltage, as shown in Figure 4.12 (c). It is found that the WSe_2 possess holes current, which flows by applying the negative potential at the gate, whereas the positive potential activated the MoS_2 channel where majority carriers are electrons. To further evaluate these transistors, we have fabricated the inverter circuit by using 2D NMOS and PMOS. The circuit diagram of the inverter is shown in Figure 4.13 (a) subset, where V_{DD} is connected to the PMOS and ground is connected to the NMOS. Constant voltage (V_{DD} and ground) is provided by the electrometer, whereas the output was measured by the source meter. In this measurement the negative voltage turn ON the PMOS, which is connected to the 100 mV source, whereas at positive potential turn ON the NMOS, which is connected to the

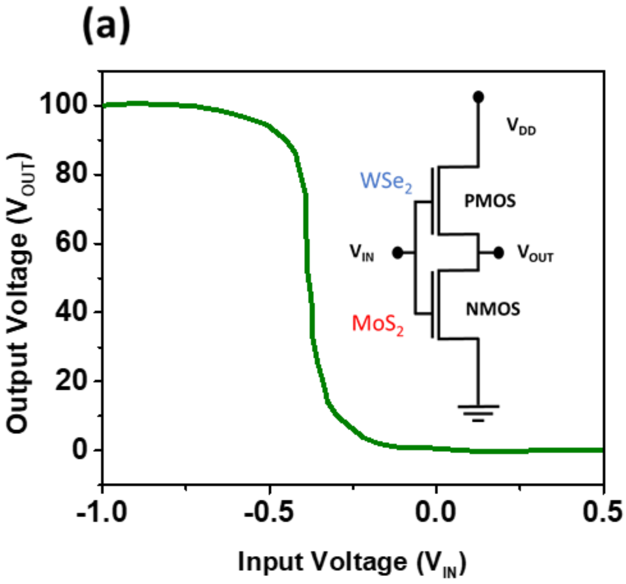

Figure 4.13: (a) PMOS WSe_2 and NMOS MoS_2 suspended inverter where negative input potential gives positive output and positive input provides negative output

ground i.e. 0V. This is the first type of the integrated circuit that is fabricated by the 2D suspended MoS_2 and WSe_2 atomic layer on the top of the nanogaps represents the next-generation electronics, where scalability is possible due to small channel length and no scattering effect enhance the mobility and the SS.

4.11 Summary and conclusion

In this chapter, a new technique of the photolithography "self-assembly" was adapted to achieve nanogaps between the metal electrodes. Here, few parameters have optimized while fabrication such as lift-off resists thickness, rpm rate of spinning photoresist, baking, developing photoresist, avoiding the residues during fabrication and most important optimization thickness of metal electrode layer. Nano-spacing between electrodes only depends upon the thermal expansion of the chromium. Therefore it is important to maintain the temperature of wafer for overnight. In this case, more the temperature bigger the spacing between two electrodes, RT showed a gap between 10 nm to 60 nm, whereas 60ºC exhibited near about 100 nm. Nano-gaps cannot be seen via microscope therefore prior to transferring the 2D material open/short circuit characterization technique is carried out. I-V between two electrodes is measured in the probe station; if the current is not flowing from two electrodes (open circuit), then nanogap is present in those electrodes.

After achieving the nanogap electrodes, we have developed a novel way to transfer 2D material by a dry stamping method. These dry stamping methods allow us to transfer the 2D material on the specific area without any wet contamination. Later, to check the 2D material is not sagging or touching to the substrate, we have performed AFM mapping, SEM on the top of nanogaps, dark-field spectroscopy, and Raman mapping. These characterizations illustrated that the nanogaps provide suspension as well as mechanical strength to the 2D materials, which do not allow to interact with the supporting substrate. After confirming the 2D material are sturdy on the top of the nanogaps, we have deposited 25-30 nm HfO_2 and then metal gate electrode for top gate transition. To further evaluate the 2D materials are not touching after coating of the HfO_2 and metal layer, we have performed the TEM of the cross-section. In this technique, the TEM sample was made from the ion beam and FIB, which demonstrated the 2D material are intact and freestanding between two electrodes, even the coating of the HfO_2 and gate metal.

The suspended 2D material on the top of nano-gap shows higher electron current transport by reducing scattering effect from the substrate morphology as illustrated in FET characteristics. For further evaluation, we characterized suspended I_D-V_{TG} transfer curve of MoS_2, which shows the SS of 66 mV/dec, which is near to ideal condition and the mobility 1.2 cm^2/Vs. I_D-V_{DS} at different gate voltages demonstrates that current is linear with respective the bias voltage, because of the no influence of the supporting substrate. Afterward, we have fabricated 2D material inverter with NMOS MoS_2 and PMOS WSe_2. This is the first type of suspended 2D material electronic circuit, which shows the high V_{dd} by applying a low voltage and low V_{dd} by applying high voltage. With this characterization, we can confirm that the substrate influence of single-layer 2D material is very prominent, and it can affect the electrical performance reliability significantly. Therefore, suspended 2D material devices can be advantageous in future microelectronic ICs and sensors by improving mobility, reliability, and the response time.

CHAPTER 5 SENSING FROM SUSPENDED 2D FET DEVICE

5.1 Introduction

Analogous to graphene 2D materials such TMDs are well known for there functionality in the semiconductor industry. Form these TMDs selenide, and sulfide-based 2D materials are well studied in the domain of FET biosensing applications. However, from all 2D TMDs, MoS_2 is found to be a promising candidate due to the biocompatible in nature, whereas selenide based TMDs (WSe_2 and $MoSe_2$) are investigated as carcinogenic [129]. Therefore, MoS_2 is becoming the most studied material in the field of bioelectronics and biosensing applications due to the high surface to volume ratio, and pristine structure, which makes it malleable to present fabrication techniques . MoS_2 based sensor in FET regime illustrated promising candidate in future of the sensing application. Such devices change their transconductance by changing the surface potential by biomolecule. The surface charge creates the field on the MoS_2, which alter the threshold voltage of the device according to the Nernst equation, which can implement to measure the concentration of the target analytes. These type of architecture are label-free sensing and employed for detecting the pathogens, proteins, DNA, and other biomolecules.

Due to the high fragility of the 2D materials, it requires an insulating supporting substrate, which does not interact with the transition of the electron. However, the supporting substrate uneven morphology scatters the electron, and trapped charges create the leakage and reduce the overall mobility. Therefore, when FET biosensor built on the supporting substrate, it provides an unreliable response in every single device. The other significant parameter, which dictates the sensitivity of the FET based sensor is subthreshold swing (SS). The SS and sensitivity relation is given by

$$Sensitivity = 10^{\left(\int_{V_{gi}}^{V_{gf}} \frac{1}{SS} . dVg\right)} - 1 \ldots\ldots\ldots\ldots\ldots..(5.1)$$

Where V_{gf} and V_{gi} are the final surface gate potential and the initial surface gate potential respectively before and after the attachment of the target analytes. From this equation, it is clear that the lowering the SS will increase the sensitivity. However, in the supporting substrate due to the scattering phenomenon, the requirement of the surface potential is high to drive the electron from 2D MoS_2 atomic layer. The higher magnitude of the surface potential increases the SS and reduce the sensitivity. Therefore, it is essential to eliminate the scattering phenomenon from the substrate for reliability and to enhance the sensitivity of the sensor.

Given the importance of the sensitivity and reliability issue, we have fabricated the suspended 2D MoS_2 devices (fabrication and FET characterization discussed in chapter 4) via nanogaps. These nanogaps provide strength to the 2D materials and don't allow to interact with the supporting substrate even after depositing dielectric layer and the linkers and antibodies for selective sensing. It is noted that apart from dielectric layer different polymer, functional group and lipids can be used to cover channel, which is called "effective layer" [130, 131]. The effective layer is used to achieve specificity so that the other non-specific biomolecule cannot directly get absorbed on channel material. However, most of the specific molecules such as linkers and antibodies functionalize directly on bare channel surface which creates defects on the material.

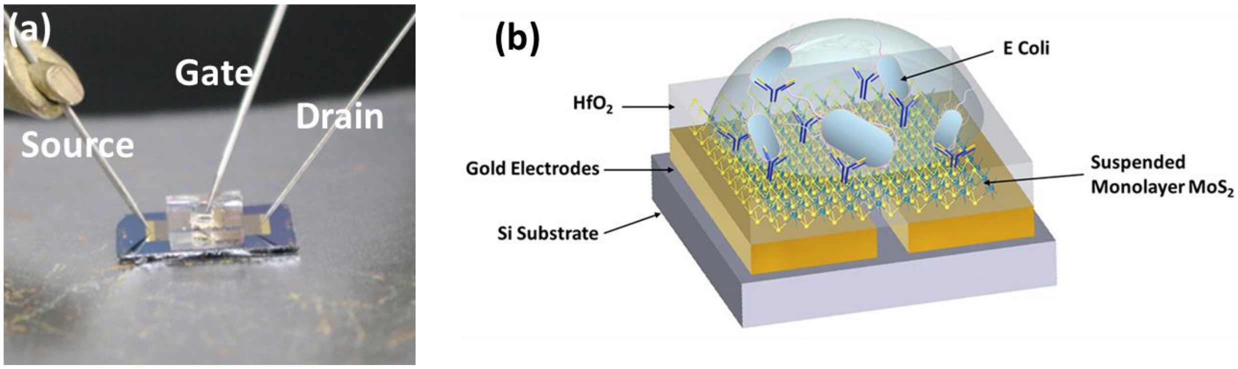

Figure 5.1: (a) Image of biosensor device with Source, Drain, and Gate (Ag electrode) connection (b) Schematic of Biosensor with E-coli and antibodies.

These defects bring a large variation in response. Moreover, when linkers/antibodies directly attached to the bare channel, the transduction mechanism is the combination of the electrostatic gating, direct charge transfer, and mobility modulation. Therefore, it's desirable to eliminate the density of defects by covering bare channel material with insulating material and then functionalize linkers and antibodies on the top of the insulator [15]. HfO_2 is used as a dielectric material, which is deposited via Atomic Layer Deposition (ALD). Afterward, macro fluidic storage is fabricated using Polydimethylsiloxane (PDMS) for encompassing electrolyte droplets, which is placed precisely on the top MoS_2 triangle covered with HfO_2. A reference electrode (Ag/AgCl) is used to apply bias through the electrolyte for stabilizing the process and better control of the operation under the biosensor regime, as shown in the optical image of Figure.5.1 (a) [132]. Figure. 5.1 (b) represents the schematic structure of the suspended MoS_2 FET biosensor by selective detection of the *E. coli* bacteria. Thus, this structure of suspended 2D FET is advantageous for label-free and unambiguous transconductance from target biomolecule only.

5.2 Ionic gating of suspended FET

The electrostatic effect of MoS_2 FET investigated to compare the electrical performance of the suspended devices. Initially, current-voltage (I-V) characteristics were evaluated by applying different gate voltages (back gate and ionic gating) of fabricated suspended devices in a dry and wet environment. Figure 5.2 (a) illustrates the I_D-V_{BG} curve of free-standing MoS_2 at 100 mV bias voltage (V_{DS}), where suspended channel length is ~90 nm. The suspended device represents excellent ON/OFF ratio 10^7 and threshold voltage (V_T) 3.9 V as compared at room temperature. The improvement of the $V_{T,}$ i.e. switching of the device at low voltage as comapare to the supporting one (discussed in chapter 3) is due to the elimination of the supporting substrate. The holder substrate confines the electrons mean free path by scattering as well as trapped charges on

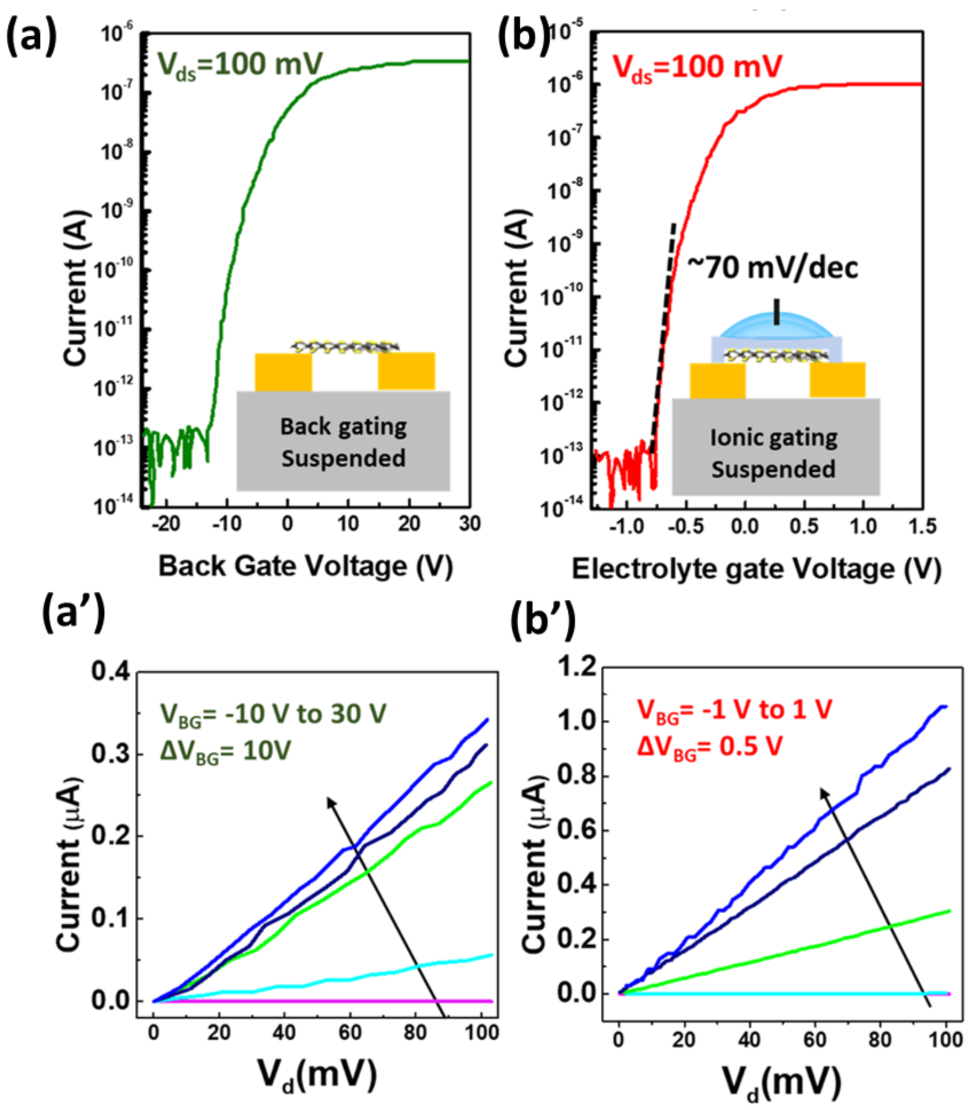

Figure 5.2: (a) back gating of suspended MoS_2 with 90 nm channel length (b) Ionic gating of suspended MoS_2. Current-drain voltage characterization (a') Suspended MoS_2 with back gating from -10 V to 30 V. (b') Suspended MoS_2 with ionic liquid gating from -1 V to 1V.

the surface [133]. Figure. 5.1 (a') represents the I_D-V_{DS} characteristics at different V_{BG} (-10V to 30V). In this case, the V_{DS} varies from the 0 mV to 100 mV and output current shows the linearity with the input voltage, which confirms that MoS_2 has ohmic contact with the Au/Ti contacts. Suspended FET displays better V_T and an ohmic contact with metal in back gate voltage characteristics as compare to supported one discussed in chapter 3, but due to the high power consumption, it is not feasible to use in biosensor domain. Therefore, we have used a thin dielectric layer of the HfO_2 on the top of the channel and studied the ionic gating effect on the suspended MoS_2 channel as shown in Figure 5.2 (b) and (b'). Phosphate buffer solution as an electrolyte has been used for the ionic gating measurements by transporting drop in macro fluidic storage. I_D-V_{LG} analysis of suspended ionic gating FET displayed impressive Subthreshold swing (SS) 70 mV/dec, which is near to ideal at room temperature as well as the ON/OFF ratio (10^7) and V_T (-0.29 V). Low SS, threshold voltage, and elimination of substrate scattering make these type of the FET structure more sensitive as well as consistence with better gate controllability in a wet environment.

5.3 pH sensing

After achieving excellent performance in the ionic gating effect, the suspended device investigated by changing the pH of the electrolyte solution. The pH sensing strongly depends upon the proton (H^+) present in the electrolyte solution react with the OH group on HfO_2 surface, which causes the protonation and deprotonation, as shown in Figure 5.3 [134]. Depending upon the pH value of the electrolyte solution, the dielectric surface charge of the suspended FET varies, a lower pH value protonates the surface by generating OH_2^+ on the HfO_2 whereas the higher pH value deprotonates the surface by extracting H^+ [135, 136]. The surface potential change can be related to the capacitance between the dielectric layer and the semiconductor channel, which is given as

$$\frac{d\emptyset_s}{dpH} = -2.3\alpha\frac{k_B T}{q} \dots\dots\dots\dots\dots (5.2)$$

$$\alpha = \left(2.3\frac{k_B T}{q^2}.\frac{C_s}{\beta_s} + q\right)^{-1} \dots\dots\dots\dots\dots (5.3)$$

Where $\emptyset_s$ is defined as the surface potential on the dielectric layer, K_B is the Boltzman constant, T is temperature, q is the charge of the electron, β_s intrinsic buffer solution capacity, and C_s is the

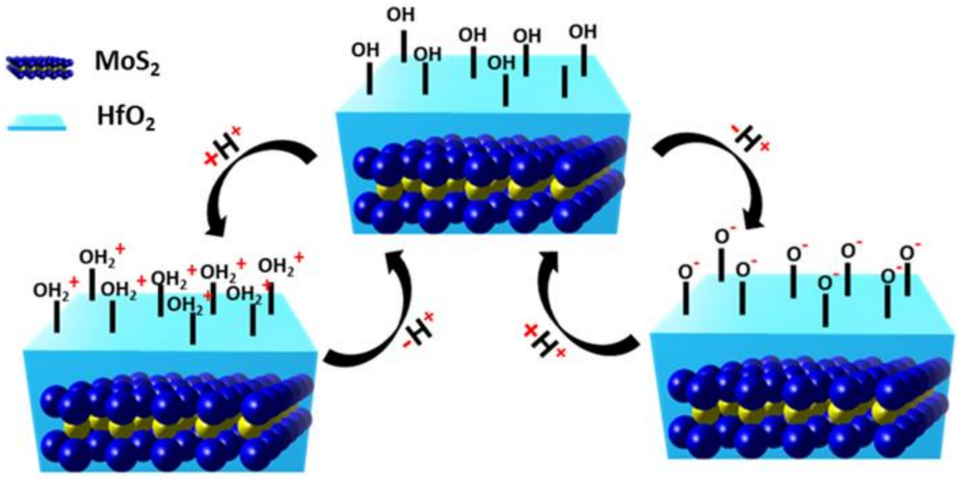

Figure5.3: Schematic of protonation and deprotonation on HfO_2 substrate.

electrical surface capacitance. According to the Nernst equation, the ideal shift in the threshold voltage on the dielectric surface is found to be 59.3 mV/pH at 300K. When the α tends to 1 at room temperature, then the change in potential on the dielectric from initial to final pH value will be ideal i.e. 59.3 mV/pH.

Figure 5.4 (a) represents the drain current (I_D) (100 mV bias voltage) at different pH value (3, 5, 7, and 9) by changing the electrolyte gate voltage (V_{LG}). It is found that the V_T of I_D-V_{LG} curves shifts to the positive side from low to high pH due to the negative charge developed on the dielectric surface. The shift in ΔV_T found to be 59.1 mV/pH, which is satisfied the Nernst limit at room temperature, i.e. 59.3 mV/pH and agree with early studies of ISFET characterization on HfO_2 [137, 138]. Therefore, HfO_2 does not require any functionalization for pH sensing as compared to the SiO_2 whose change in threshold voltage found to be 30-40 mV/pH [139, 140]. Figure 5.4 (b) represents the sensitivity of the pH at three different regions (Subthreshold, saturation, and linear), which is defined by the equation (5.4), where S_n is the sensitivity of pH, I_{pH1} and I_{pH2} are the drain current achieved from two different pH values (where pH1>pH2).

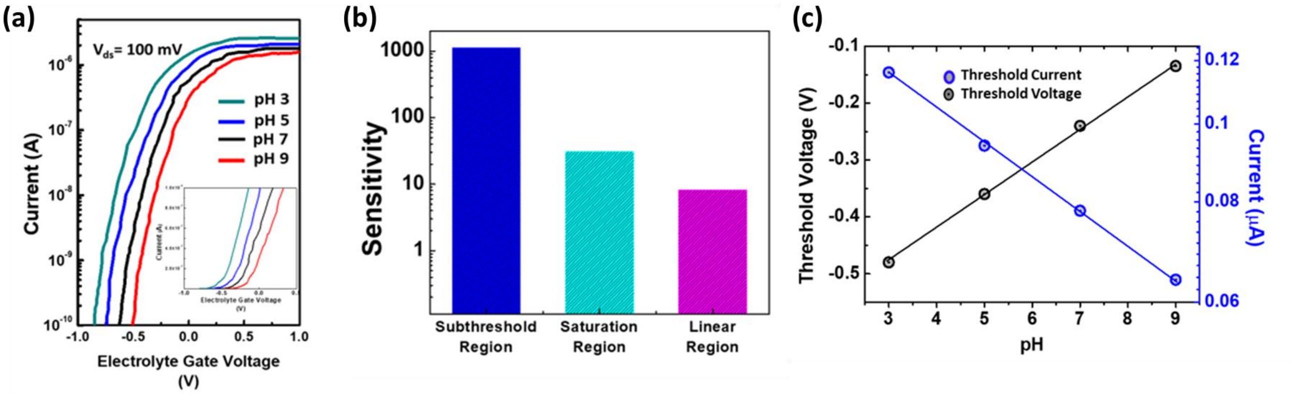

Figure 5.4: pH detection of suspended MoS_2 FET (a) I_D-V_{LG} curve of different pH concentration on the suspended MoS_2 (subset: Linear graph of I_D-V_{LG}). (b) Sensitivity of pH in subthreshold, saturation, and linear regions from pH 5 to pH 7. (c) experimental threshold voltage of suspended MoS_2 FET from pH 3 to pH 9 (Left-axis); experimental current corresponds to threshold voltage (Right-axis).

$$S_n = \frac{I_{pH1}-I_{pH2}}{I_{pH2}} \times 100 \ldots\ldots\ldots\ldots(5.4)$$

The sensitivity at subthreshold region found to be much higher because of the drain current is an exponential function of the gate voltage, whereas the saturation and linear regions are the quadratic and the linear with a change in gate potential. In a suspended device, the sensitivity at subthreshold region was found to be ~876 from pH 5 to 6 and ~880 from pH 7 to 8 respectively, which is far better than the previous reports of MoS_2 FET biosensor on the supporting substrate [16]. The suspended MoS_2 FET possesses higher sensitivity than supported one because of the lower SS, where SS defined as the

$$SS = dV_{LG}/d\log_{10} I_D \ldots\ldots\ldots\ldots\ldots(5.5)$$

This equation elucidates that the change in subthreshold current by one decade is a function of the applied gate voltage. Whereas, the consistency in the sensitivity of suspended device at two different ΔpH range is due to the elimination of the external scattering from the supporting substrate. Figure 5.4 (c) represents the threshold voltage and current on the suspended device at different pH value, which satisfy the nearnst eqaution i.e. change in the threshold voltage is 59,1 mV/pH.

5.4 Bacteria sensing from suspended FET

One more time suspended FETs are fabricated as described in the fabrication section. To specifically detect the *E. coli* bacteria from the buffer solution (pH=7.4), linkers were immobilized on the top of the HfO_2. For evaluating the bonding of the linkers with oxide surface, di-thiol and (3-Aminopropyl)triethoxysilane (APTES) have used followed by glutaraldehyde treatment and antibodies immobilization. From two linkers molecules, APTES has shown promising I_D-V_{LG} curve shift while detecting bacteria as compared to the di-thiol. Initially, for finding a more sophisticated way to immobilized the biomolecule to achieve maximum change in conductance, we have considered two different types of linkers *(i)* silane and *(ii)* dithiol, which are well known in MoS_2 biosensor domain and commonly functionalize on the oxide and chalcogen surfaces [92].

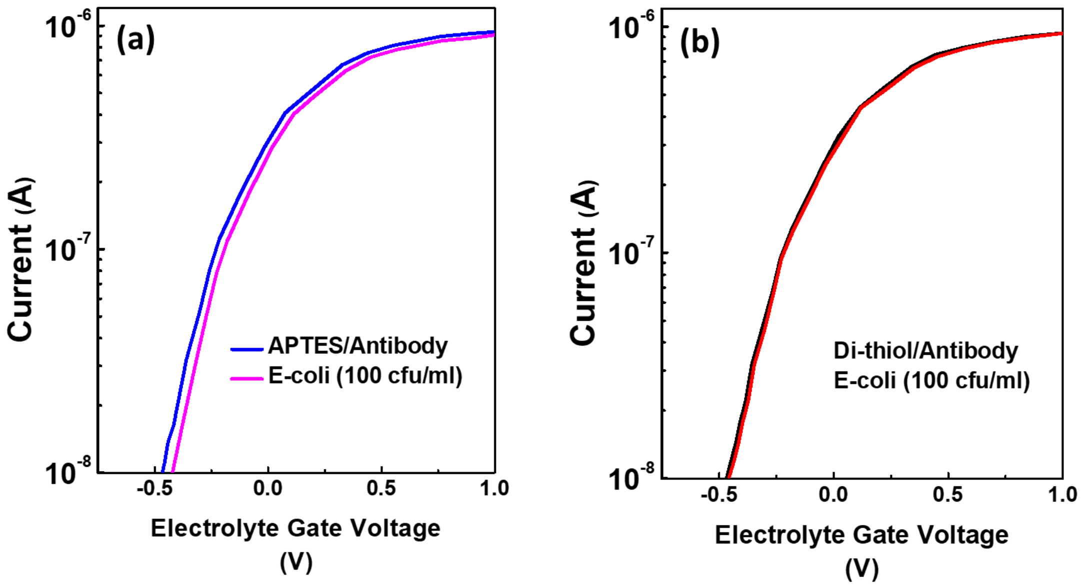

Figure 5.5: I_D-V_{LG} curve at constant bias 100 mV (a) APTES linkers with antibodies (Blue), 100 CFU/mL E-coli bacteria (Magenta) (b) Dithiol linkers with antibodies (Black), 100 CFU/mL E-coli bacteria (Red)

In general, the silane group on the oxide surface generates the silanol group, which tends to be a strong base for hydroxyl linkages between the HfO_2 and silane. After heating, it creates stable polymeric siloxane linkages [141]. In the second hand, dithiol does not create any bond with the oxide group, and it might be washed away after rinsing the surface. Therefore, the bacteria were trapped on the silane-based linkers and change the conductance more as compare to the dithiol, where there was no binding of the bacteria as shown in Figure 5.5 (a) and (b).

It is interesting to see that after functionalization of the APTES/glutaraldehyde linkers on the surface of the HfO_2, a small shift of the I_D-V_{LG} curve illustrated. The shift in the transfer curve is due to the MoS_2, which is the n-type of the semiconductor and possesses an electron as a majority carrier. In MoS_2 FET, when HfO_2 surface was modified with APTES, the magnitude of the current increased due to the generation of the positive charge on the dielectric surface. The APTES is

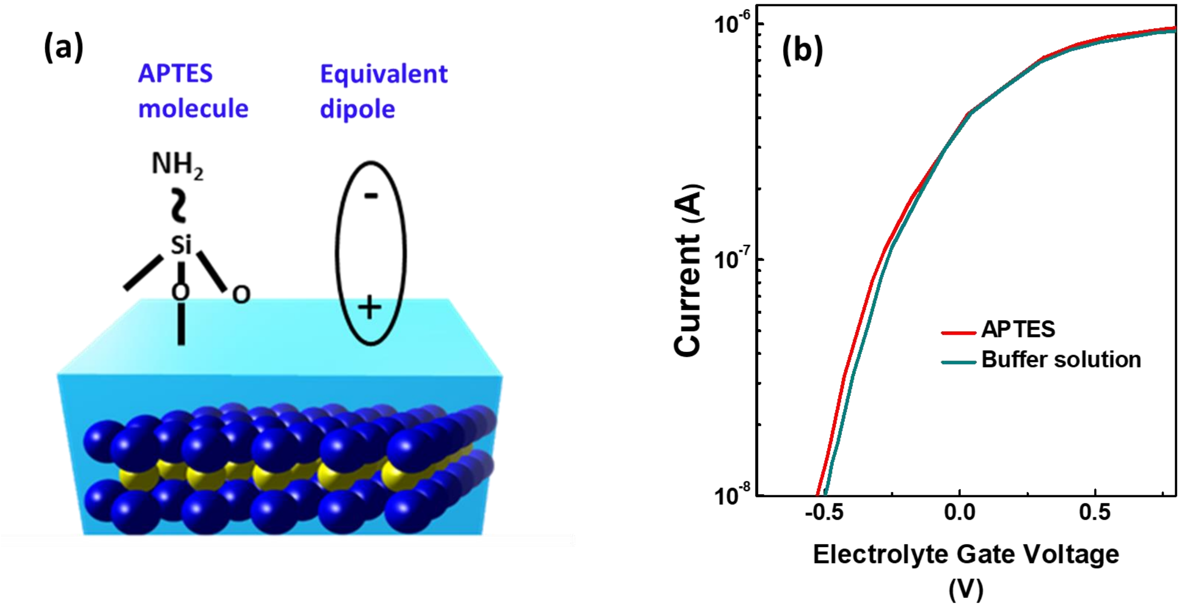

Figure 5.6: Inducing of electron by APTES molecule (a) schematic of the APTES molecule and the equivalent dipole (b) I_D-V_{LG} curve at V_{DS} 100 mV of buffer solution (Cyan) and functionalization of APTES (Red)

covalently attached with the OH group on the surface of HfO_2 and amine end is away from the surface, which implies that more electropositive end of the APTES molecule is near to the dielectric surface as shown in Figure 5.6 (a) [142]. Therefore, positive potential build on the HfO_2 layer after surface modification with APTES that induce more electron in the suspended MoS_2 channel and increase the magnitude of the current as illustrated in Figure 5.6 (b). After achieving the linkers and antibodies, the overall process flow of the linkers binding, antibodies immobilization on suspended MoS_2 FET through macro storage fluidic channel to detect *E. coli* was optimized as shown in the schematic of Figure 5.7 [143, 144]. Initially, the suspended device was absorbed into APTES for 2 Hrs in the mixture of ethanol/water followed by the cleaning of the chip by ethanol and blow-dried. Then, APTES functionalized chip was immersed in glutaraldehyde solution for approximately 1 Hr. Afterward, *E. coli* antibodies were incubated to the suspended chip in 0.05 M PBS solution for 2 Hrs. at room temperature.

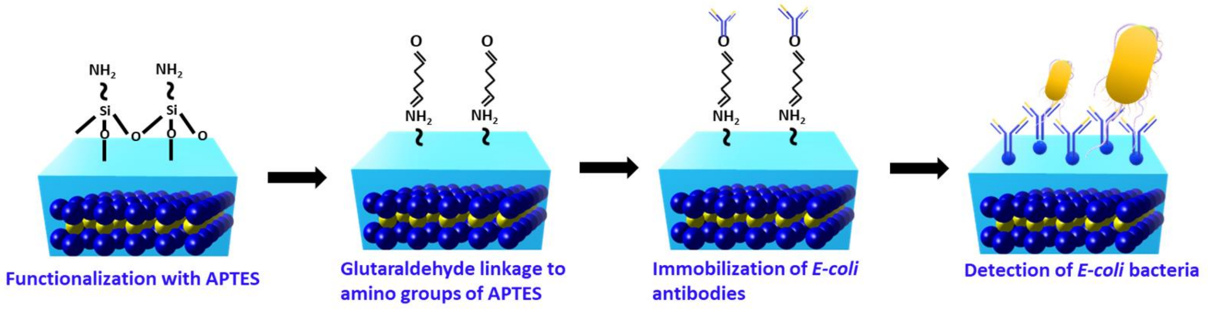

Figure 5.7: Schematic diagram of self-assembly process for immobilization of E-coli bacteria on HfO_2 surface.

The I_D-V_{LG} transfer curve of the linkers, antibodies, PBS buffer solution, and the 100 CFU/mL of *E. coli* bacteria was performed as demonstrated in Figure 5.8 (a). It is essential to introduce a buffer solution again after antibodies immobilization to confirm there is no change of conductance (Cyan curve in Figure 5.8 (a)). A shift found in I_D-V_{LG} curve on the left side after incubation of 100 CFU/mL of *E. coli* (Magenta curve in Figure 5.8 (a)).This illustrated the current

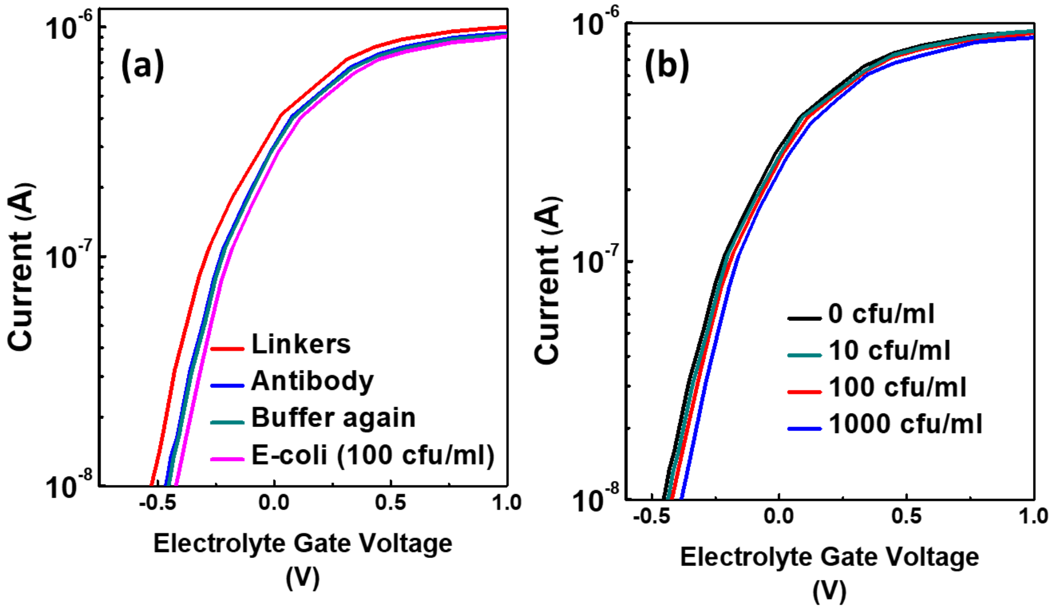

Figure 5.8 (a) I_D-V_{LG} curve of SAM process at 100 mV bias; Functionalization of APTES (Red), immobilization of E-coli antibodies (Blue), buffer solution 0.01 M PBS solution of pH 7 (Cyan), and detection of E-coli bacteria of 100 CFU/mL (Magenta). (b) I_D-V_{LG} characterization of E-coli bacteria from 0 CFU/mL to 10^3 CFU/mL.

in the MoS_2 channel deteriorated due to an increment of hole concentration induced on the dielectric surface by highly negative charged bacteria wall [53]. After achieving appreciable performance from suspended MoS_2 FET device, different *E. coli* concentrations ranging from 0 to 10^3 CFU/mL were prepared and used for detection. The increase in the concentration of the bacteria leads to the decrement of the MoS_2 channel conductance. For buffer solution, I_D at (V_{LG} = 0V) is illustrated 0.3 µA, whereas 10 CFU/mL shows the current response 0.274 µA, the change in the conductance of freestanding MoS_2 found to be ~9% with a low concentration of the bacteria. The change in conductance for 100 CFU/mL and 10^3 CFU/mL with buffer solution illustrated 18% and 25% respectively, as shown in Figure 5.8 (b).

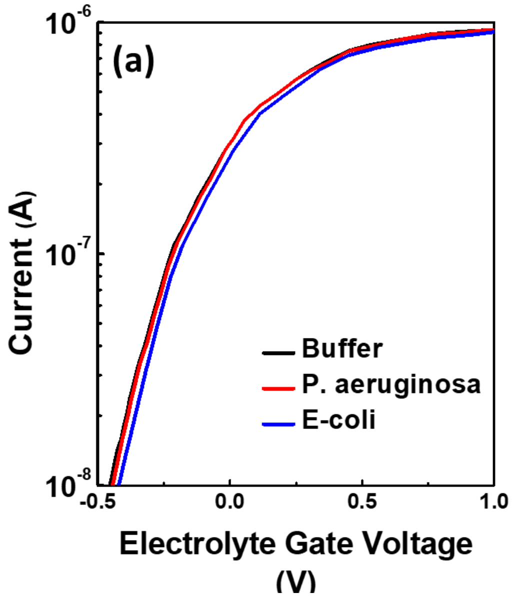

Figure 5.9: (a) Comparison of I_D-V_{LG} characterization of E-coli and P. aeruginosa bacteria (100 CFU/mL) with PBS buffer solution.

Another essential factor in biosensor domain is the selectivity, which attributes the other bacterial strain should not be attached with *E. coli* antibodies to achieve false signal. Therefore, *Pseudomonas aeruginosa* (*P. aeruginosa*) bacteria (100 CFU/mL) were considered to measure the I_D-V_{LG} signal by keeping V_{DS} = 100 mV. *P. aeruginosa* bacteria did not show any change in conductance as compared to the *E. coli* (100 CFU/mL) as shown in Figure 5.9 (a) after the incubation of 1 Hr. *P. aeruginosa* bacteria was not able to bind the customize E-coli antibodies (IgG) and fail to create enough field to shift the transfer curve.

After checking the shift in the I_D-V_{LG} curve and selectivity by the other bacteria, it is important to measure the sensitivity of the 2D suspended sensor. The sensitivity of the biosensor is defined as shown in equation (5.6),

$$S_{n(cfu/ml)} = \frac{I_{buffer}-I_{n(CFU/mL)}}{I_{n(CFU/mL)}} \times 100 \ldots\ldots\ldots\ldots..(5.6)$$

Where $S_{n(CFU/mL)}$ sensitivity, I_{buffer} is a buffer solution current, $I_{n(CFU/mL)}$ is current after bacteria bind to the FET biosensor. It was found that the shift in I_D-V_{LG} is more in the subthreshold region as compare to saturation and linear regions, as shown in Figure 5.10 (a). The sensitivity of the sensor in the subthreshold region calculated 83.3 for 100 CFU/mL of *E-coli* bacteria at -0.35 V.

Whereas in linear and saturation regions, this sensitivity become lower because the voltage in this regions are linearly and quadratic function of the change in the gate potential. After obtaining higher sensitivity, the other most crucial factor in the 2D FET biosensor is the reliability in every fabricated sensor, which can be easily affected by external scattering from supporting substrate or the contact resistance from metal. Till now, very few studies are undergone on the reliability of the 2D biosensor. In those investigations back gating was used, which has negligible sensitivity and requires high power. In our case, we have maintained the constant work function between the electrode and the MoS_2 in every single device as well as eliminate the supporting substrate interaction, which attributes the constant sensitivity in three suspended MoS_2 FET at the subthreshold region (100 CFU/mL and -0.35 V) as demonstrated in Figure 5.10 (b).

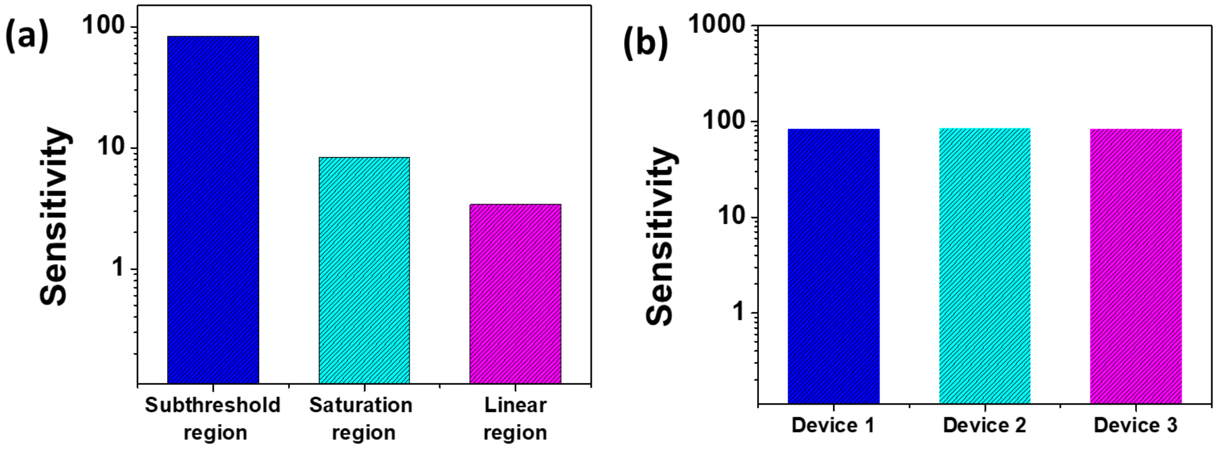

Figure 5.10 (a) Sensitivity measurement of E-coli bacteria at subthreshold, linear, and saturated regions. (b) Sensitivity comparison of three suspended MoS_2 FET devices by immobilizing the 100 CFU/mL E-coli bacteria.

5.5 Summary and conclusion

The sensitivity presented in this report is found to be impressive as compare to the previous reports of biomolecule detection via 2D FET based technology. Graphene-based FET biosensor has shown the conductance change of 3.25% at 10 CFU/mL of E-coli, which is almost three times smaller than the presented value (9% at 10 CFU/mL) [53, 152]. The detection limits of the graphene is due to the zero band gap in nature, which leads to an increase in the off-state leakage current and the SS value (SS is inversely proportional to the sensitivity) [153]. Proposed biosensor demonstrated the reliable and quantitative detection of pH and biomolecule by eliminating the scattering effect from the supporting substrate. A control experiment of pH sensing confirms the high sensitivity (~880/pH) as well as constant I_D-V_{LG} curve shift at different pH range (3 to 9). In

Target	**Channel materials**	**Detection limit**	**Sensitivity**	**references**
DNA	r-GO (reduce Graphene oxide)	100 nM	2.4 (low)	[145]
vascular endothelial growth factor	r-GO (reduce Graphene oxide)	100 fM	0.3 (low)	[146]
IgG	Graphene	290 pM	0.4 (low)	[147]
BSA	Graphene	300 nM	0.3 (low)	[148]
E-coli	Graphene	10 CFU/mL	*3% change in current at 10 CFU/mL* (low)	[53]
Streptavidin & pH	MoS_2	100 fM & pH	196 & 713 (High)	[16]
tumor necrosis factor-α (TNFα)	MoS_2	60 fM	0.19 µA mL ng−1 (Moderate)	[149]
DNA	MoS_2	10 fM	17 mV/dec (Moderate)	[150]
PSA	MoS_2	375 fM	0.23 nA/ 3.75 nM (Moderate)	[151]
***E-coli* & pH**	Graphene	10 CFU/mL & pH	*9% change in current at 10 CFU/mL* & 880 (ultra-high)	This work

Table 5.1: Comparison of 2D FET based biosensor

the second hand, FET based MoS_2 biosensor has shown promising sensitivity in biomolecule detection due to ~1.8 eV bandgap. However, the scattering effect from the supporting substrate increases the mean free path of an electron leads to the unreliable output from every single device, which is the significant barrier to proliferate this technology in biosensor industries [133]. Therefore, elimination of the scattering effect in the proposed biosensor shows the overall change of conductance in the 2D film is entirely by the change in concentration of the biomolecule. Table 5.1 represents a comparison of different 2D material based FET biosensor in terms of channel materials, detection limits, biomolecules, and sensitivity. Due to these merits i.e. the involvement of the CVD method, direct transfer technique, and optical lithography open the new avenues for the bulk fabrication of suspended MoS_2 biosensor.

CHAPTER 6 CONTRIBUTION AND FUTURE OUTLOOK

6.1 Summary of contribution

In spite of the excessive research work on the 2D materials in the last decade, still we lack a practical application which has a scalable process flow and reliable output from every single device. These issues are aroused due to the several factors (i) oxidation of the 2D material in the environmental condition, which reduces the overall conductivity (ii) Scattering effect from the supporting substrate, which brings reliability issues (iii) contact of 2D materials with metal, which affect the electron tunneling. These are some important aspects that are hindering 2D technology to commercialize the product at an industrial level.

Given the importance of the reliability and robust process flow issues, this research work focuses on the advancement of 2D material-based FET biosensor and microelectronics circuit by eliminating scattering effect and encapsulating 2D material to reduce oxidation. 2D channel material in the proposed FET biosensor is freestanding in between the nanogaps electrodes, which eliminated the scattering phenomenon from the supporting substrate. Nanogaps structure for building the highly reliable FET sensor allows applying top gating by depositing another insulating layer such as HfO_2, which keep intrinsic properties of 2D intact. Secondly, direct functionalization of the HfO_2 makes this sensor lable-free to detect the target analyte and provide unambiguous transconductance without any false results. Also, we kept the work function between the 2D semiconductor and metal constant, which provides a similar electrical output response from every fabricated device. This novel architecture of the FET eradicated all the possible factors, which distort the output signal and bring the reproducibility issue in the biosensing and microelectronics IC domain.

To achieve the above discussed FET architecture, initially, we have synthesized different semiconducting 2D TMDs and optimized it crystallinity based on the pressure, temperature, flow-rate, and amount of the precursors in the CVD process. Afterward, we have shown the process flow to fabricate the wafer-scale nanogaps and developed a novel dry stamping method to place this material on the appropriate region. The suspension of the 2D materials with and without dielectric layer is characterized by AFM, SEM, darkfield, Raman mapping, and the TEM spectroscopy. After confirming the 2D TMDs are suspended on the top of the nanogaps, we have fabricated NMOS and PMOS device and then inverter to check its feasibility in the microelectronics domain. However, selenide based TMDs has a toxic in nature, which hinders to make FET biosensor. Hence, CVD grown MoS_2 channel material transferred on photolithographically patterned nano-gaps to achieve suspension and covered with Hafnium oxide (HfO_2) as a dielectric material to eliminate direct functionalization on the channel material. Proposed biosensor demonstrated the reliable and quantitative detection of pH and biomolecule by eliminating the scattering effect from the supporting substrate. This architecture of biosensor has a capability to detect the low concentration of biomolecule because of the atomic layer as a channel material, scalable due to the involvement of optical photolithography, dry stamping, and CVD technique as well as reliable and reproducible due to the elimination of the supporting substrate. In Table 6.1, we have compared between different dimension and materials with respective their sensitivity, feasibility in bulk fabrication, and reliability with this research. These merits of suspended MoS_2 FET makes it promising next-generation sensing device for on-spot detection of biomolecule and bioelectronics applications.

Dimensions	**Materials**	**Sensitivity**	**Bulk Fabrication**	**Reliability**
3D (Bulk materials)	Si	Low ✓ Surface to volume ratio is low. ✓ Scattering of the electron due to 3D structure	✓ Conceivable due to well-matured Si technology.	High
1D (Nano-materials)	Si nanowires	High ✓ Surface to volume ratio is high therefore good electrostatic effect from biomolecules [154].	✓ The top-down fabrication is costly and low production yield; ✓ b) The bottom-up approach has a severe integrity issue.	Low
	CNT	High	✓ Fabrication of CNT FET is challenging due separation of semiconducting and metallic nanotubes.	Low
2D	Graphene	Low ✓ Excellent transconductance effect due to atomic layer. ✓ Low sensitivity due to semi metallic in nature [16].	✓ Low-cost mass production is conceivable due to pristine nature of graphene.	Low
	MoS_2 (Supported)	High ✓ Excellent transconductance effect due to atomic layer. ✓ High sensitivity due to present of bandgap. ✓ Scattering effect from supporting substrate doesn’t provide constant sensitivity.	✓ Low-cost mass production is conceivable due to pristine nature of MoS_2.	Low
	MoS_2 (Suspended)	Ultra-high ✓ Excellent transconductance effect due to atomic layer. ✓ High sensitivity due to present of bandgap. ✓ No scattering effect due to freestanding of MoS_2.	✓ Low-cost mass production is conceivable due to optical lithography and CVD. ✓ Patterning on different substrate is possible.	High

Table 6.1: Comparison of Suspended FET with other materials

6.2 Future Outlook

The field of Micro electro-mechanical system (MEMS) sensing and microelectronics has marched towards a fine combination between physical world and electronics. According to Yole Développement, 2015, the market value of the MEMS sensors shows an aggregate annual growth rate of 5–24% for the period 2013–2019 [155]. Further development of such type of semiconductor devices implicates towards the exploration of 2D materials in the sensor field. Before the discovery of 2D materials, selection of materials in MEMS-based sensor limited, which includes silicon, platinum, silver, gold, titanium, etc. These materials limit the sensitivity of the sensors that depends upon electrical conductivity, reactivity towards the physical world, and response to convert the physical signal into electrical [156, 157]. The emergence of 2D materials starting from graphene [47] and MoS_2 in the 2000s has significantly changed the direction of the future of MEMS. These materials are higher in conductivity, biocompatible, and extremely sensitive and fundamental nature of these 2D materials prepare it for fabrication in batch mode. However, due to the fundamental properties of the materials easily tailored from the environmental conditions, which hinders these technology to bring robust and reliable commercial product.

This research will be very helpful for building the 2D materials products such as sensors and the microelectronics circuits with no influence of any intrinsic factors. We have shown in chapter 4 possibility of the suspended 2D complementary metal-oxide-semiconductor (CMOS) by fabricating PMOS and NMOS inverter. Further, this structure can be implemented in more complicated circuits such as 16-bit and 64-bit IC's and enhance the performance of the operation due to high mobility and fast in response. The other application we have shown in chapter 5 is the sensing of pH and E-coli from the novel FET structure. However, by changing the specific self-assembly molecule, we can proliferate this suspended device in the real-time monitoring of medical, environmental, and industrial domain by integrating with transmission circuits and high power batteries.

APPENDIXES

APPENDIX A: MILLIMETER-SCALE LITHIUM-ION BATTERY PACKAGING FOR HIGH-TEMPERATURE SENSING APPLICATIONS

A 1.1 Introduction

In recent years, electronic industries are breaking previous boundaries of integration and functional density towards miniaturization in autonomous self-powered microdevices. These micro/nano machines are suitable to operate as well as interconnect in different environments to provide, process and store information without having any connection to power grids [158]. The autonomous devices should operate continuously without any power obstacle in natural, industrial or in-vivo applications of the human body [159-162]. As self-directed systems are shrinking day by day, energy storage systems have to be flexible with respect to dimensional constraints so that they can be integrated into the miniaturized devices [163]. Therefore, battery is the main power source in autonomous system and the improvement of miniaturized energy storage system with large volumetric density is of essential importance for MEMS-based sensors that deliver power at vigorous environment conditions [164]. However, present miniaturized batteries have several serious limitations including areal energy (µAhcm-2), size (around 80 mm^2) and thermal stability (up to 85^{o}C) [165]. In addition, several micro-sensors acquiring real-time information related to pressure, temperature, etc., at extreme environmental conditions demands highly reliable rechargeable miniaturized batteries sustaining temperatures up to 100^{o}C to 200^{o}C, works at high pressure and deliver power in the order of few mAhcm-2. Thus, miniaturized rechargeable batteries which can readily embed with microsystem and works at extreme conditions are a requirement of present autonomous devices in various industries.

By considering this problem in the account, here we present packaging of miniaturized rechargeable lithium batteries by using “3D printing” casings for high temperature (~120ºC) autonomous sensing applications. Miniaturized batteries contain electrochemically active components which must be protected from moisture, air, and mechanical stresses, therefore, packaging the battery components within millimeter configuration is extremely challenging for high-temperature applications. In addition, these batteries having millimeter size components need to be assembled in the inert atmosphere, which further complicates the process. Hence, tackling previously mentioned issues, a process flow has been developed to fabricate miniaturized batteries in the small domain by reducing the number of required components compared to conventional coin cell battery. Packaged miniaturized batteries in small geometrical dimension (2 mm to 5 mm) show minor self-discharge, long lifetime and high volumetric capacity at high temperature (120ºC). Moreover, to show integrability of the miniaturized batteries for typical autonomous sensor, room temperature solar cell charging and discharging at 120ºC in terms of different duty cycle has been performed.

A 1.2 Results and discussion

3D printers are gaining tremendous popularity in almost every industry due to its rapid prototyping of parts and machines by using Computer-Aided Design. This additive manufacturing technique is simple and shown its potential by manufacturing big houses to small extremely complicated human organs [166-168]. Therefore, we utilize “3D printing” technique (Direct metal laser sintering) to fabricate miniaturized battery casings by maintaining material properties (316 Stainless Steel) for electrochemistry compatibility. This battery casing contains two parts of 316 Stainless Steel, bottom case to hold the cathode material whereas the top case contains anode material, an extrusion has been added to the top case which aids sufficient contact pressure between the anode and cathode material as shown in Figure A1.1. At first, the optimized design had a wall thickness of 500 µm in 3 × 3 mm2 domain, which was later reduced to 200 µm in the 2.25 × 1.7 mm2 size casings illustrated in Figure. A1.1 (a) & 1(b). The requirement of the thinner wall is to increase the overall area of the cup which leads towards the increment of battery capacity by depositing higher loading of the cathode material. Afterward, the least wall thickness of the battery components set as 200 µm in all other dimensions (2mm to 5mm). In addition, 3D metal printers have a minimum resolution of 40 µm (±10 µm error) that provide a highly smooth surface in millimeter dimension as shown in Figure A1.1 (c) and allow us to reduce the further thickness of the wall. Though, it is not feasible to construct battery wall thickness less than 200 µm as it results in bending of casings while fabrication.

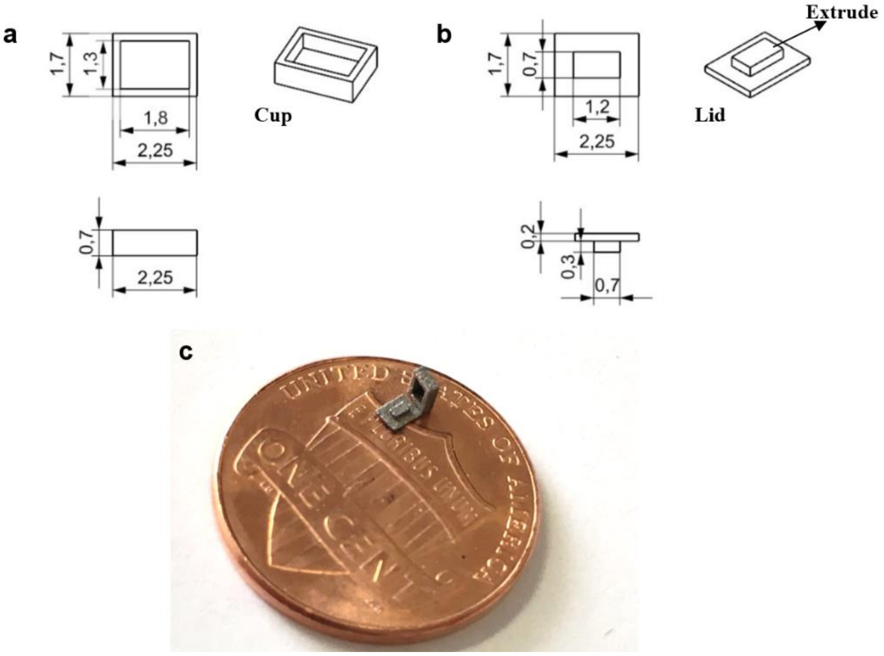

Figure A1.1: Battery casing design of 2.25 ×1.7 mm2 (a) Bottom case or cup for holding cathode material (b) Top case or lid for conformal coating of Lithium i.e. Anode (c) optical image of metal 3D printed casings

The next critical step to fabricate millimeter-scale lithium batteries is choosing epoxy or sealant, which would electrically isolate cathode and anode casings and at the same time to bind them tightly to regulate liberated electrons for the external circuit. These compounds with specific formulations are well studied and documented for their thermal and electrical properties to apply in the electronic industry [169-171]. However, the compatibility of these thermally stable epoxies with battery chemistries is unknown. It is very important to know the stability of selected epoxy with electrodes/electrolytes since it involves electrical energy (voltage) along with thermal energy which creates issues towards their stability. Hence, it was planned to study the selected epoxies (thermally stable) systematically towards battery chemistry by fabricating lithium batteries and testing them at a higher temperature. As shown in Figure A1.2(a), electrochemical performance of 4 mm battery sealed using silicone sealant is studied by conducting charge-discharge measurements at a constant current rate of 10 μA in the potential range of 2.5 - 4.5 V. Electrochemical test rate was performed on the silicon sealed 4 mm battery in an air atmosphere at 120 °C. Adversely, the battery is not charged completely due to undesirable side reactions of

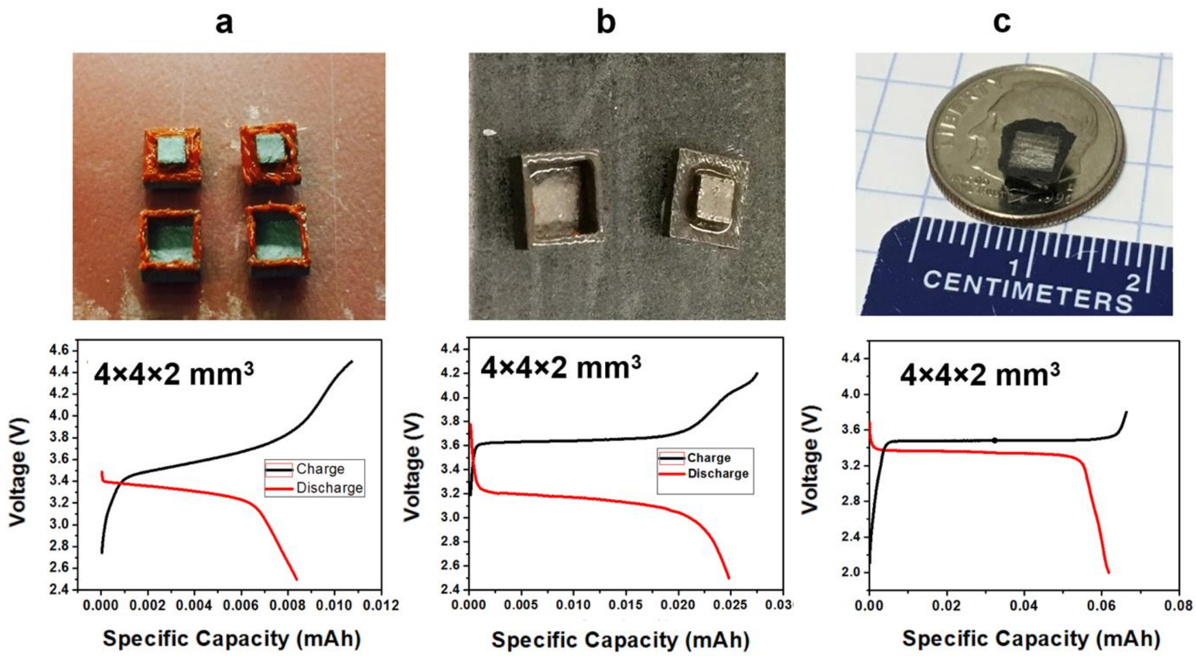

Figure A1.2: Epoxies optimization with 4 mm battery casings (a) Casings sealed using silicone epoxy and charge-discharge profile, (b) Casings sealed using master bond epoxy and charge-discharge profile, (c) Casings sealed using Urethane epoxy and charge-discharge profile

electrolyte/electrodes with atmospheric air. This kind of parasitic reactions because of silicone epoxy has not hermetically sealed the battery. Though, silicone sealant is capable of isolating cathode and anode compartments electrically even at 120°C inside the glove box, however it is incompatible with air atmosphere to seal the batteries. This is because of the oxygen permeable of PDMS (polydimethylsiloxanes) which is the main composition of the Silicon sealant [172, 173]. PDMS has high dielectric constant and preferable candidate for insulating materials, but it allows oxygen to penetrate through the surface due to which batteries are incapable to perform in an air atmosphere [173]. The next alternative sealant/epoxy for battery applications is on shelf Master-bond epoxy resin as illustrated in Figure A1.2 (b), the charge-discharge behavior of 4 mm battery at 120º C, wherein well-defined charge and discharge plateaus were observed around 3.4/3.0 V. The appearance of such a large polarization between charging/discharging plateaus indicates the unwanted side reactions from on shelf epoxy which rise the internal resistance. This epoxy resin might react with electrolyte while curing at 90 º C for 10 hours by releasing oxygen which reduces the movement of ions and increased the internal resistance of the battery. Finally, urethane based epoxies are used to seal the batteries as illustrated in Figure A1.2(c), the electrochemical performance of 4 mm battery sealed using urethane epoxy has carried out by the C/6 rate at a higher temperature. The perfect and well-defined charge-discharge voltage plateaus were observed, wherein the appearance of 3.4 V plateaus. Among the different epoxies used to seal the mm-scale batteries, cells sealed with urethane epoxy exhibits higher discharge capacity value and minimum polarization (less internal resistance). The discharge capacity of such a urethane epoxy sealed battery exhibits 62 µAh at 120°C with excellent capacity retention. The room temperature curing of urethane-based epoxies in 10 minutes makes a perfect candidate for mm battery sealing.

In addition, the magnitude of capacity is inferior compared to the batteries sealed with other epoxies at same loading of active material, which could be corroborated to the chemical and thermal stability of urethane epoxy.

After optimizing design and packaging epoxy, miniaturized battery fabrication process flow is evaluated as shown in Figure A1.3. In the assembling process, 3D printed Stainless Steel (SS) shell cup coated with cathode material ($LiFePO_4/C$) by spray ink technique as depicted in Figure A1.3(a). After drying out cathode material, separator and electrolyte (Room Temperature Ionic Liquid) are injected in the appropriate amount as illustrated in Figure A1.3(b). At Lid side, a dielectric layer (100 µm thick Kapton) is placed to insulate top lid from the bottom cup demonstrated in schematic Figure A1.3(c). After coating Lid with an insulating material, Lithium metal is applied to the extrude inside the glove box, i.e. inert environment as mentioned in Figure A1.3(d). Later, these two different prepared components of the battery are embedded together in an inert environment. Airtight urethane epoxy which cures at room temperature is applied to the exterior sidewalls of the SS casings as shown in Figure A1.3(e). The final optical image of

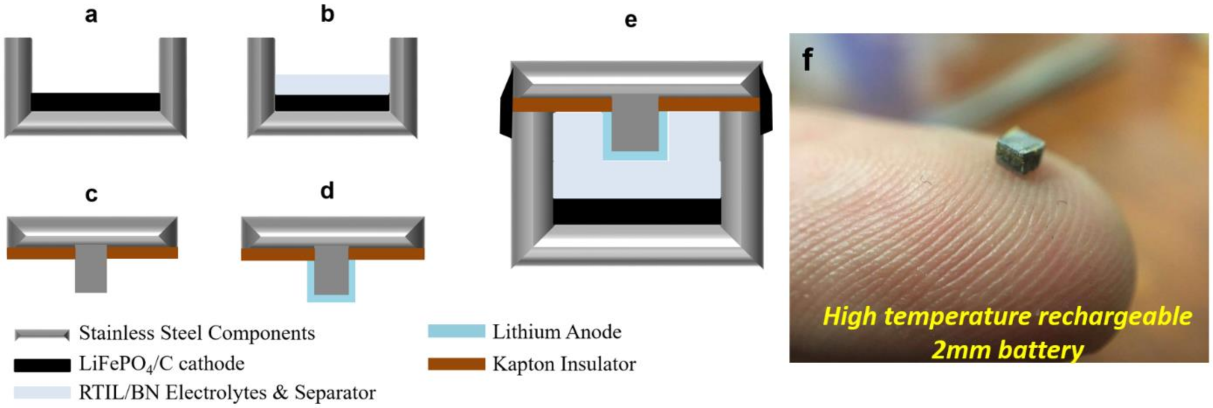

Figure A1.3: schematic of assembly process a. Cathode coated on to bottom Stainless Steel case by spray ink technology, **b**. RTIL electrolyte and quartz separator is added to bottom case inside the glove box **c**. Kapton added to top case to insulate top and bottom shell **d**. Lithium as an anode applied on top case projector inside the glove box **e**. Both **b&d** sealed together using Urethane epoxy **f.** Optical image of fabricated lithium battery.

fabricated 2 mm Li-ion battery by using urethane epoxy, 3D printed casings and optimized high temperature active materials as demonstrated in Figure A1.3(f). After curing epoxy, electrochemical performance of the packaged battery is tested according to the specification of sensors.

With the successful packaging of miniatured batteries and demonstration of its feasibility at 120ºC using urethane epoxy, it is important to further showcase its suitability for sensor requirements to use in an autonomous device. In this regard, we programmed our

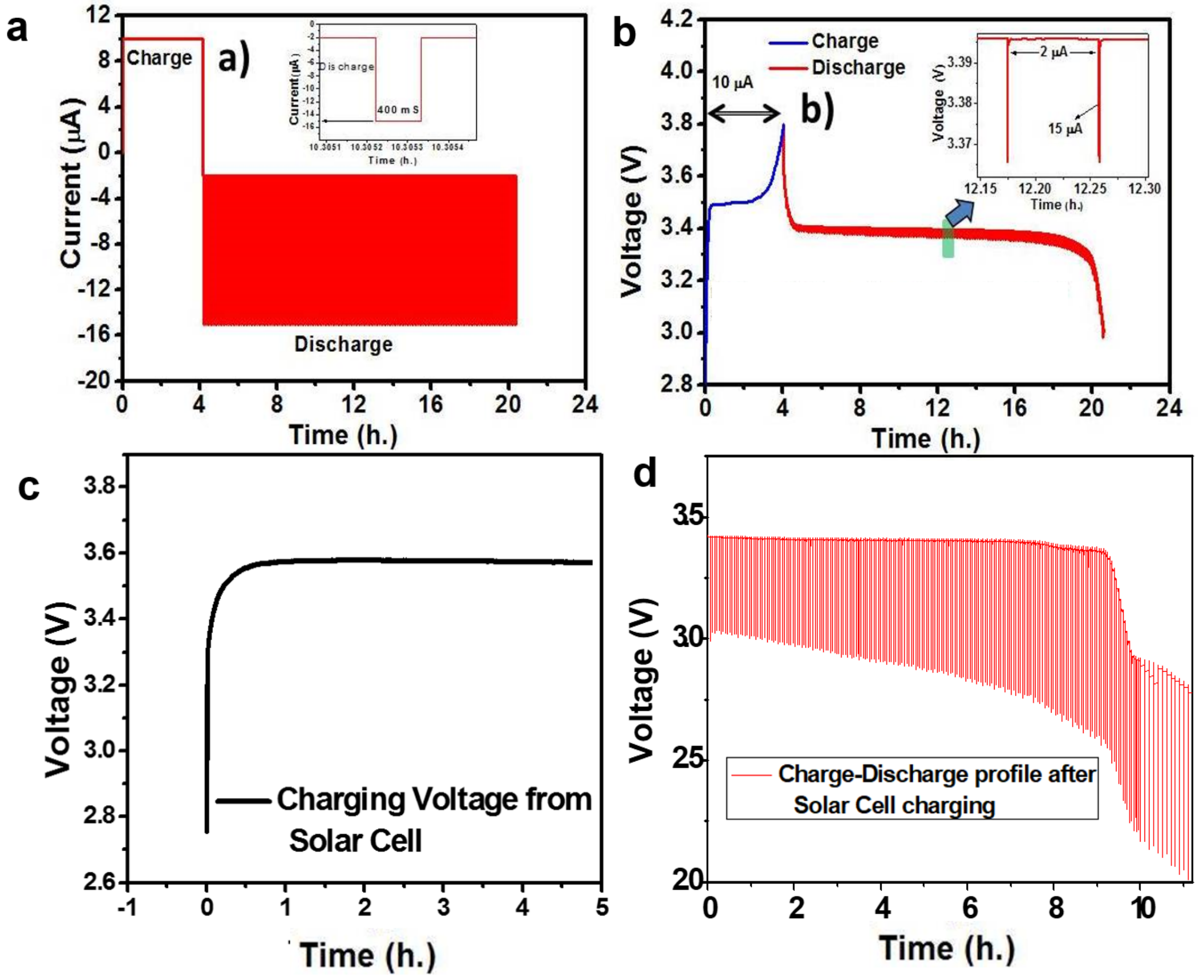

Figure A1.4 Duty cycle studies according to sensor applications on 3 mm battery a. Charing continuously at 10 µA in potentiostat with discharging current of 15 µA for 400 ms (active mode) with base current of 2 µA (sleep mode) **b.** Charging battery till 3.8 V at 10 µA and discharge with respective input active and sleep mode currents **c.** Charing at 15 µA for 5 h. by solar cell **d.** discharge voltage with respective input current of 200 µA for 500 ms (active mode) and continuous base current at 3 µA (sleep mode) of solar cell charged 3 mm battery.

galvanostatic/potentiostatic instrument in-accordance with the autonomous sensor wake-up program [174, 175] requirements and applied on newly packaged 3 mm battery. Figure A1.4 (a) reveals the input current conditions during the charge-discharge process where charging at 10 µA constant current and discharge current at 15 µA for 400 ms (active mode) in a regular 5 minutes interval with 2 µA of base current (Figure A1.4(a) inset). Figure A1.4 (b) demonstrates output voltage with respect to the time during the charge-discharge process in which cut off voltage is 3.8 V. It is noteworthy to know that the performance of 3 mm battery is stable for ~16h. at 120 °C under given conditions to be used in sensors.

For any battery control autonomous system, the key challenge is environmental energy harvesting particularly solar based ones. In this aspect, solar (Photovoltaic) charging of miniaturized 3 mm Lithium battery was tested by using the crystalline photovoltaic module. This testing performed as a proof concept for solar charging of batteries which is useful for most of the autonomous sensor. After connecting with solar energy, 3 mm battery charged at room temperature with a solar cell current of 15 µA for 5 h. as shown in Figure A1.4 (c) and drained it at 120ºC with programmed duty cycles. In sensor measurement mode (active mode) 200 µA is taken out for 1.5 seconds in every 3 mins where all measure data transmitted and then it enters to the sleep mode (device is turned off) where 3 µA continuous current is carried out from the battery. The voltage drop across the battery is found 3000 Ω in every reading at 120ºC as illustrated in Figure A1.4 (d). In these both experiments, fabricated miniaturized batteries have shown minimum load loss and ability to charge with solar energy for providing continuous power to high temperature autonomous microsystems.

A 1.3 Conclusion

We have developed a facile process using thermally stable electroactive materials and packaging components to construct lithium ion batteries with tunable dimensions and operable from room temperature to 120 °C. Miniaturized components design has optimized meticulously to achieve higher capacity and less internal impedance by keeping casing wall thickness 200 µm and maintaining proper compression between cup (Cathode) and Lid (Anode). Urethane-based epoxy has been categorized from different sealing agents and demonstrated its workability in the lithium-battery domain. The feasibility of these cells has demonstrated in 3D printed 2 mm to 5 mm scale rectangular metal casings by performing electrochemical studies from RT to 120 ºC. The resistance of the currently assembled millimeter size batteries (1750 Ω) and traditional coin cell (105 Ω) has compared regarding the active loading materials. Self-discharge test has performed with millimeter-size fabricated batteries to evaluate load loss with respective time. Sensor duty cycle program has carried out to check the expediency of miniaturized batteries for autonomous sensing applications at 120ºC, in this test 3 mm battery provided continuous data for 22 hours. This newly packaged millimeter batteries also demonstrated its compatibility with energy harvesting (solar cell) to provide continuous power to autonomous devices. It is expected that this high-temperature battery will be useful in self-directed miniaturized system where direct human control is not possible.

REFERENCES

1. Pohanka, M. and P.J.J.o.A.B. Skládal, *Electrochemical biosensors--principles and applications.* 2008. **6**(2).
2. Kuriyama, T. and J. Kimura, *FET-based biosensors.* Bioprocess technology, 1991. **15**: p. 139-162.
3. Song, S., et al., *Aptamer-based biosensors.* TrAC Trends in Analytical Chemistry, 2008. **27**(2): p. 108-117.
4. Cui, Y., et al., *High performance silicon nanowire field effect transistors.* Nano letters, 2003. **3**(2): p. 149-152.
5. Yang, X., et al., *Fullerene–biomolecule conjugates and their biomedicinal applications.* 2014. **9**: p. 77.
6. Kim, J., et al., *Fabrication of high-performance ultrathin In2O3 film field-effect transistors and biosensors using chemical lift-off lithography.* ACS nano, 2015. **9**(4): p. 4572-4582.
7. Mukherjee, S., et al., *A graphene and aptamer based liquid gated FET-like electrochemical biosensor to detect adenosine triphosphate.* IEEE transactions on nanobioscience, 2015. **14**(8): p. 967-972.
8. Makowski, M.S. and A.J.s. Ivanisevic, *Molecular analysis of blood with micro-/nanoscale field-effect-transistor biosensors.* 2011. **7**(14): p. 1863-1875.
9. Gupta, A., T. Sakthivel, and S.J.P.i.M.S. Seal, *Recent development in 2D materials beyond graphene.* 2015. **73**: p. 44-126.
10. Yan, R.-H., A. Ourmazd, and K.F.J.I.T.o.E.D. Lee, *Scaling the Si MOSFET: From bulk to SOI to bulk.* 1992. **39**(7): p. 1704-1710.
11. Colinge, J.-P.J.S.-s.e., *Multiple-gate soi mosfets.* 2004. **48**(6): p. 897-905.

12. Zhang, Y., et al., *Origin of spatial charge inhomogeneity in graphene.* Nat Phys, 2009. **5**(10): p. 722-726.

13. Jin, T., et al., *Suspended single-layer MoS2 devices.* Journal of Applied Physics, 2013. **114**(16): p. 164509.

14. Zhang, F., et al., *Etchant-free transfer of 2D nanostructures.* Nanotechnology, 2017. **29**(2): p. 025602.

15. Sarkar, D., et al., *MoS2 field-effect transistor for next-generation label-free biosensors.* ACS nano, 2014. **8**(4): p. 3992-4003.

16. Sarkar, D., et al., *MoS2 field-effect transistor for next-generation label-free biosensors.* 2014. **8**(4): p. 3992-4003.

17. Kalantar-zadeh, K. and J.Z. Ou, *Biosensors based on two-dimensional MoS2.* ACS Sensors, 2015. **1**(1): p. 5-16.

18. Neethirajan, S., et al., *Recent advancement in biosensors technology for animal and livestock health management.* 2017. **98**: p. 398-407.

19. Haes, A.J. and R.P.J.J.o.t.A.C.S. Van Duyne, *A nanoscale optical biosensor: sensitivity and selectivity of an approach based on the localized surface plasmon resonance spectroscopy of triangular silver nanoparticles.* 2002. **124**(35): p. 10596-10604.

20. Babacan, S., et al., *Evaluation of antibody immobilization methods for piezoelectric biosensor application.* 2000. **15**(11-12): p. 615-621.

21. Say, J., et al., *Process for producing an electrochemical biosensor*. 2000, Google Patents.

22. Shao, Y., et al., *Graphene based electrochemical sensors and biosensors: a review.* 2010. **22**(10): p. 1027-1036.

23. Pohanka, M. and J.J.I.J.E.S. Leuchter, *Biosensors based on semiconductors, a review.* 2017. **12**(7): p. 6611-6621.

24. Kerman, K., et al., *Nanomaterial-based electrochemical biosensors for medical applications.* 2008. **27**(7): p. 585-592.

25. Ramgir, N.S., Y. Yang, and M.J.S. Zacharias, *Nanowire-Based Sensors.* 2010. **6**(16): p. 1705-1722.

26. Ramnani, P., N.M. Saucedo, and A.J.C. Mulchandani, *Carbon nanomaterial-based electrochemical biosensors for label-free sensing of environmental pollutants.* 2016. **143**: p. 85-98.

27. Torchinsky, I. and G.J.N.r.l. Rosenman, *Wettability modification of nanomaterials by low-energy electron flux.* 2009. **4**(10): p. 1209.

28. Boguslavsky, Y., et al., *Controlling the wettability properties of polyester fibers using grafted functional nanomaterials.* 2011. **21**(28): p. 10304-10310.

29. Zhang, Y., et al., *Advances in conceptual electronic nanodevices based on 0D and 1D nanomaterials.* 2014. **6**(1): p. 1-19.

30. Novoselov, K., et al., *Two-dimensional atomic crystals.* Proceedings of the National Academy of Sciences of the United States of America, 2005. **102**(30): p. 10451-10453.

31. Stellacci, F., et al., *Laser and electron-beam induced growth of nanoparticles for 2D and 3D metal patterning.* Advanced Materials, 2002. **14**(3): p. 194.

32. Cao, L., et al., *Direct Laser-Patterned Micro-Supercapacitors from Paintable MoS2 Films.* Small, 2013. **9**(17): p. 2905-2910.

33. Li, X., et al., *Large-area synthesis of high-quality and uniform graphene films on copper foils.* Science, 2009. **324**(5932): p. 1312-1314.

34. Zhang, G. and D. Wang, *Colloidal lithography—the art of nanochemical patterning.* Chemistry–An Asian Journal, 2009. **4**(2): p. 236-245.

35. Bell, D.J., et al., *MEMS actuators and sensors: observations on their performance and selection for purpose.* Journal of Micromechanics and Microengineering, 2005. **15**(7): p. S153.

36. Hu, K., et al., *Written-in Conductive Patterns on Robust Graphene Oxide Biopaper by Electrochemical Microstamping.* Angewandte Chemie International Edition, 2013. **52**(51): p. 13784-13788.

37. Kim, K.S., et al., *Large-scale pattern growth of graphene films for stretchable transparent electrodes.* Nature, 2009. **457**(7230): p. 706-710.

38. Lochner, C.M., et al., *All-organic optoelectronic sensor for pulse oximetry.* Nature communications, 2014. **5**.

39. Ostfeld, A.E., et al., *Single-walled carbon nanotube transparent conductive films fabricated by reductive dissolution and spray coating for organic photovoltaics.* Applied Physics Letters, 2014. **105**(25): p. 253301.

40. Lu, X., et al., *Tailoring graphite with the goal of achieving single sheets.* Nanotechnology, 1999. **10**(3): p. 269.

41. Miyamoto, Y., H. Zhang, and D. Tománek, *Photoexfoliation of graphene from graphite: an Ab initio study.* Physical review letters, 2010. **104**(20): p. 208302.

42. Hernandez, Y., et al., *High-yield production of graphene by liquid-phase exfoliation of graphite.* Nature nanotechnology, 2008. **3**(9): p. 563-568.

43. Bang, G.S., et al., *Effective liquid-phase exfoliation and sodium ion battery application of MoS2 nanosheets.* ACS applied materials & interfaces, 2014. **6**(10): p. 7084-7089.

44. Lee, Y.H., et al., *Synthesis of large-area MoS2 atomic layers with chemical vapor deposition.* Advanced Materials, 2012. **24**(17): p. 2320-2325.

45. Miao, C., et al., *Chemical vapor deposition of graphene*. 2011: INTECH Open Access Publisher.

46. Reina, A., et al., *Large area, few-layer graphene films on arbitrary substrates by chemical vapor deposition.* Nano letters, 2008. **9**(1): p. 30-35.

47. Geim, A.K. and K.S. Novoselov, *The rise of graphene.* Nature materials, 2007. **6**(3): p. 183-191.

48. Novoselov, K., et al., *Two-dimensional gas of massless Dirac fermions in graphene.* nature, 2005. **438**(7065): p. 197-200.

49. Maffucci, A. and G.J.A.S. Miano, *Electrical properties of graphene for interconnect applications.* 2014. **4**(2): p. 305-317.

50. Castro, E.V., et al., *Biased bilayer graphene: semiconductor with a gap tunable by the electric field effect.* Physical Review Letters, 2007. **99**(21): p. 216802.

51. Shao, Y., et al., *Graphene based electrochemical sensors and biosensors: a review.* Electroanalysis, 2010. **22**(10): p. 1027-1036.

52. Allen, M.J., V.C. Tung, and R.B. Kaner, *Honeycomb carbon: a review of graphene.* Chemical reviews, 2009. **110**(1): p. 132-145.

53. Huang, Y., et al., *Graphene-based biosensors for detection of bacteria and their metabolic activities.* 2011. **21**(33): p. 12358-12362.

54. Yin, Z., et al., *Single-layer MoS2 phototransistors.* ACS nano, 2011. **6**(1): p. 74-80.

55. Ovchinnikov, D., et al., *Electrical transport properties of single-layer WS2.* ACS nano, 2014. **8**(8): p. 8174-8181.

56. Wang, Q.H., et al., *Electronics and optoelectronics of two-dimensional transition metal dichalcogenides.* Nature nanotechnology, 2012. **7**(11): p. 699-712.

57. Kuc, A., N. Zibouche, and T. Heine, *Influence of quantum confinement on the electronic structure of the transition metal sulfide T S 2.* Physical Review B, 2011. **83**(24): p. 245213.

58. Kośmider, K. and J. Fernández-Rossier, *Electronic properties of the MoS 2-WS 2 heterojunction.* Physical Review B, 2013. **87**(7): p. 075451.

59. Hong, X., et al., *Ultrafast charge transfer in atomically thin MoS2/WS2 heterostructures.* Nature nanotechnology, 2014. **9**(9): p. 682-686.

60. Balendhran, S., et al., *Semiconductors: Two-Dimensional Molybdenum Trioxide and Dichalcogenides (Adv. Funct. Mater. 32/2013).* Advanced Functional Materials, 2013. **23**(32): p. 3946-3946.

61. Jariwala, D., et al., *Emerging device applications for semiconducting two-dimensional transition metal dichalcogenides.* ACS nano, 2014. **8**(2): p. 1102-1120.

62. Li, H., et al., *Fabrication of single-and multilayer MoS2 film-based field-effect transistors for sensing NO at room temperature.* small, 2012. **8**(1): p. 63-67.

63. He, Q., et al., *Fabrication of Flexible MoS2 Thin-Film Transistor Arrays for Practical Gas-Sensing Applications.* Small, 2012. **8**(19): p. 2994-2999.

64. Zhao, W., R.M. Ribeiro, and G. Eda, *Electronic structure and optical signatures of semiconducting transition metal dichalcogenide nanosheets.* Accounts of chemical research, 2014. **48**(1): p. 91-99.

65. Chhowalla, M., et al., *The chemistry of two-dimensional layered transition metal dichalcogenide nanosheets.* Nature chemistry, 2013. **5**(4): p. 263-275.

66. Kalantar-zadeh, K., et al., *Two-Dimensional Transition Metal Dichalcogenides in Biosystems.* Advanced Functional Materials, 2015. **25**(32): p. 5086-5099.
67. Mak, K.F., et al., *Atomically thin MoS 2: a new direct-gap semiconductor.* Physical Review Letters, 2010. **105**(13): p. 136805.
68. Splendiani, A., et al., *Emerging photoluminescence in monolayer MoS2.* Nano letters, 2010. **10**(4): p. 1271-1275.
69. Wang, R., et al., *Ultrafast and spatially resolved studies of charge carriers in atomically thin molybdenum disulfide.* Physical Review B, 2012. **86**(4): p. 045406.
70. Novoselov, K.S., et al., *Room-temperature quantum Hall effect in graphene.* Science, 2007. **315**(5817): p. 1379-1379.
71. Ridley, B., *The electron-phonon interaction in quasi-two-dimensional semiconductor quantum-well structures.* Journal of Physics C: Solid State Physics, 1982. **15**(28): p. 5899.
72. Chen, J.-H., et al., *Intrinsic and extrinsic performance limits of graphene devices on SiO2.* Nature nanotechnology, 2008. **3**(4): p. 206-209.
73. Hwang, E., S. Adam, and S.D. Sarma, *Carrier transport in two-dimensional graphene layers.* Physical review letters, 2007. **98**(18): p. 186806.
74. Konar, A., T. Fang, and D. Jena, *Effect of high-κ gate dielectrics on charge transport in graphene-based field effect transistors.* Physical Review B, 2010. **82**(11): p. 115452.
75. Radisavljevic, B., et al., *Single-layer MoS2 transistors.* Nature nanotechnology, 2011. **6**(3): p. 147-150.
76. Adam, S., E. Hwang, and S.D. Sarma, *Scattering mechanisms and Boltzmann transport in graphene.* Physica E: Low-dimensional Systems and Nanostructures, 2008. **40**(5): p. 1022-1025.

77. Wang, D.W., et al., *3D aperiodic hierarchical porous graphitic carbon material for high-rate electrochemical capacitive energy storage.* Angewandte Chemie International Edition, 2008. **47**(2): p. 373-376.

78. Bolotin, K.I., et al., *Ultrahigh electron mobility in suspended graphene.* Solid State Communications, 2008. **146**(9): p. 351-355.

79. Kaasbjerg, K., K.S. Thygesen, and K.W.J.P.R.B. Jacobsen, *Phonon-limited mobility in n-type single-layer MoS 2 from first principles.* 2012. **85**(11): p. 115317.

80. Chiang, C.-W., et al., *Highly stretchable and sensitive photodetectors based on hybrid graphene and graphene quantum dots.* 2016. **8**(1): p. 466-471.

81. Zhu, W., et al., *Carrier scattering, mobilities, and electrostatic potential in monolayer, bilayer, and trilayer graphene.* Physical Review B, 2009. **80**(23): p. 235402.

82. Lin, M.-W., et al., *Mobility enhancement and highly efficient gating of monolayer MoS2 transistors with polymer electrolyte.* Journal of Physics D: Applied Physics, 2012. **45**(34): p. 345102.

83. Bao, W., et al., *High mobility ambipolar MoS2 field-effect transistors: Substrate and dielectric effects.* Applied Physics Letters, 2013. **102**(4): p. 042104.

84. Wang, F., et al., *Ionic liquid gating of suspended MoS2 field effect transistor devices.* Nano letters, 2015. **15**(8): p. 5284-5288.

85. Kim, S., et al., *High-mobility and low-power thin-film transistors based on multilayer MoS2 crystals.* Nature communications, 2012. **3**: p. 1011.

86. Radisavljevic, B., et al., *Single-layer MoS 2 transistors.* 2011. **6**(3): p. 147.

87. Jin, T., et al., *Suspended single-layer MoS2 devices.* Journal of Applied Physics, 2013. **114**(16): p. 164509.

88. Jin, T., et al., *Suspended single-layer MoS2 devices.* 2013. **114**(16): p. 164509.

89. Yuan, H., et al., *Liquid-gated ambipolar transport in ultrathin films of a topological insulator Bi2Te3.* Nano letters, 2011. **11**(7): p. 2601-2605.

90. Lin, M.-W., et al., *Mobility enhancement and highly efficient gating of monolayer MoS2 transistors with polymer electrolyte.* 2012. **45**(34): p. 345102.

91. Wang, F., et al., *Annealing and transport studies of suspended molybdenum disulfide devices.* Nanotechnology, 2015. **26**(10): p. 105709.

92. Kalantar-zadeh, K. and J.Z.J.A.S. Ou, *Biosensors based on two-dimensional MoS2.* 2015. **1**(1): p. 5-16.

93. Yun, W.S., et al., *Thickness and strain effects on electronic structures of transition metal dichalcogenides: 2H-M X 2 semiconductors (M= Mo, W; X= S, Se, Te).* Physical Review B, 2012. **85**(3): p. 033305.

94. Mak, K.F. and J. Shan, *Photonics and optoelectronics of 2D semiconductor transition metal dichalcogenides.* Nature Photonics, 2016. **10**(4): p. 216-226.

95. Tian, H., et al., *Optoelectronic devices based on two-dimensional transition metal dichalcogenides.* Nano Research, 2016. **9**(6): p. 1543-1560.

96. Babu, G., et al., *Transition Metal Dichalcogenide Atomic Layers for Lithium Polysulfides Electrocatalysis.* Journal of the American Chemical Society, 2016.

97. Duan, X., et al., *Two-dimensional transition metal dichalcogenides as atomically thin semiconductors: opportunities and challenges.* Chemical Society Reviews, 2015. **44**(24): p. 8859-8876.

98. Shaw, J.C., et al., *Chemical vapor deposition growth of monolayer MoSe2 nanosheets.* Nano Research, 2014. **7**(4): p. 511-517.

99. Vrubel, H. and X. Hu, *Growth and activation of an amorphous molybdenum sulfide hydrogen evolving catalyst.* ACS Catalysis, 2013. **3**(9): p. 2002-2011.

100. Wang, X., et al., *Chemical vapor deposition growth of crystalline monolayer MoSe2.* ACS nano, 2014. **8**(5): p. 5125-5131.

101. Zhan, Y., et al., *Large-area vapor-phase growth and characterization of MoS2 atomic layers on a SiO2 substrate.* Small, 2012. **8**(7): p. 966-971.

102. Wang, X., et al., *Controlled synthesis of highly crystalline MoS2 flakes by chemical vapor deposition.* Journal of the American Chemical Society, 2013. **135**(14): p. 5304-5307.

103. Wang, S., et al., *Shape evolution of monolayer MoS2 crystals grown by chemical vapor deposition.* 2014. **26**(22): p. 6371-6379.

104. Zhang, Q., et al., *Synthesis of MoS2 Nanosheets by Solid-State Reaction in CVD Furnace.* 2011. **128**(1): p. 125-129.

105. Najmaei, S., et al., *Vapour phase growth and grain boundary structure of molybdenum disulphide atomic layers.* 2013. **12**(8): p. 754.

106. Wang, H., et al., *MoSe2 and WSe2 nanofilms with vertically aligned molecular layers on curved and rough surfaces.* 2013. **13**(7): p. 3426-3433.

107. Scheuschner, N., et al., *Interlayer resonant Raman modes in few-layer MoS 2.* 2015. **91**(23): p. 235409.

108. Wieting, T. and J.J.P.R.B. Verble, *Infrared and Raman Studies of Long-Wavelength Optical Phonons in Hexagonal Mo S 2.* 1971. **3**(12): p. 4286.

109. Zhang, X., et al., *Raman spectroscopy of shear and layer breathing modes in multilayer MoS 2.* 2013. **87**(11): p. 115413.

110. Sun, D., et al., *Formation and interlayer decoupling of colloidal MoSe2 nanoflowers.* Chemistry of Materials, 2015. **27**(8): p. 3167-3175.

111. Zhao, W., et al., *Lattice dynamics in mono-and few-layer sheets of WS 2 and WSe 2.* 2013. **5**(20): p. 9677-9683.

112. Shidpour, R., et al., *A general two-step chemical vapor deposition procedure to synthesize highly crystalline transition metal dichalcogenides: A case study of MoS2.* 2016. **76**: p. 473-478.

113. Kim, S.K., et al., *Directional dependent piezoelectric effect in CVD grown monolayer MoS2 for flexible piezoelectric nanogenerators.* 2016. **22**: p. 483-489.

114. Das, S. and J.J.A.p.l. Appenzeller, *WSe2 field effect transistors with enhanced ambipolar characteristics.* 2013. **103**(10): p. 103501.

115. Liu, W., et al., *Role of metal contacts in designing high-performance monolayer n-type WSe2 field effect transistors.* 2013. **13**(5): p. 1983-1990.

116. Cao, D., et al., *Role of Chemical Potential in Flake Shape and Edge Properties of Monolayer MoS2.* The Journal of Physical Chemistry C, 2015. **119**(8): p. 4294-4301.

117. Gudibande, R.R. and U.o.P.D.o. Nanotechnology, *Application of the Novel 2D Nanoscale Material "graphene" in Bio/chemical Liquid Sensing and Flexible Electronics*. 2014.

118. Novoselov, K.S., et al., *Two-dimensional gas of massless Dirac fermions in graphene.* Nature, 2005. **438**(7065): p. 197-200.

119. Cho, W.-S. and K.J.I.E.D.L. Roy, *The effects of direct source-to-drain tunneling and variation in the body thickness on (100) and (110) sub-10-nm Si double-gate transistors.* 2015. **36**(5): p. 427-429.

120. Chen, H., et al., *Dramatic switching behavior in suspended MoS2 field-effect transistors.* 2018. **33**(2): p. 024001.

121. Tseng, A.A., A. Notargiacomo, and T. Chen, *Nanofabrication by scanning probe microscope lithography: A review.* Journal of Vacuum Science & Technology B: Microelectronics and Nanometer Structures Processing, Measurement, and Phenomena, 2005. **23**(3): p. 877-894.

122. Tao, N. and S. Boussaad, *Apparatus and method for fabricating arrays of atomic-scale contacts and gaps between electrodes and applications thereof*. 2004, Google Patents.

123. Schmidt, P.H. and E.G. Spencer, *Ion etching through a pattern mask*. 1975, Google Patents.

124. Kwon, H., et al., *Large scale MoS2 nanosheet logic circuits integrated by photolithography on glass*. 2016. **3**(4): p. 044001.

125. Castellanos-Gomez, A., et al., *Deterministic transfer of two-dimensional materials by all-dry viscoelastic stamping*. 2014. **1**(1): p. 011002.

126. Darhuber, A.A., et al., *Thermocapillary actuation of liquid flow on chemically patterned surfaces*. 2003. **15**(5): p. 1295-1304.

127. Wang, Y., et al., *Raman spectroscopy study of lattice vibration and crystallographic orientation of monolayer MoS2 under uniaxial strain*. 2013. **9**(17): p. 2857-2861.

128. O'Brien, M., et al., *Raman Spectroscopy of Suspended MoS2*. physica status solidi (b), 2017. **254**(11): p. 1700218.

129. Teo, W.Z., et al., *Cytotoxicity of exfoliated transition-metal dichalcogenides (MoS2, WS2, and WSe2) is lower than that of graphene and its analogues*. 2014. **20**(31): p. 9627-9632.

130. Makowski, M.S. and A. Ivanisevic, *Molecular Analysis of Blood with Micro-/Nanoscale Field-Effect-Transistor Biosensors.* small, 2011. **7**(14): p. 1863-1875.

131. Banerjee, S., T. Hemraj-Benny, and S.S. Wong, *Covalent surface chemistry of single-walled carbon nanotubes.* Advanced Materials, 2005. **17**(1): p. 17-29.

132. Sarkar, D. and K.J.A.P.L. Banerjee, *Proposal for tunnel-field-effect-transistor as ultra-sensitive and label-free biosensors.* 2012. **100**(14): p. 143108.

133. Bolotin, K.I., et al., *Ultrahigh electron mobility in suspended graphene.* 2008. **146**(9-10): p. 351-355.

134. Shadman, A., et al., *Monolayer MoS2 and WSe2 double gate field effect transistor as super nernst pH sensor and nanobiosensor.* 2016. **11**: p. 45-51.

135. Ameri, S., P. Singh, and S. Sonkusale. *Three dimensional monolayer graphene foam for ultra-sensitive pH sensing*. in *2015 Transducers-2015 18th International Conference on Solid-State Sensors, Actuators and Microsystems (TRANSDUCERS)*. 2015. IEEE.

136. Dinar, A.M., et al., *Comprehensive identification of sensitive and stable ISFET sensing layer high-k gate based on ISFET/electrolyte models.* 2019. **9**(2): p. 926.

137. Zafar, S., et al., *Optimization of pH sensing using silicon nanowire field effect transistors with HfO2 as the sensing surface.* 2011. **22**(40): p. 405501.

138. Van Hal, R., et al., *A novel description of ISFET sensitivity with the buffer capacity and double-layer capacitance as key parameters.* 1995. **24**(1-3): p. 201-205.

139. Gao, X.P., G. Zheng, and C.M.J.N.l. Lieber, *Subthreshold regime has the optimal sensitivity for nanowire FET biosensors.* 2009. **10**(2): p. 547-552.

140. Bergveld, P.J.S. and A.A. Physical, *The future of biosensors.* 1996. **56**(1-2): p. 65-73.

141. Goda, T. and Y.J.C.P.C. Miyahara, *DNA biosensing using field effect transistors.* 2011. **1**(4): p. 276-291.

142. Watts, B., L. Thomsen, and P.C.J.S.m. Dastoor, *Measurement of molecular order and orientation in nanoscale organic films.* 2005. **152**(1-3): p. 21-24.

143. Gunda, N.S.K., et al., *Optimization and characterization of biomolecule immobilization on silicon substrates using (3-aminopropyl) triethoxysilane (APTES) and glutaraldehyde linker*. 2014. **305**: p. 522-530.

144. Wu, S.-M., et al., *Detection of Escherichia coli in drugs with antibody conjugated quantum dots as immunofluorescence probes.* 2013. **78**: p. 9-13.

145. Yin, Z., et al., *Real-time DNA detection using Pt nanoparticle-decorated reduced graphene oxide field-effect transistors.* 2012. **4**(1): p. 293-297.

146. Kwon, O.S., et al., *Flexible FET-type VEGF aptasensor based on nitrogen-doped graphene converted from conducting polymer.* 2012. **6**(2): p. 1486-1493.

147. Ohno, Y., K. Maehashi, and K.J.J.o.t.A.C.S. Matsumoto, *Label-free biosensors based on aptamer-modified graphene field-effect transistors.* 2010. **132**(51): p. 18012-18013.

148. Ohno, Y., et al., *Electrolyte-gated graphene field-effect transistors for detecting pH and protein adsorption.* 2009. **9**(9): p. 3318-3322.

149. Wang, T., et al., *Direct detection of DNA below ppb level based on thionin-functionalized layered MoS2 electrochemical sensors.* 2014. **86**(24): p. 12064-12069.

150. Lee, D.-W., et al., *Field-effect transistor with a chemically synthesized MoS 2 sensing channel for label-free and highly sensitive electrical detection of DNA hybridization.* 2015. **8**(7): p. 2340-2350.

151. Wang, L., et al., *Functionalized MoS2 nanosheet-based field-effect biosensor for label-free sensitive detection of cancer marker proteins in solution.* 2014. **10**(6): p. 1101-1105.

152. Chang, J., et al., *Ultrasonic-assisted self-assembly of monolayer graphene oxide for rapid detection of Escherichia coli bacteria.* 2013. **5**(9): p. 3620-3626.

153. Schwierz, F.J.N.n., *Graphene transistors.* 2010. **5**(7): p. 487.

154. de Moraes, A. and L.J.C. Kubota, *Recent trends in field-effect transistors-based immunosensors.* 2016. **4**(4): p. 20.

155. Villanueva, L.G., J. Bausells, and J. Brugger, *Grand Challenge in N/MEMS.* Frontiers in Mechanical Engineering, 2016. **1**: p. 15.

156. Kebabi, B., C.K. Malek, and F. Ladan, *Stress and microstructure relationships in gold thin films.* Vacuum, 1990. **41**(4-6): p. 1353-1355.

157. Shibahara, K., S. Nishino, and H. Matsunami, *Metal-oxide-semiconductor characteristics of chemical vapor deposited cubic-SiC.* Japanese Journal of Applied Physics, 1984. **23**(11A): p. L862.

158. Humble, P.H., J.N. Harb, and R. LaFollette, *Microscopic nickel-zinc batteries for use in autonomous microsystems.* Journal of the Electrochemical Society, 2001. **148**(12): p. A1357-A1361.

159. Ayazian, S., et al., *A photovoltaic-driven and energy-autonomous CMOS implantable sensor.* IEEE Transactions on biomedical circuits and systems, 2012. **6**(4): p. 336-343.

160. Hou, L., et al., *Autonomous Wireless Sensor Node with Thermal Energy Harvesting for Temperature Monitoring of Industrial Devices.* International Journal of Online Engineering, 2017. **13**(4).

161. Gartner, M., et al. *Sustainable Autonomous System for Nitrites/Nitrates and Heavy Metals Monitoring of Natural Water Sources (WaterSafe)*. in *Conference on Sustainable Energy*. 2017. Springer.

162. Kim, J., et al., *Miniaturized Battery-Free Wireless Systems for Wearable Pulse Oximetry.* Advanced Functional Materials, 2017. **27**(1).

163. Corbishley, P. and E. Rodríguez-Villegas, *Breathing detection: towards a miniaturized, wearable, battery-operated monitoring system.* IEEE Transactions on Biomedical Engineering, 2008. **55**(1): p. 196-204.

164. Cook-Chennault, K., N. Thambi, and A. Sastry, *Powering MEMS portable devices—a review of non-regenerative and regenerative power supply systems with special emphasis on piezoelectric energy harvesting systems.* Smart Materials and Structures, 2008. **17**(4): p. 043001.

165. Nathan, M., *Microbattery technologies for miniaturized implantable medical devices.* Current pharmaceutical biotechnology, 2010. **11**(4): p. 404-410.

166. Ambrosi, A. and M. Pumera, *3D-printing technologies for electrochemical applications.* Chemical Society Reviews, 2016. **45**(10): p. 2740-2755.

167. Parekh, D.P., et al., *3D printing of liquid metals as fugitive inks for fabrication of 3D microfluidic channels.* Lab on a Chip, 2016. **16**(10): p. 1812-1820.

168. Ladd, C., et al., *3D printing of free standing liquid metal microstructures.* Advanced Materials, 2013. **25**(36): p. 5081-5085.

169. Muñoz, J., et al., *Planar compatible polymer technology for packaging of chemical microsensors.* Journal of the Electrochemical Society, 1996. **143**(6): p. 2020-2025.

170. Lee, S.-W., et al., *UV-curing and thermal stability of dual curable urethane epoxy adhesives for temporary bonding in 3D multi-chip package process.* International Journal of Adhesion and Adhesives, 2013. **44**: p. 138-143.

171. Rimdusit, S. and H. Ishida, *Development of new class of electronic packaging materials based on ternary systems of benzoxazine, epoxy, and phenolic resins.* Polymer, 2000. **41**(22): p. 7941-7949.

172. De Buyl, F., *Silicone sealants and structural adhesives.* International Journal of Adhesion and Adhesives, 2001. **21**(5): p. 411-422.

173. Shiku, H., et al., *Oxygen permeability of surface-modified poly (dimethylsiloxane) characterized by scanning electrochemical microscopy.* Chemistry letters, 2006. **35**(2): p. 234-235.

174. Lee, I., et al., *A Wire-overhead-free Reset Propagation Scheme for Millimeter-scale Sensor Systems.* JOURNAL OF SEMICONDUCTOR TECHNOLOGY AND SCIENCE, 2017. **17**(4): p. 524-533.

175. Lee, I. and Y. Lee, *Circuit Design in mm-Scale Sensor Platform for Future IoT Applications*, in *Smart Sensors and Systems*. 2017, Springer. p. 57-81.

ABSTRACT

2D SUSPENDED FET TECHNOLOGY: OVERCOMING SCATTERING EFFECT FOR ULTRASENSITIVE RELIABLE BIOSENSOR

by

NIRUL MASURKAR

December 2019

Advisor: Dr. Leela Mohana Reddy Arava

Co-Advisor: Dr. Gregory Auner

Major: Mechanical Engineering

Degree: Doctor of Philosophy

TMDs such as MoS_2 is playing an important role in the field of FETs, photodetectors, thin film transistors and efficient biosensors because of their direct band-gap, high mobility, and biocompatibility. Despite these strengths, the performance and reliability of such atomic layer are easily influenced by supporting substrate. Interaction between the supporting substrate and MoS_2 implies that interface control is vital for performance of devices consisting of monolayer MoS_2. In particular, the Silicon dioxide (SiO_2) supporting substrate has an uneven morphology and is chemically active because of trapped environmental gases, unknown functional groups, chemical adsorbates, and charges. Thus, adding another layer of MoS_2 on the top of SiO_2 cannot contribute charge transport clearly, which leads to the unreliable function of every single device. To solve the interface problem, suspended 2D layer devices have been reported by wet etching silicon di oxide underneath the monolayer. Freestanding MoS_2 has shown 10 times greater back gate electronic mobility than the supporting on the SiO_2 substrate. However, the existing SiO_2 requires hazardous chemical etchants such as hydrofluoric acid (HF), which is difficult to handle and affects the 2D film structure and purity. Secondly, freestanding MoS_2 sags between the two electrodes because

of the high spacing (~ 2 µm), which makes it impossible to coat another layer such as hafnium oxide (HfO_2) and antibodies on top of monolayer. Therefore, this structure impedes making top gate FET biosensors, which allows for only back gating. However, back gate mobility is far lesser than the top gate mobility which hinders making a highly sensitive FET-based biosensor because the sensitivity of a sensor depends on its mobility.

In this work, CVD grown MoS_2 channel material is transferred on self-assembled photolithographically patterned nano-gaps to achieve suspension and is covered with HfO_2 to eliminate the direct functionalization of channel material. These nano-gap arrays provide mechanical strength to the monolayer and do not allow the supporting substrate to touch after coating another thin insulating layer as well as linkers/antibodies. HfO_2 can be easily functionalized by silane-based linkers and antibodies (E-coli antibodies) to bring variation to the suspended 2D material by targeting a charged biomolecule (E-coli). In addition, termination of the supporting substrate leads to decrement of subthreshold swing which is inversly proportional to the sensitivity of the FET biosensor. The proposed FET biosensor has the capability to detect one molecule because of its single atomic layer as a channel material, its scalability due to the involvement of optical photolithography, and its fast response because of higher mobility.

AUTOBIOGRAPHICAL STATEMENT
NIRUL MASURKAR

Education

Doctor of Philosophy, Wayne State University, Detroit, USA, 2014-2019
Master of Science, University of Dundee, Scotland, UK, 2012
Bachelor of Engineering, Nagpur University, Nagpur, India, 2009

Journal Publications

1. *Nirul Masurkar, Naresh Kumar Thangavel, Sally Yurgelevic, Gregory W Auner, Leela Mohana Reddy Arava;* Suspended MoS_2 biosensor for reliable sensing, manuscript is under communication
2. *Nirul Masurkar, Sundeep Varma, ALM Reddy;* Wafer-scale nanogap fabrication on flexible substrate for TMD based CMOS circuits, manuscript is under communication
3. *Nirul Masurkar, Naresh Kumar Thangavel, Sally Yurgelevic, Gregory W. Auner and Leela Mohana Reddy Arava;* Suspended 2D Material Biosensor for Reliable Sensing, **ECS Meeting Abstracts**, 515-515, First Author
4. *Nirul Masurkar; Naresh Kumar Thangavel, Leela Mohana Reddy Arava;* CVD-grown MoSe2 nanoflowers with dual active sites for efficient electrochemical Hydrogen Evolution Reaction; **ACS Appl. Mater. Interfaces**, 2018, 10 (33), pp 27771 -27779. (Impact Factor-8.04) First Author
5. *Nirul Masurkar, Sanjeev Porchelvan, Babu Ganguli, Leela Mohana Reddy Arava;* High Power micro/millimeter rechargeable battery packaging for high temperature applications, **Journal of Power Source**, Volume 399, 30 September 2018, Pages 179-185 (Impact Factor-6.97) First Author
6. *Ganguli Babu, Nirul Masurkar, Hesham Al Salem, Leela Mohanna Reddy Arava;* Transition Metal Dichalcogenide Atomic Layers for Lithium Polysulfides Electrocatalysis, **Journal of the American Chemical Society**, 2017, 139(1), pp 171-178 (Impact factor-14.357) First Co-Author
7. *Nirul Masurkar, Kawsar Jamil, Leela Mohana Reddy Arava;* Environmental effects on the Polypyrrole trilayer actuator, **MDPI Actuators**, 2017, 6(2), 17 (Impact Factor-2.8) First Author
8. *Shuangjie Liu, Nirul Masurkar, ALM Reddy;* Experimental and Simulation modelling of Polypyrrole trilayer actuator, **ACS Omega**, 2015, Volume 4, 6436-6442 (Impact factor-2.4), Co- First Author
9. *Andreas Winter, Antony George, Christof Neumann, Zian Tang, Michael J, Johannes skupek, Nirul Masurkar, Leela Mohana Reddy Arava, Thomas Weimann, Uwe Hübner, Ute Kaiser, Andrey Turchanin;* Lateral heterostructures of two-dimensional materials by electron-beam induced stitching, **Elsevier, Carbon**, 2018, Volume 128, 106-116 (Impact Factor-6.337)
10. *Khalid Ababtain, Ganguli Babu, Sandhya Susarla, Hemtej Gullapalli, Nirul Masurkar, Pulickel M. Ajayan and Leela Mohana Reddy Arava;* Porous Graphene Current Collectors Filled with Silicon as Anode for High Performance Lithium ion Battery Applications; **IOP, Material research Express**, 2018, Volume 5, Number 1 (Impact factor-1.25)
11. *Edwin Jager, Nirul Masurkar, NF Nworah, Babita Gaihre, Gurce Alici, Geoffrey Spinks;* Patterning and electrical interfacing of individually controllable conducting polymer microactuators, **Sensors and Actuators B: Chemical**, 2013, Volume 183, Pages 283-289 (Impact factor-5.401) First Co-Author
12. *Edwin Jager, Nirul Masurkar, NF Nworah, Babita Gaihre, Gaurce Alici, Geoffrey Spinks;* Individually controlled conducting polymer tri-layer microactuators, **Solid-State Sensors, Actuators and Microsystems**, 2013, 978-1-4673-5983-2 (Impact Factor: 2.52) First Co-Author
13. *W Yi, C Chen, Z Feng, Y Xu, C Zhou, Nirul Masurkar, John Cavanaugh and Mark Ming-Cheng Cheng;* A flexible and implantable microelectrode arrays using high-temperature grown vertical carbon nanotubes and a biocompatible polymer substrate, **IOP Nanotechnology**, 2015, Volume 26, 125-301 (Impact factor-3.404)
14. *Naresh kumar Thangavel, Nirul Masurkar, AR Sawas, L Arava;* Electrocatalysis of Polysulfide Redox in Lithium-Sulfur Battery, **ECS Meeting Abstracts**, 515-515, First Co-Author
15. *Rathi, Keerti, Nirul Masurkar, Sundeep Varma, Leela Arava, Kaushik Pal;* Ruthenium Decorated Tungsten Disulfide Quantum Dots for CO_2 Gas Sensor, submitted **ACS applied nanomaterials**, First Co-Author

Patents

1. *Leela Mohana Reddy Arava, Nirul Masurkar*, Method for fabrication wafer scale nano/submicron gap electrodes and arrays via photolithography, WO-2019074977A1

2. *Leela Mohana Reddy Arava, Nirul Masurkar, Babu Ganguli*, Fabrication of micro/millimeter-scale power sources and the process flow therefor, WO-2019074976A1.